LUND UNIVERSITY | LUND INSTITUTE OF TECHNOLOGY
Division of Structural Mechanics | Sweden 1996 | Report TVSM-3018

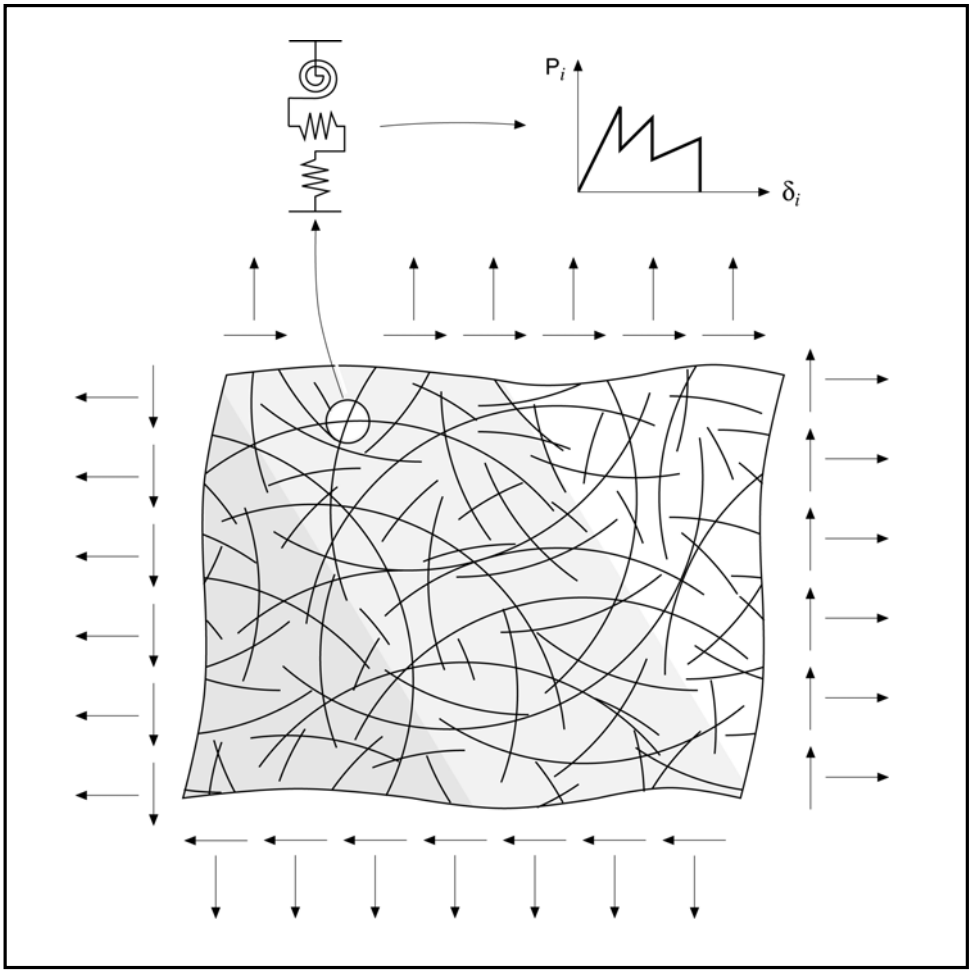

A NETWORK MODEL APPLIED TO CELLULOSE FIBRE MATERIALS

SUSANNE HEYDEN

LUND UNIVERSITY | LUND INSTITUTE OF TECHNOLOGY
Division of Structural Mechanics | Sweden 1996 | Report TVSM-3018
CODEN: LUTVDG / (TVSM-3018) / 1-155 / (1996) | I SSN 0281-6679

A NETWORK MODEL APPLIED TO CELLULOSE FIBRE MATERIALS

SUSANNE HEYDEN

Acknowledgements

The research presented in this licentiate thesis was performed at the Division of Structural Mechanics, Lund Institute of Technology. The financial support from Bo Rydins Stiftelse för Vetenskaplig Forskning and the Swedish National Board for Industrial and Technical development, NUTEK, is greatfully acknowledged.

I would like to thank my supervisor, Dr. Per Johan Gustafsson, for his excellent guidance and support during the course of this work. He has supplied numerous ideas, has a remarkable scientific intuition and is always enthusiastic. I also want to thank Prof. Hans Petersson and Dr. Christer Nilsson for interesting discussions and comments on the manuscript, as well as my other colleagues for their support.

The industrial partners in this project have been SCA Research AB and Mölnlycke AB, and I am grateful for the ideas, information and comments which their representatives have supplied.

Thanks is also due to Per-Anders Hansson and Kent Persson for helping me out with the computer system, and to Bo Zadig for skilfully drawing the more complicated figures.

Finally, I want to express my gratitude to Anders for his support.

Lund in March 1996

Susanne Heyden

Abstract

A network mechanics model for analysis of materials made of dry-shaped cellulose fibres is proposed. In terms of the model, the network is composed of fibres of arbitrary distribution in length, curvature, cross-section, stiffness and strength. The fibres are arranged in a random structure according to an arbitrary orientation distribution. Where fibres meet there may be fibre-to-fibre interaction, modelled by a linear or non-linear spring coupling representing stick-slip performance. The connection is of arbitrary distribution in stiffness and strength.

The network geometry is periodic, any cell under observation being regarded as one of many identical cells that make up a global structure. A set of cyclic boundary and loading conditions facilitates obtaining relevant results even in the case of small network cells.

A two-dimensional implementation of the model was carried out, and several examples of simulation results are provided. The results concern geometrical properties of the network, and the effects on network stiffness and fracture behaviour due to variations of sample size, boundary conditions and the various micro-level parameters mentioned above.

key words: network mechanics, fibre network, cellulose fibres, fracture, stiffness, computer simulation

Contents

1. Introduction

1.1. General remarks

Cellulose fibres are obtained by defibration of wood, by either chemical or mechanical processing. A major part of the pulp is used for making paper, which is manufactured by forming the wet fibres into sheets. Another important product made from pulp is dry-shaped cellulose fibre fluff, see Figures 1.1 and 1.2. This kind of material is produced by blowing the fibres, in a dry condition, into the desired shape. The result is a material used mainly in diapers and health care products. It is also possible to blow the fibres together with an adhesive aerosol present. In this case the bonds between the fibres are stronger, and fields of application include insulation boards and various moulded products, the latter being of higher density.

Some of the products mentioned have other main functions like absorbing liquid or preventing heat transfer, but it is of course also necessary that they can withstand the mechanical impact that they are subjected to when in use. This study deals with the mechanical properties of dry-shaped cellulose fibre materials, and

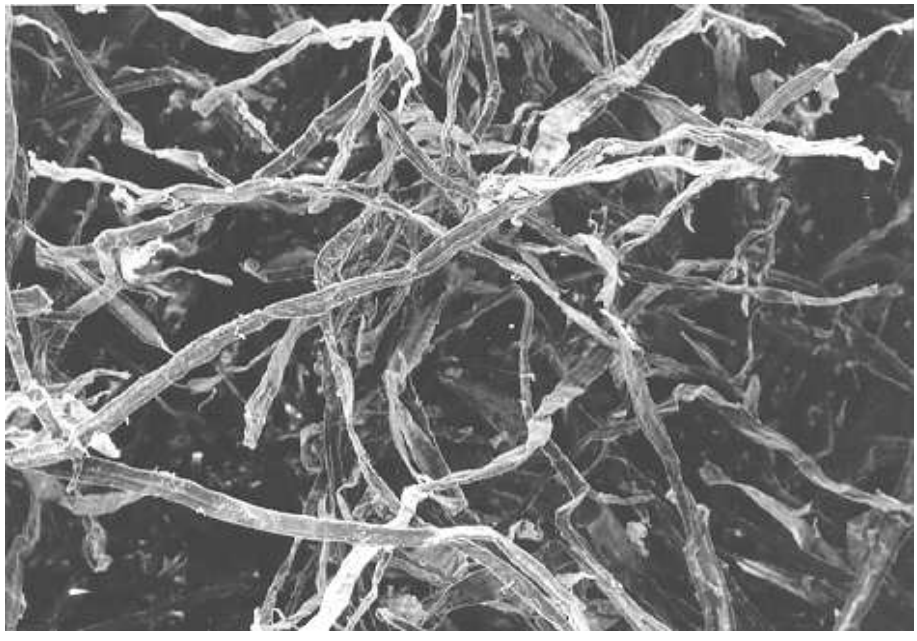

Figure 1.1: *Cellulose fibre fluff seen in a microscope.*

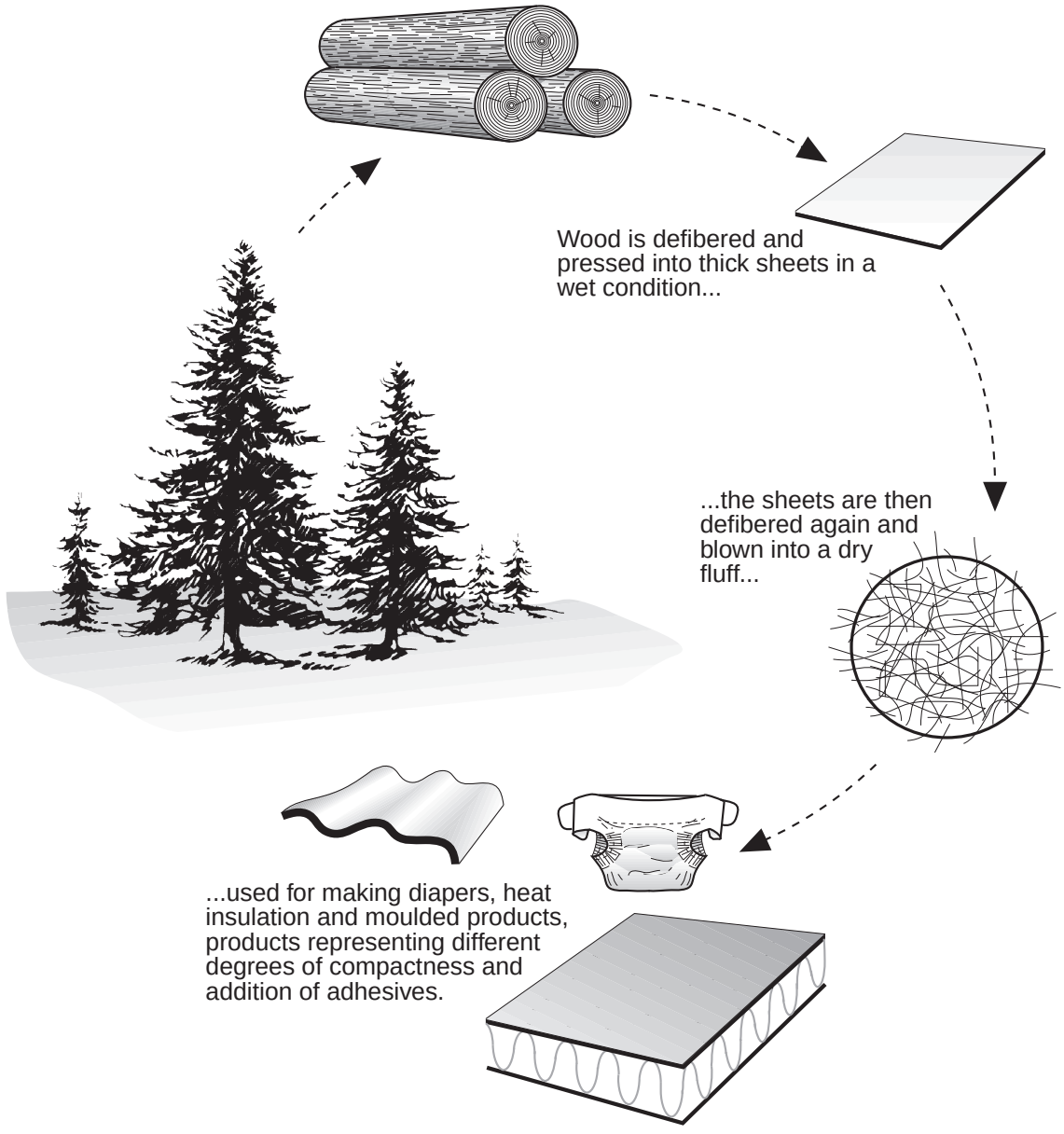

Figure 1.2: *Dry-shaped cellulose fibre fluff is made from wood, and is used for diapers, insulation and moulded products.*

examines what factors are of importance for mechanical properties such as stiffness, strength, strain localization and fracture process of a cellulose fibre fluff.

A network model approach is used. Network mechanics can be very useful in modelling various heterogeneous materials such as concrete, where the network structure does not have an obvious physical interpretation. In the case of a cellulose fibre material, however, the material is indeed of a real network character, and the modelling becomes comparatively straightforward.

It is the increasing capacity of computers that makes it possible to apply this kind of model, but computer capacity also sets a limit to what can be achieved from the calculations.

1.2. Aim and limitations of present investigation

Due to strong market competition, the absorbent product industry is very research intensive. The need within this industry for methods for rationally analysing the mechanical behaviour of fibre materials has been emphasized. The aim of the present study is to develop such a model for the rational mechanical and geometrical analysis of materials made of cellulose fibres.

One established concept within structural mechanics is to make assumptions as to the properties and behaviour of the components of a material on a lower structural level, and thereby calculate the expected behaviour of the material on a higher structural level. In this study, assumptions are made on the network level, see Figure 1.3, from [28], and the properties on the continuum level are obtained by computer simulations.

A theoretical model of the fibre material is introduced in terms of fibres, fibre-to-fibre connections and the structure into which these are assembled. In order to reduce the computational effort, the numerical implementation of the model is at present restricted to two dimensions. The implementation involves two separate steps. First a network structure is generated according to prescribed statistical distributions of the various properties that define the micro-structure of the material. The resulting structure is then assumed to be subjected to strain, and the finite element method is used to obtain the global stiffness properties. Through introducing fracture criteria for fibres and fibre-to-fibre connections, a non-linear simulation of the fracture process can be carried out.

Computer simulations allow relations between parameters on the microlevel and the global level to be obtained. The pertinent microlevel parameters include those of the length distribution, the orientation distribution, the geometrical and the constitutive properties of the fibres, the constitutive properties of the fibre-to-fibre connections, the rate of heterogeneity of the network and also the network density.

The corresponding global characteristics can be divided into purely geometrical and mechanical properties. Interesting geometrical properties include the number of fibre-to-fibre connections and the percentage of the network that is active. By non-active parts are meant parts that are in a state of zero stress regardless of loading at the boundary of the network. Concerning the mechanics, practical interest is

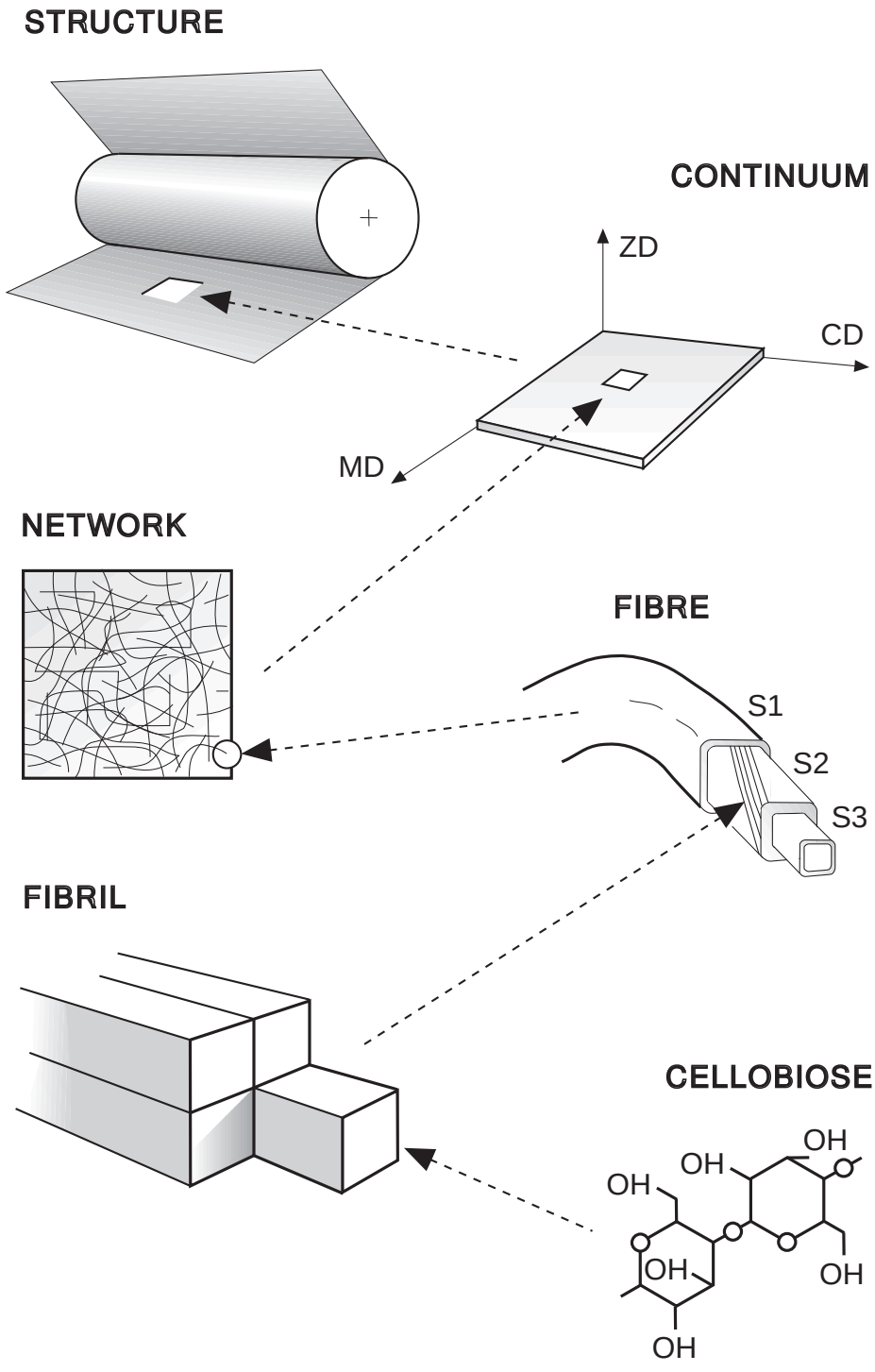

Figure 1.3: *Modelling and analysis can take place at different structural levels. This study deals with the transition from network to continuum. [28].*

focused on the initial stiffness properties and on the fracture process, the latter involving strength, strain localization and softening. From the application point of view, strain localization is of particular interest, since it may initiate crumbling in case of cyclic loading.

Particular attention is paid to the network size needed to obtain relevant computational results. The choice of boundary conditions is an important parameter in this context, and a concept of periodic geometry and boundary conditions is used in an effort to minimize the required network size, and thereby minimize the number of degrees of freedom.

Viscous effects and dynamic behaviour of the material are not treated in this study.

1.3. Organisation of the report

In Chapter 2 some earlier work on cellulose fibre network mechanics is summarized. This includes both theoretical network modelling and computer simulations.

In Chapter 3 the proposed theoretical model of the fibre network is presented. The parameters that define a network are listed and discussed.

Chapter 4 describes how a network is generated and prepared for the analysis of mechanical performance.

Chapter 5 contains results concerning purely geometrical properties of a network, such as number of fibre-to-fibre connections and the mechanically active part of a network.

In Chapter 6, methods for obtaining the global initial stiffness properties of a network are thoroughly discussed. Different boundary conditions are considered.

In Chapter 7, simulation results of global initial stiffness properties are presented, in terms of Young's modulus and Poisson's ratio of networks. These results illustrate how stiffness properties are affected by boundary conditions, network size, network density, stiffness properties of fibres and connections, as well as curl and length and orientation distribution of fibres.

Chapter 8 deals with the fracture process. Output parameters of interest are defined and discussed, and the methods used for obtaining them are presented.

Chapter 9 presents results from the analysis of the fracture process. It shows how global parameters such as strength, fracture energy, and localization depend on sample size, network density, properties of connections and other micro-level parameters.

Chapter 10 contains a discussion of numerical aspects of the study, what problems have arisen and how they have been solved.

Conclusions are given and future plans are outlined in Chapter 11.

Finally, in Appendix A to E, some algorithms and calculations are indicated.

1.4. Notations

Notations are explained in the text when they first occur. In addition, a list of main notations is given below together with the corresponding SI-units. A barred letter denotes arithmetic mean value of the parameter in question.

A_f	cross-sectional area of fibre	[m^2]
b_f	width of rectangular fibre cross-section	[m]
c	curl index, see Figure 3.1	[-]
$\boldsymbol{D}$	3x3 constitutive matrix	[N/m]
D_{ij}	element in row i, column j of $\boldsymbol{D}$	[N/m]
$d(x, y)$	network density probability function	[-]
E	Young's modulus of 2-d isotropic network	[N/m]
E_f	Young's modulus of fibre	[Pa]
$\boldsymbol{F}$	(F_x, F_y, M), spring forces in connection	[N],[Nm]
F_{ult}	ultimate resultant force in connection	[N]
G	shear modulus of 2-d isotropic network	[N/m]
G_f	fracture energy of network, see Section 8.3	[Nm/m]
h_f	depth of rectangular fibre cross-section	[m]
I_f	moment of inertia of fibre	[m^4]
$\boldsymbol{K}_e$	element stiffness matrix	[Nm],[N],[N/m]
$\boldsymbol{K}$	system stiffness matrix	[Nm],[N],[N/m]
k_i	stiffness of spring in direction i, $i = x, y, \phi$	[N/m],[Nm/rad]
L	side-length of network	[m]
l_{ch}	characteristic length	[m]
l_f	length of fibre	[m]
l_s	free fibre segment length	[m]
M_{ult}	ultimate moment in connection	[Nm]
m	degree of utilization for fibre or connection	[-]
N	probability distribution function	[-]
n_c	number of fibre crossings	[-]
n_f	number of fibres	[-]
n_s	number of slips before complete connection failure	[-]
p	approximate active part of network	[-]
s	probability of interaction at a fibre crossing	[-]
$\boldsymbol{u}$	(u_x, u_y, θ), in-plane displacements and rotations in a node, element or structure	[m],[rad]
w_e	external work	[Nm]
w_i	internal elastic strain energy	[Nm]
$\boldsymbol{x}$	(x, y), rectangular Cartesian coordinates	[m]
α	angle of the fibre relative to the x-axis, ccw positive	[rad]
β_1	reduction of connection stiffness at slip	[-]
β_2	reduction of connection strength at slip	[-]
$\Delta\boldsymbol{u}$	$(\Delta u_x, \Delta u_y, \Delta\theta)$ in-plane deformations in element	[m],[rad]

$\boldsymbol{\epsilon}$	$(\epsilon_x, \epsilon_y, \gamma_{xy})$, strain vector	[-]
ϵ_{lim}	strain in network at maximum stress	[-]
ϵ_{ult}	ultimate strain in network	[-]
κ	fibre curvature	$[\mathrm{m}^{-1}]$
ν	Poisson's ratio of 2-d isotropic network	[-]
ρ	network density in 2-d; total fibre length per unit area	$[\mathrm{m}^{-1}]$
$\boldsymbol{\sigma}$	$(\sigma_x, \sigma_y, \tau_{xy})$, stress vector	[N/m]
σ_{max}	maximum stress in network	[N/m]
σ_{ult}	ultimate normal stress in fibre	[Pa]
τ_{ult}	ultimate shear stress in fibre	[Pa]

2. Earlier work on cellulose fibre network mechanics

The development of models for understanding the mechanical behaviour of fibre networks closely reflects the development of computers. The earliest models use analytical methods and are thus confined to rather simple and uniform networks. Nevertheless, they produce results of great interest and value. During the 70s and 80s the arrival of computers of considerable computation capacity resulted in the first computer simulations of network behaviour. This evolution has continued, and in the 90s several new models have appeared, taking more and more variables into account. The variables included in the models are naturally those which are believed to be of importance. Experimental progress, the possibility of measuring new properties in a network, has also been an important factor in choosing what parameters to study.

Most references given in this chapter deal with paper, and this reflects the fact that there is not much literature on the geometry and mechanics of dry-shaped cellulose fibre materials. There are however obvious similarities between the two material types, the main differences being the density, the more three-dimensional character and weaker fibre-to-fibre bonding of a fibre fluff.

2.1. Analytical network models

A very often cited paper treating the geometry of fibre networks was presented by Kallmes and Corte in 1960, see [15]. They state that the structure of paper (the geometric arrangement of fibres and inter-fibre spaces) is an effect of the paper-making process, as well as the cause of the paper's properties. In the article, relations are obtained between various geometrical properties of the network such as number of fibre crossings and average segment length between crossings, and basic properties of the fibres and the sheet such as mean fibre length and number of fibres.

They are dealing with a two-dimensional sheet, which is defined as a sheet where the area which is covered by more than two fibres is negligible. Probability theory is used, and the fibres are assumed to be deposited independently of each other. Further, it is assumed that the fibres are randomly distributed over the area and have a random orientation. Among the results, the following equations are cited for $\bar{n}_c$, average number of fibre crossings in a square of side-length L, occupied by n_f fibres of average length $\bar{l}_f$, and $\bar{l}_s$, average free segment length on a fibre. $\bar{c}$ denotes average curl index, that is distance between fibre end points divided by fibre length,

see Figure 3.1.

$$\bar{n}_c = \frac{(n_f \bar{l}_f)^2 \bar{c}^2}{L^2 \pi} \tag{2.1}$$

$$\bar{l}_s = \frac{\bar{l}_f n_f \bar{c}}{2\bar{n}_c} \tag{2.2}$$

In addition to average values of geometrical and topological properties of the model network, distributions of various properties are also given, and the analytical results are compared to experimental results.

Komori and Makishima presented in 1977, [17], the equations corresponding to (2.1) and (2.2) for a three-dimensional fibre assembly where the fibres have an arbitrary orientation distribution. If the fibres are not straight, however, the orientation distribution function must be interpreted as the orientation distribution of the infinitesimal fibre segments. For the case of a two-dimensional network and uniform orientation distribution, the equations as expected reduce to those of [15].

[7] is a book presented by Deng and Dodson in 1994, in which various aspects of the stochastic geometry of paper are compiled.

An early fibre network model dealing with mechanical properties was presented by Cox in 1952, see [6]. He treats both two- and three-dimensional networks, but the results cited here apply to the former case. He assumes a perfectly homogeneous network of long straight thin fibres oriented according to a law of statistical distribution. Each fibre is assumed to extend from one edge of the network to the other, see Figure 2.1; its bending stiffness is negligible and there is no interaction between the fibres. This means that the strain field is homogeneous throughout the network,

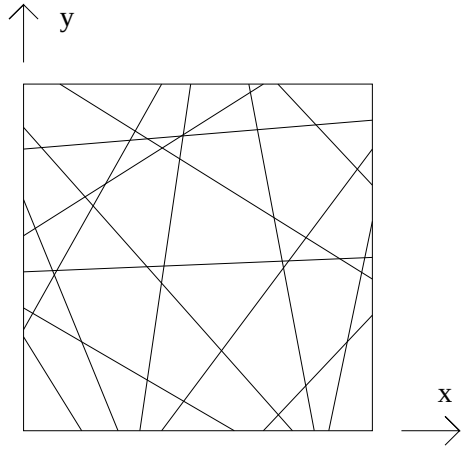

Figure 2.1: *Cox' homogeneous network.*

and if the network is subjected to a strain

$$\boldsymbol{\epsilon} = (\epsilon_x, \epsilon_y, \gamma_{xy}),$$

the axial strain in a fibre inclined an angle α to the x-axis is

$$\epsilon = \epsilon_x \cos^2 \alpha + \epsilon_y \sin^2 \alpha + \gamma_{xy} \cos \alpha \sin \alpha. \tag{2.3}$$

Cox shows analytically that if the orientation distribution function is of the form

$$f(\alpha) = \frac{1}{\pi}(1 + a_1 \cos 2\alpha + a_2 \cos 4\alpha + a_3 \cos 6\alpha + ... + b_1 \sin 2\alpha + b_2 \sin 4\alpha + ...), \tag{2.4}$$

where

$$\int_0^\pi f(\alpha) d\alpha = 1, \tag{2.5}$$

the elements of the constitutive matrix $\boldsymbol{D}$, which relates $\boldsymbol{\epsilon}$ and stress $\boldsymbol{\sigma}$=$(\sigma_x, \sigma_y, \tau_{xy})$ in

$$\boldsymbol{\sigma} = \boldsymbol{D}\boldsymbol{\epsilon} \tag{2.6}$$

are:

$$\begin{aligned} D_{11} &= \frac{K}{16}(6 + 4a_1 + a_2) \\ D_{22} &= \frac{K}{16}(6 - 4a_1 + a_2) \\ D_{13} &= \frac{K}{16}(2b_1 + b_2) \\ D_{23} &= \frac{K}{16}(2b_1 - b_2) \\ D_{12} &= D_{33} = \frac{K}{16}(2 - a_2) \end{aligned} \tag{2.7}$$

where

$$K = A_f E_f \rho.$$

A_f denotes cross-sectional area of the fibres, E_f Young's modulus of the fibres and ρ the network density, that is total fibre length per unit area. Note that the higher order terms in the expansion of $f(\alpha)$ disappear in the integration. For an isotropic material, where $f(\alpha) = 1/\pi$, this reduces to

$$E = \frac{K}{3} \tag{2.8}$$

$$G = \frac{K}{8} \tag{2.9}$$

$$\nu = \frac{1}{3}, \tag{2.10}$$

E, G and ν denoting Young's modulus, shear modulus and Poisson's ratio of the network. The stiffness values predicted by this homogeneous field model are not reached in real cellulose fibre networks, but they could be viewed as an upper limit. To approach the homogeneous strain field situation in a network where the fibres do not extend from edge to edge, an alternative mechanism of transferring forces across

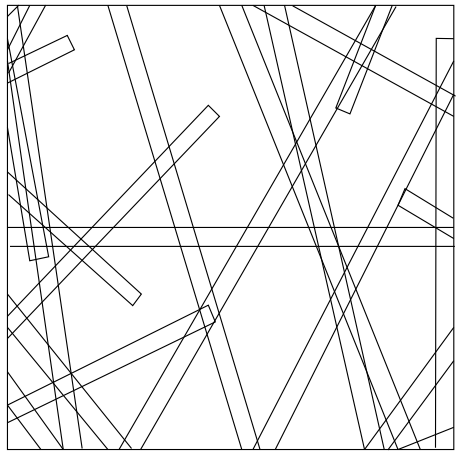

Figure 2.2: *Example of base element,* [29].

the network must be provided. This could be completely rigid connections between the fibres and sufficiently high network density to suppress the effect of bending of the fibres.

Since the mid-seventies, it seems that most of the work carried out in the area of geometrical and mechanical properties of random fibre networks has been based on computer simulations.

2.2. Computer simulations

An early example of computer simulation of cellulose fibre structures was presented by Yang in 1975, see [29]. He models paper by a two-dimensional network of randomly distributed fibres with prescribed distribution of length and orientation. He generates network geometries and compares e.g. number of fibre crossings and average free fibre segment length with the values predicted by Kallmes and Corte in [15]. The fibres are ribbon-like with non-zero width, and the part of the fibre area which is in contact with other fibres, the relative bonded area, is computed. Among the geometrical output is also 'percentage of free fibre ends', which is closely related to what in this work is denoted by 'approximate active part', see Section 5.3.

The linear elastic stiffness is calculated by means of the finite element method. The fibres are represented by orthotropic quadrilateral elements, and the areas where fibres overlap are treated as a composite consisting of two layers of orthotropic material. The concept of sub-structuring is used to overcome the problem of poor computer capacity. That is, several small base elements, see e.g. Figure 2.2, are analysed. These elements are then condensed into quadrilateral elements with two degrees of freedom in every corner. The condensed base elements, which have statistical variations in properties, are then used to model the paper sheet. The simulation results show good agreement with experiments performed on kraft paper.

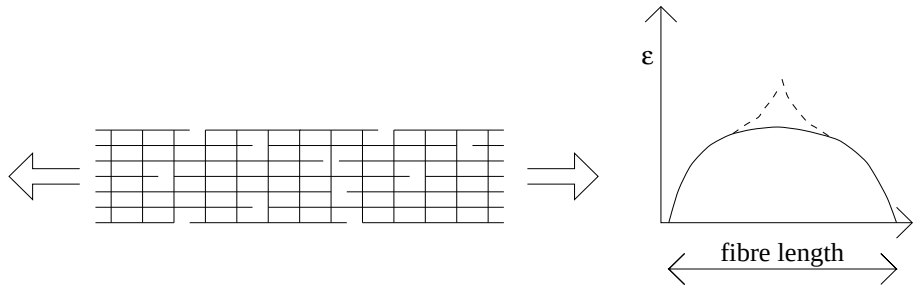

Figure 2.3: *a) Symbolic sketch of network geometry. b) Strain as a function of position in a fibre, revised from* [25].

In 1984 Rigdahl et al., see [25], investigate the axial stress distribution in the fibres of a network by means of finite element simulations. Figure 2.3a shows a simplified sketch of the network geometry considered. It consists of parallel fibres of finite length bonded together through fibres crossing at right angles. The fibres are modelled by linearly elastic straight beam elements, and the fibre-to-fibre bonds are rigid. It is observed that the axial strain in the fibres is smaller than the global strain of the network. The strain in a fibre is zero at the fibre end, rises quite quickly to a plateau value, and, moreover, where the neighboring fibre ends, there is a peak in the strain, see Figure 2.3b. This is because the force transmitted in the neighboring fibre row has to find another way when there is suddenly a discontinuity in the path. The influence of the stiffness of the fibre-to-fibre bond is also investigated. This is done by considering two parallel fibres connected by crossing fibres, fibre-to-fibre bonding not being rigid. One of the fibres is subjected to strain corresponding to the result of one of the previously mentioned analyses, and the transfer of strain to the other fibre as a function of bond stiffness is studied. The result is that the bond stiffness is of small importance unless it is below a certain critical value, in which case the transfer of strain deteriorates rapidly.

In his 1991 thesis, [12], Hamlen treats mechanical properties as well as permeability of paper by means of network modelling. He examines the properties of several regular (triangular, square, hexagonal) and perturbed regular networks, and concludes that the regular networks needed to give satisfactory results when modelling paper are not less computationally expensive than random networks. He therefore chooses to study random networks, in two and three dimensions. The two-dimensional model is composed of linearly elastic straight beams of random distribution and orientation, connected rigidly at crossings. The network geometry is periodic, but the loading conditions are not. The fibres are assigned a breaking stress in simple tension, adjusted in size to reflect breaking of bonds. Simulation results indicate that tensile extension of fibres is the dominant mechanism of force transfer in a fibre network. He also studies the influence of fibre curl by assigning a non-linear Young's modulus to the fibres. Young's modulus is initially set to zero, and when the network has been strained enough to completely straighten out

a fibre, its modulus is reset to a value representative of a straight fibre. Hamlen also proposes a three-dimensional network model for paper, called the sequential deposition model. A network is generated by letting the projection of a fibre in the xy-plane fall down on the already deposited fibres. To begin with, it lands on two points where it first meets previously deposited fibres. Then the fibre continues to descend between the supports to an extent determined by the fibre stiffness through a 'limit angle', possibly making contact with more fibres. In this model the fibre-to-fibre connections are represented by beam elements. The computations prove to be extremely numerically demanding, in spite of the use of a CRAY-2/512. It is concluded that here too the dominant mode of deformation is tension in fibres, followed by shear in connections. To facilitate further 3-d simulations, it is proposed that the modes of deformation of less importance be neglected, and that alternative numerical methods to treat the non-linearity due to the breaking of elements be considered.

In [1], 1991, and [2], 1993, Åström and Niskanen report simulations of fracture in random fibre networks. They examine 2-d random fibre networks of uniform spatial and orientation distribution; the fibres are straight and the fibre-to-fibre bonds are rigid. The mechanical properties of the networks are evaluated as functions of width-to-length ratio of a fibre segment and ratio of network density to percolation network density. They suggest that the specific modulus of elasticity (E of network relative to E of fibre) at low densities is a linear function of network density, and that at high densities it deviates from Cox's homogeneous field value by an amount inversely proportional to network density. Fracture calculations are performed by introducing fracture criteria of fibres and bonds, in terms of axial strain, and performing successive linear calculations where the fractured elements are removed from the structure. The simulations indicate that the strength, in the case of bond breaking, is equal to the product of the elastic modulus of the network and the maximum shear strain that a bond can carry. The character of the stress-strain-curve is discussed in terms of comparisons with predictions from the homogeneous field approximation. Niskanen also provides a review of the knowledge about strength and fracture of paper in [21].

Jangmalm and Östlund in [14], 1995, model paper by a two-dimensional network composed of curled fibres. The circle arc fibres are randomly distributed, and length, width, curl and orientation are described by statistical distributions. The fibre-to-fibre bonds, which occur at a prescribed percentage of the crossings, are rigid. Although the fibres are curled, they are modelled by straight linearly elastic beam elements, but if the free fibre segments are considered to be too long they are divided into several straight elements. The main objective is to investigate the influence of fibre curl on the linear elastic stiffness of a network. This is due to the recently developed possibilities of measuring fibre curl in a pulp with the instrument STFI FiberMaster, referred to in [14]. The influence of fibre length and percentage of bonds in the crossings on the elastic stiffness is also investigated, and some calculations are made using large-strain theory. Those show that the non-linear effect of large strain is rather small. Comparisons of the simulation results are made with

experiments performed on laboratory sheets made of commercial pulps. It turns out that the effect of curl is stronger in the laboratory sheets than is predicted by the model. Several possible reasons for the discrepancies are discussed, among which are the two-dimensional character of the model and that out-of-plane curl is not taken into account.

The Division of Structural Mechanics in Lund has a tradition of studying the fracture of heterogeneous materials. This has led to computer simulation studies in network mechanics, so far reported in [3], [26], [10] and [13].

3. Model

The definition of the model is divided into three parts; fibres, Section 3.1, fibre-to-fibre connections, Section 3.2, and network geometry, Section 3.3. The network geometry parameters describe the way in which the components of the network are assembled into a structure. Assumptions and modelling regarding boundary conditions and loading are discussed in Chapter 6.

3.1. Fibre

A cellulose fibre is complex and strongly affected by the defibration process from wood to single fibre. It is often kinked, curled and with branches of fibrils, and may also have remains of lignin.

In this work the fibre is modelled as a plane beam of circle-arc shape, that is, a curved member that possesses stiffness in the axial and in-plane bending deformation modes. An important special case is zero fibre curvature, that is, straight fibres.

The cross section is arbitrary, although the implementation of the fracture criterion used in the subsequent analyses of network failure is based on a rectangular cross section.

The fibres are assumed to be made of a homogeneous isotropic linearly elastic material, the failure of a fibre occurring when

$$f(\boldsymbol{\sigma}) = 0. \tag{3.1}$$

f is set to

$$f(\boldsymbol{\sigma}) = \max \begin{cases} \dfrac{|\sigma_n|}{\sigma_{ult}} - 1 \\ \dfrac{|\tau|}{\tau_{ult}} - 1 \end{cases}, \tag{3.2}$$

where for a rectangular cross section

$$\sigma_n = \pm \frac{N}{A_f} \pm \frac{M}{I_f} \sqrt{\frac{3I_f}{A_f}}, \tag{3.3}$$

$$\tau = \frac{1.5V}{A_f}. \tag{3.4}$$

Here $|\sigma_n|$ is the maximum absolute value of normal stress in the fibre due to axial force N and bending moment M, σ_{ult} is the ultimate normal stress, $|\tau|$ is the absolute

value of shear stress in the fibre due to shear force V and τ_{ult} is the ultimate shear stress. A_f and I_f denote area and moment of inertia of the beam cross section.

Second order effects are not taken into account; that is, decrease in stiffness due to compressive normal force in a fibre, and possible buckling, are disregarded.

The following parameters define a fibre:

- length, $l_f \in N_{l_f}$
- curvature, $\kappa \in N_\kappa$
- area of cross section, $A_f \in N_{A_f}$
- moment of inertia of cross section, $I_f \in N_{I_f}$
- modulus of elasticity, $E_f \in N_{E_f}$
- ultimate normal stress, $\sigma_{ult} \in N_{\sigma_{ult}}$
- ultimate shear stress, $\tau_{ult} \in N_{\tau_{ult}}$

N represents a distribution of the parameter in question. If the parameter is assumed to be of constant value, N is the Dirac delta distribution.

A value of $\kappa = 0$ corresponds to the case of straight fibres. In experimental situations fibre curl is often quantified by the curl index, c, defined as the distance between the end-points of a fibre divided by fibre length, see Figure 3.1. On assuming

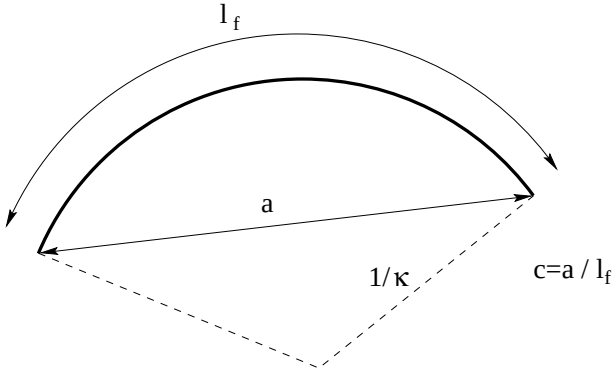

Figure 3.1: *Definition of curl index, c, and curvature, κ.*

constant curvature, the relation between curl index and curvature is:

$$c = \frac{2}{\kappa l_f} \sin(\frac{\kappa l_f}{2}) \tag{3.5}$$

Since it is not possible to solve analytically for κ in this equation, a graphical representation of (3.5) is given in Figure 3.2.

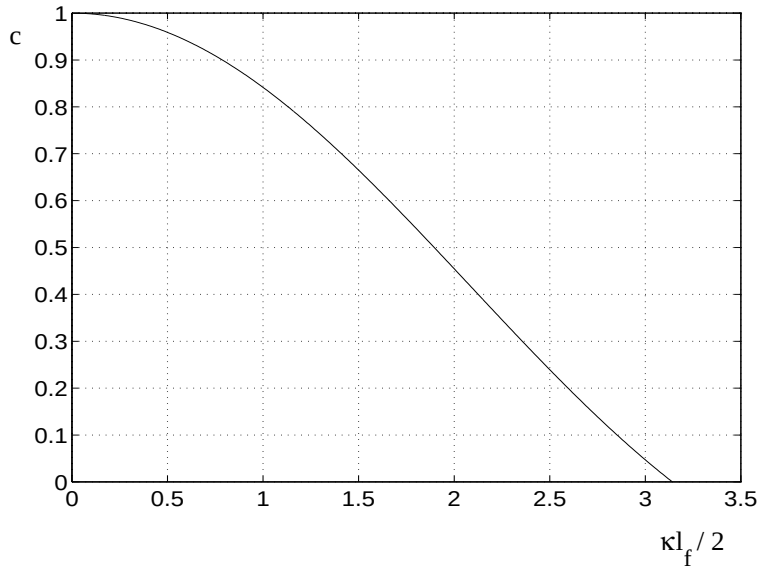

Figure 3.2: *Curl index, c, versus normalized curvature, $\kappa l_f/2$.*

3.2. Fibre-to-fibre connection

The mechanisms of fibre-to-fibre interaction in fluffed dry-shaped cellulose fibre materials are not completely known; probably several mechanisms are acting together. One mechanism is that kinked fibres hook on to each other, another is fibre-to-fibre friction. Chemical attractions may also play a role. When an adhesive aerosol is added during the dry-forming process a different type of material is achieved. The adhesive provides a very strong fibre-to-fibre connection compared to the other suggested mechanisms.

One way of describing this complex reality is to model the interaction in terms of an assemblage of springs. In this work a fibre-to-fibre connection is modelled as three uncoupled springs, one that resists relative motion between the fibres in the x-direction, one in the perpendicular y-direction and one in a rotational mode, ϕ. The springs making up a fibre-to-fibre connection are illustrated symbolically in Figure 3.3. It should be noted that points A and B, which are shown as separate, are really coincident in a model network, and also that the interaction between two fibres occurs where the centroid lines of the two fibres cross. When a fibre-to-fibre connection fails, it does so either completely and in a brittle manner or according to some rule for stick-slip performance or fibre-to-fibre friction, when

$$g(\boldsymbol{F}) = 0, \tag{3.6}$$

where $\boldsymbol{F}$ is the vector of spring forces. In the present implementation the connections

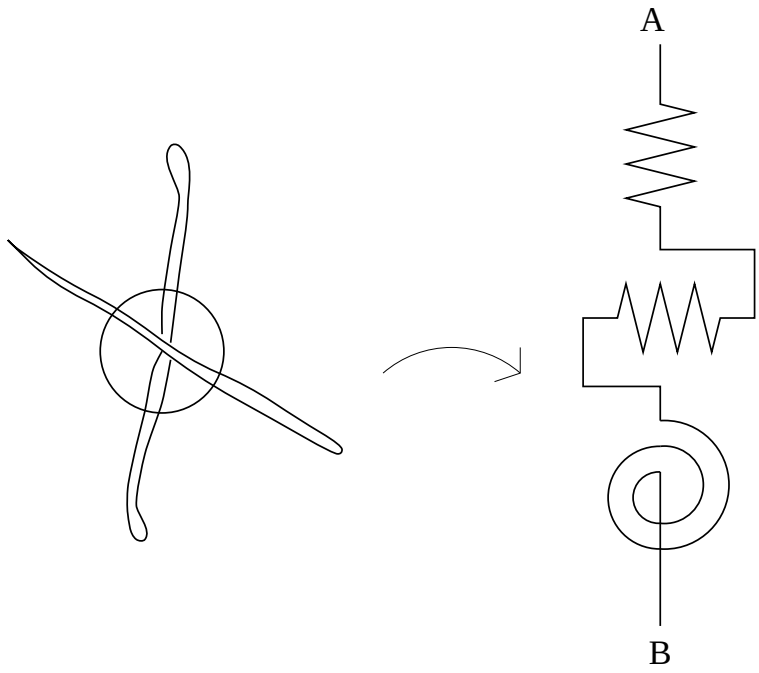

Figure 3.3: *A fibre crossing is modelled with an assemblage of springs.*

are assumed to fail according to a stick-slip performance, and g is set to

$$g(\boldsymbol{F}) = \frac{|F|}{F_{ult}} + \frac{|M|}{M_{ult}} - 1, \tag{3.7}$$

where $|F|$ is the absolute value of the vector sum of the forces in the x- and y-springs, F_{ult} is the ultimate force of the connection, $|M|$ is the absolute value of the moment in the ϕ-spring and M_{ult} is the ultimate moment of the connection.

Figure 3.4 shows the fracture behaviour of a connection, in this case an x-spring, but the same parameters apply to all springs in a connection. Initially the spring is defined by stiffness k_1 and strength F_{ult1}. When the situation $g(\boldsymbol{F}) = 0$ occurs the stiffness is reduced by the factor β_1 and the strength is reduced by the factor β_2. This is repeated $n_s - 1$ times, and when $g(\boldsymbol{F}) = 0$ the n_s:th time the connection fails completely. A special case is $n_s = 1$, completely brittle failure.

The following parameters define a fibre-to-fibre connection:

- initial spring stiffness values in the x-, y- and ϕ-directions, $k_{x1} = k_{y1} \in N_{k_{x1}}$ and $k_{\phi 1} \in N_{k_{\phi 1}}$
- initial ultimate force in connection, $F_{ult1} \in N_{F_{ult1}}$
- initial ultimate moment in connection, $M_{ult1} \in N_{M_{ult1}}$
- reduction of stiffness at slip, $\beta_1 \in N_{\beta_1}$

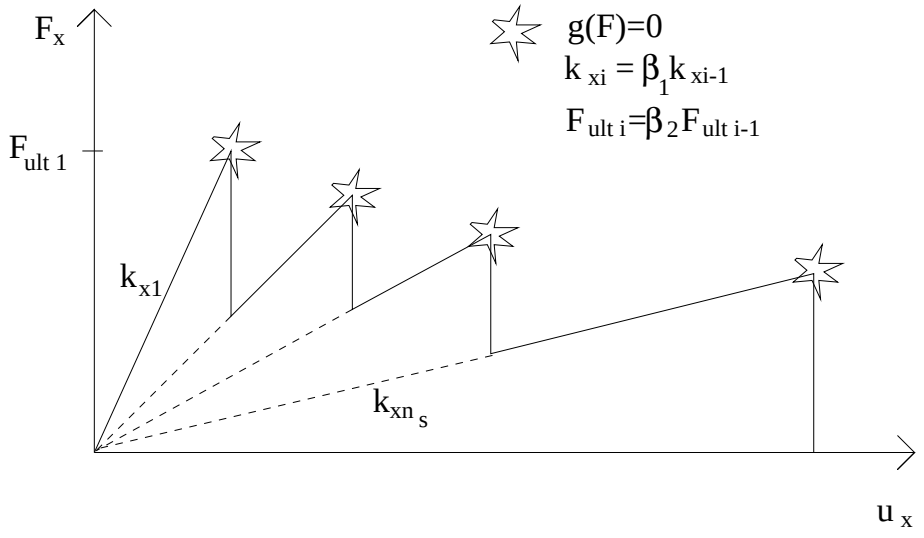

Figure 3.4: *Stick-slip fracture performance of connection.*

- reduction of strength at slip, $\beta_2 \in N_{\beta_2}$
- number of slips before complete failure, $n_s \in N_{n_s}$

3.3. Network geometry

The network structure is obtained by successively placing fibres in the studied area, which is a rectangle of side-lengths L_x and L_y. The fibres are arranged in a random structure according to a specified orientation distribution and rate of heterogeneity.

The rate of heterogeneity can be controlled either by prescribing density variations or restrictions directly or by imposing restrictions on how close to existing fibres a new one is allowed to be placed or must be placed. At least by the latter method, a fairly uniform network can be obtained, even at low density.

In the present implementation the center of the fibre is positioned according to a rectangular distribution, that is with equal probability over the entire area. The heterogeneity parameter $d(\boldsymbol{x})$ is defined as the part of the entire area for which the density is prescribed. Since in this study the fibres are positioned at random, with equal probability over the entire area, $d(\boldsymbol{x})$=1. This means that the network density ρ is prescribed to a certain value in an area of size $L_x L_y$. That is, if the studied area is divided into smaller parts there is a variation in density between the different parts. This issue is further discussed in Section 4.2.

Where two fibres cross each other there is a possibility of interaction between the fibres. At each crossing, the probability of a fibre-to-fibre connection is s. s can be used to symbolically model a three-dimensional network, in which a fibre crossing in the xy-plane does not automatically imply a connection.

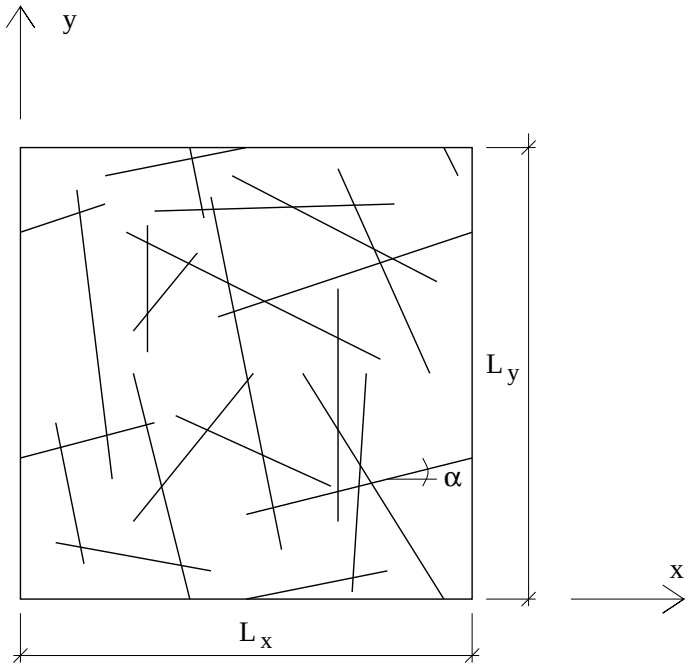

Figure 3.5: *Unit cell of periodic network geometry.*

The number of fibres in the square is determined by the network density, that is total fibre length per unit area.

The network geometry is periodic, such that opposite sides of the area or the volume studied match, as shown in Figure 3.5. This allows the cell under observation to be regarded as one of many identical cells making up a global structure. It also allows periodic boundary conditions to be specified. Those are discussed in Chapter 6.

The following parameters define the network geometry:

- side-lengths of the rectangle that is studied, L_x, L_y
- network density, ρ
- orientation of fibre, $\alpha \in N_\alpha$
- probability of interaction at a fibre crossing, s
- rate of heterogeneity, $d(\boldsymbol{x})$

4. Generation and analysis of network geometry

The analysis of a fibre network can be divided into two main parts: generation and analysis of the network geometry, and analysis of the mechanical properties of the network structure. The first main part, which is described in this chapter, consists of reading input, generating a network, processing it as is described in the following and preparing input data for the subsequent analysis of mechanical properties. It is also desired to have an image of the network, and input data are prepared for a graphic computer code.

A Fortran 90 code has been developed to deal with these tasks; the main structure of the program is illustrated by Figure 4.1.

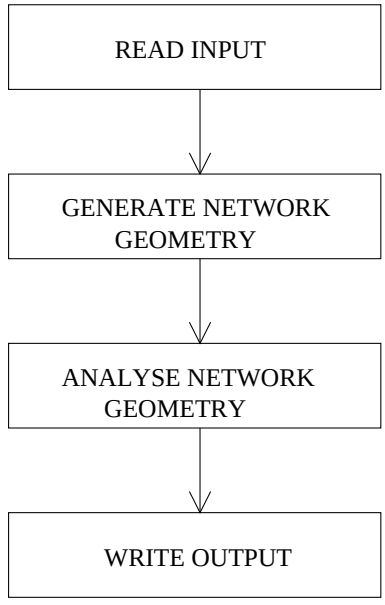

Figure 4.1: *Main structure of program.*

4.1. Input data

All input parameters related to the network are listed in Chapter 3, and in addition to those, the global strain to which the network is to be subjected must be given.

Many of the input parameters are given in terms of a statistical distribution. For each of those a random seed is given. This means that identical networks are reproduced if the same seeds are given in two simulations. This is an almost necessary feature when debugging a program. The statistical distribution is quantified by a cumulative distribution function composed of straight line segments. In Figure 4.2 an example is given of a hypothetical experimental distribution and an approximation of this curve made up of three straight lines. The input to the program is the two vectors of interval boundaries of probability and value of the variable: $(0, p1, p2, p3)$ and $(0, v1, v2, v3)$. If the variable were constant at value v, the vectors would be $(0, 1)$ and (v, v). The maximum number of intervals allowed in the program is twenty. If the random number p is received from the Fortran rectangular pseudo-random number function, the variable is given the value v, as indicated by the dotted line in Figure 4.2.

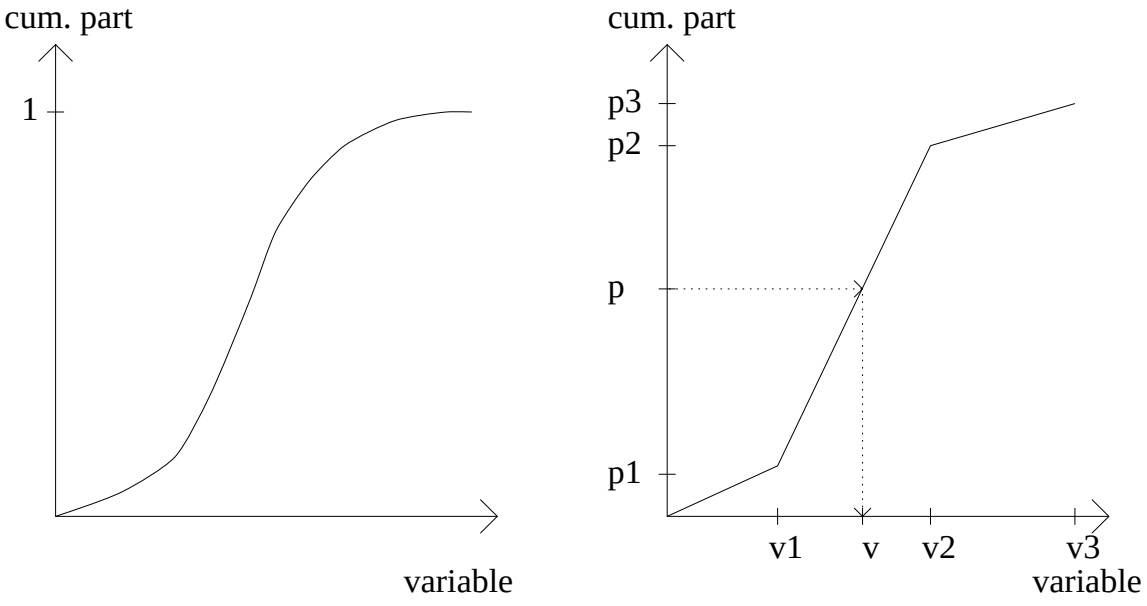

Figure 4.2: *Experimental statistical distribution and approximation made of straight lines.*

4.2. Generation of network geometry

A fibre network is generated by sequentially placing fibres in a rectangle of sidelengths L_x, L_y, until the desired network density is reached. That is, since the number of fibres is an integer, the network density will not be *exactly* as specified. The steps through which one fibre is added to the network are illustrated in Figure 4.3.

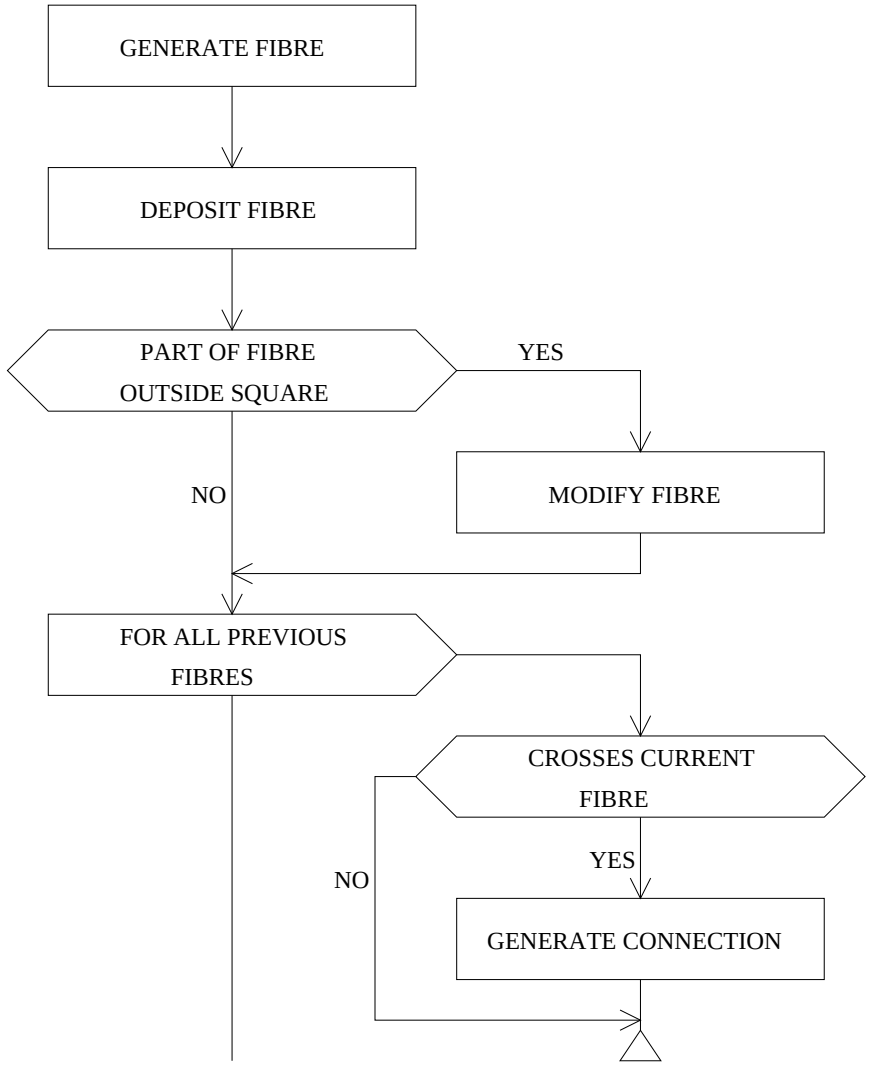

Figure 4.3: *Steps through which one fibre is added to the network.*

A fibre is generated by assigning to it values of all parameters given in Section 3.1 as well as an angle of orientation. This is done according to the principles described in Section 4.1.

The fibre is deposited by placing its mid-point inside the square; for a curled fibre the mid-point is (x_4, y_4) in Figure 4.4. The distribution of fibre mid-points in the square is controlled by the rate-of-heterogeneity parameter, which in the present implementation is such that there is equal probability of a fibre mid-point to be placed everywhere in the square, and the placement of one fibre is independent of the position of the other fibres. This means that a network becomes more heterogeneous as the ratio side-length of square relative to fibre length increases, in the sense that the mass distribution of the network becomes more varied. In a network where $L = l_f$, the network density of the square of area l_f^2 is equal to the prescribed ρ,

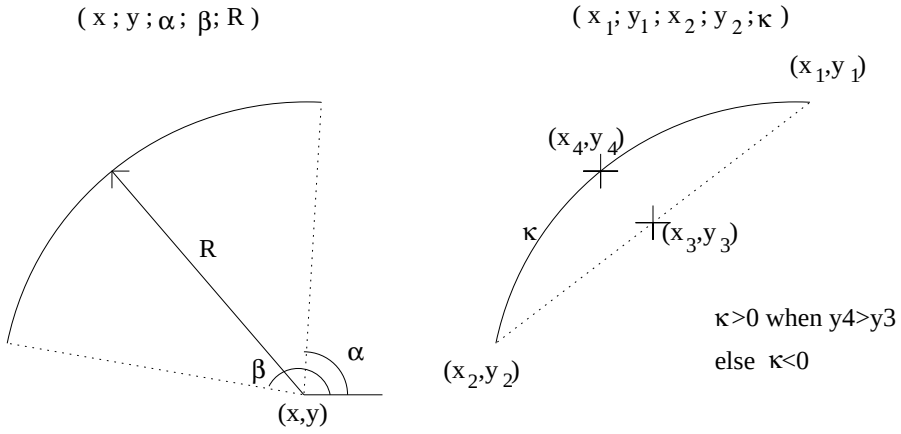

Figure 4.4: *Different ways of defining a circle arc.*

while if $L = 2l_f$, there is variation in network density between the four squares of area l_f^2. The average network density of the squares is however still ρ. This variation in density has a weakening effect on the network, as is discussed in Chapters 7 and 9.

The geometry and location of a fibre, in the case of straight fibres is defined by the coordinates of the end-points of the fibre in a coordinate system with the origin in the lower left corner of the square. The geometry and location of a curled fibre could e.g. be defined by center point, radius of curvature and angles between which the fibre extends, or by end-points of fibre and curvature, including a sign convention, see Figure 4.4. The two representations of a circle arc mentioned are optimal in different situations, and in an effort to minimize computer time at the cost of more stored data all parameters mentioned (except radius of curvature) are stored.

The numerical implementation requires that

$$l_f \kappa \leq \pi, \tag{4.1}$$

implying that the circle arc may at most be a semi-circle.

Since the geometry is supposed to be periodic, the fibre has to be modified if it extends outside the studied square; this modification is illustrated in Figure 4.5. In order to limit the complexity of the program it is required that the fibre length does not exceed twice the side-length of the square.

The modification and detection of crossings for curled fibres and the special case of straight fibres must be treated in separate program units, since the algorithms used for curled fibres degenerate when the radius of curvature approaches infinity. Thus, at the moment, it is not possible to mix curled and entirely straight fibres in the same network, although this is a straightforward generalization to implement.

When a fibre has been deposited, it is checked for crossings against all previous fibres. For the case of straight fibres, this is a matter of solving a linear system of equations in two unknowns. If the fibres are curled, the two fibres might even cross

twice, and the solution algorithm is given in Appendix A . If a crossing is found, a connection is created with the probability s. A connection is created by assigning to it the properties listed in 3.2 and assigning the coordinates of the connection to the fibres involved. Topological information concerning the connection must also be stored, that is, a node number is assigned to the crossing points on each of the two fibres, and it is noted that the connection connects the two nodes.

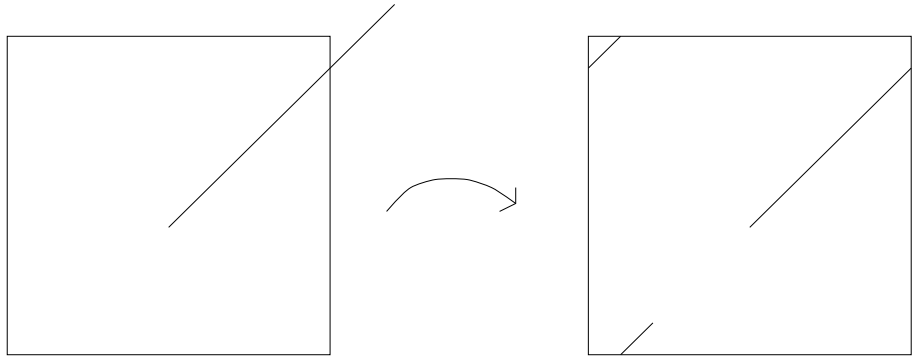

Figure 4.5: *Modification of fibre that extends outside square.*

4.3. Analysis of network geometry

In order to analyse the mechanical properties of the network by means of the finite element method (FEM) the fibres must be divided into beam elements. Each fibre segment between two connections, between a boundary and a connection or between two boundaries of the network is made into one beam element. To be able to do this, the coordinates of the connections on a certain fibre must be sorted in their order along the fibre, since these points are also the end-points of the beam elements. The fibre segments which are free ends of fibres with only one, or possibly no, end being on the boundary or in a connection are not made into beam elements. This is because they would be zero-stress elements that have no influence on the network's behaviour.

Before the network's structure can be analysed in a FEM code it must be established that the network is indeed a connected structure, and not composed of several separate clusters of fibres, since this results in a degenerate system of equations. Usually, this is only a real question in the case of network densities close to the percolation threshold. The algorithm used for this purpose is discussed and presented in Appendix B.

An interesting geometrical property is the active part of a network. By non-active parts, those parts are meant which are in a state of zero stress regardless of loading at the boundary of the network. Most of the zero-stress fibres are removed from the network by not making free fibre ends into beam elements, but there may still be

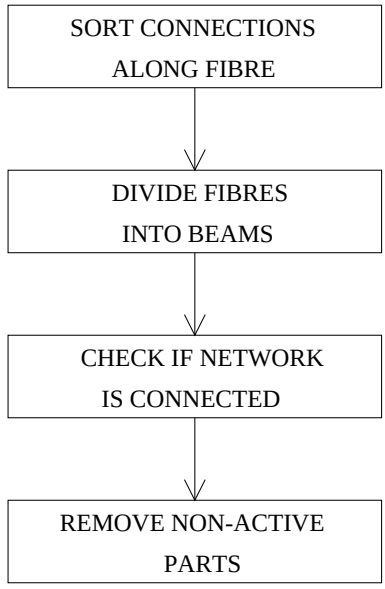

Figure 4.6: *Analysis of network geometry.*

small clusters of fibres not in contact with the rest of the network. These have to be removed as well in order to provide a positive definite system stiffness matrix. In addition to isolated clusters of fibres, there may be clusters of fibres in contact with the rest of the network by only one fibre. Those are zero-stress elements too, and could be removed in order to save degrees of freedom, and to yield the percentage of the fibres that take an active part in the load-carrying structure. If the aim is to obtain a network's stiffness, it is however doubtful if it is worthwhile to remove clusters connected to the rest of the structure by only one fibre, since they are not common in fairly dense networks and detecting them is an extremely time-consuming task. Detection of zero-stress fibres is carried out in connection with the verification of the connectedness of the network, and is also discussed in Appendix B . In Figure 4.7 the non-active parts of a network are shown by dashed lines.

4.4. Output from geometry unit

A number of output parameters are obtained from the analysis of the network geometry. These are

- number of beam elements and total beam length,
- number of connection elements,
- whether the structure is connected or not,
- active part of the network,

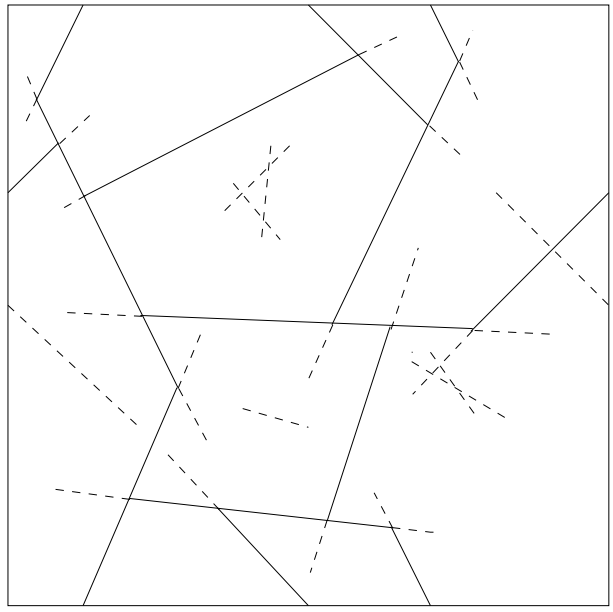

Figure 4.7: *Network with non-active parts dashed.*

- number of active beam elements,
- number of active connection elements,
- number of degrees of freedom in the FEM model.

When the final network structure has been obtained, all necessary data defining the FEM model are written on a file, formatted according to the standards of the FEM code used for the analysis of mechanical properties.

To get an image of the network, data are also written in CAEDOS neutral file format to a file which is used as input file to the Moviestar pre- and post- processing package.

5. Results from analysis of geometry

5.1. Basic example network

Figure 5.3 shows an example of a network structure. When not indicated otherwise the results cited in Chapters 5 and 7 refer to a network having the properties found in the basic example network of Figure 5.3 and Table 5.1. The values in Table 5.1 correspond roughly to mean values of what is known and believed about dry-shaped cellulose fibre materials, although some simplifications have been made to facilitate the simulations.

An example of a fibre length distribution, from [27], of a CTMP fluff (prepared by a chemic-thermo-mechanical process) is given in Figure 5.1. The two curves are cumulative population distribution of fibre length (the percentage of the number of fibres that is shorter than a certain length) and cumulative weighted distribution of fibre length (the percentage of the total fibre length that consists of fibres shorter than a certain length). The arithmetic mean fibre length is $\bar{l}_f^a = 1.34$ mm and the weighted mean fibre length is $\bar{l}_f^w = 2.18$ mm, where

$$\bar{l}_f^a = \frac{\sum_{i=1}^{n_f} l_{fi}}{n_f} \tag{5.1}$$

and

$$\bar{l}_f^w = \frac{\sum_{i=1}^{n_f} l_{fi}^2}{\sum_{i=1}^{n_f} l_{fi}}. \tag{5.2}$$

The mean fibre lengths given above are calculated without taking fibers shorter than 0.11 mm into account; the extremely short fibers are, however, included in the graph. The arithmetic mean fibre length of all fibers is approximately 1.0 mm; the weighted mean fibre length is less affected. For the basic example network we choose to use the arithmetic mean value for fibre length, which means 1.0 mm.

The cross section of a cellulose fibre varies between different tree species as well as between early-wood and late-wood fibres. Figure 5.2 shows a typical fibre cross section and the simplified cross section used in the calculations. When we have decided upon a suitable cross section, the problem remains of deciding in what direction the bending occurs. We choose to study a spiral shaped fibre which has the effective bending stiffness, I_f^e,

$$I_f^e = \frac{b_f^3 h_f^3}{6(b_f^2 + h_f^2)}, \tag{5.3}$$

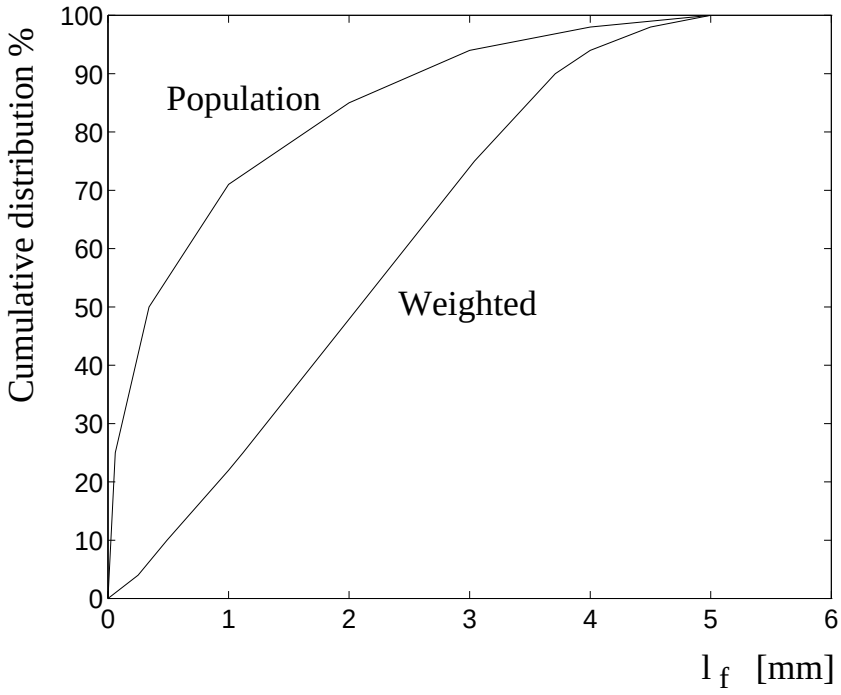

Figure 5.1: *Cumulative distributions of fibre length.*

b_f denoting width and h_f depth of cross section, see Appendix D. For the basic example network we thus use a cross-sectional area of

$$A_f = 7 \cdot 10^{-6} \cdot 35 \cdot 10^{-6} = 2.5 \cdot 10^{-10} \text{ m}^2,$$

and moment of inertia

$$I_f = \frac{(7 \cdot 10^{-6})^3 \cdot (35 \cdot 10^{-6})^3}{6\Big((7 \cdot 10^{-6})^2 + (35 \cdot 10^{-6})^2\Big)} = 20 \cdot 10^{-22} \text{ m}^2.$$

These values of A_f and I_f define a new rectangular effective cross section of

$$h_f^e = \sqrt{\frac{12I}{A}} = 9.8 \cdot 10^{-6} \text{ m},$$

$$b_f^e = \frac{A}{h} = 25.5 \cdot 10^{-6} \text{ m},$$

which is used in fracture simulations where the depth of the cross section enters the calculations.

Young's modulus for a cellulose fibre also varies between different species and early-wood and late-wood, but as a typical value, [16], we take 35 GPa.

Straight fibres are used in the basic example network.

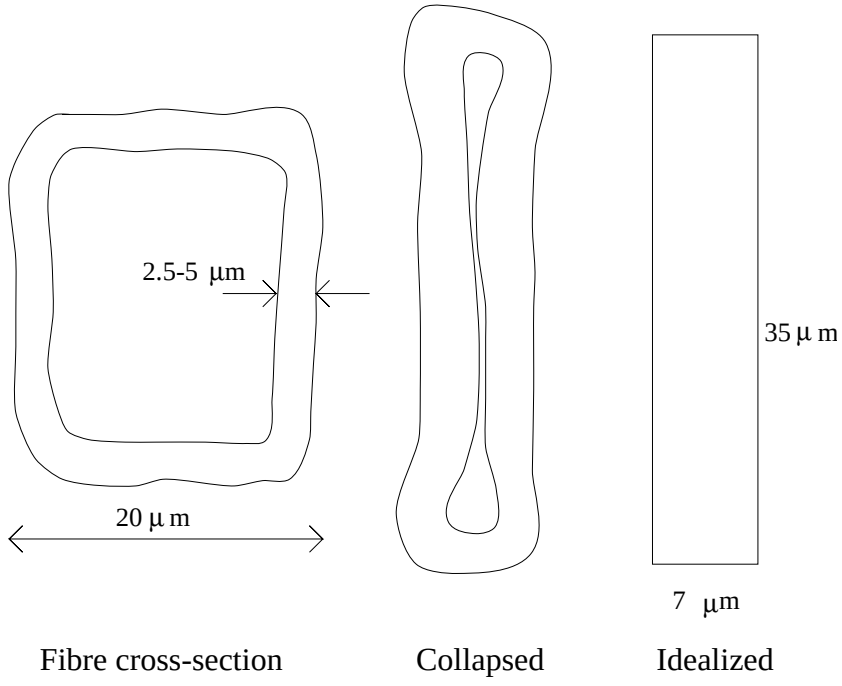

Figure 5.2: *Idealization of fibre cross section.*

The properties of the fibre-to-fibre connections are less known due to experimental difficulties. For the basic example network we take the stiffness k_x to be EA/L for a 1 mm fibre, and k_ϕ to be $4EI/L$ for a 1 mm fibre. Those values correspond to the axial and bending stiffness of a 1 mm fibre. We also assume a connection in every crossing and uniform orientation distribution. ρ is set to 60 mm^{-1}. This means that the mean number of crossings per fibre, obtained as total number of crossings from (2.1) divided by number of fibres and multiplied by two, is 37. This value is probably rather high for a dry-shaped cellulose fibre fluff. The side-length of the studied square is 1.2 mm.

The input parameters of the basic example network are listed in Table 5.1. In Table 5.2 are given some geometry output parameters for the basic example network as well as the mean values from ten different networks that have the same nominal properties as the basic example network. For the definition of active part, see Section 5.3.

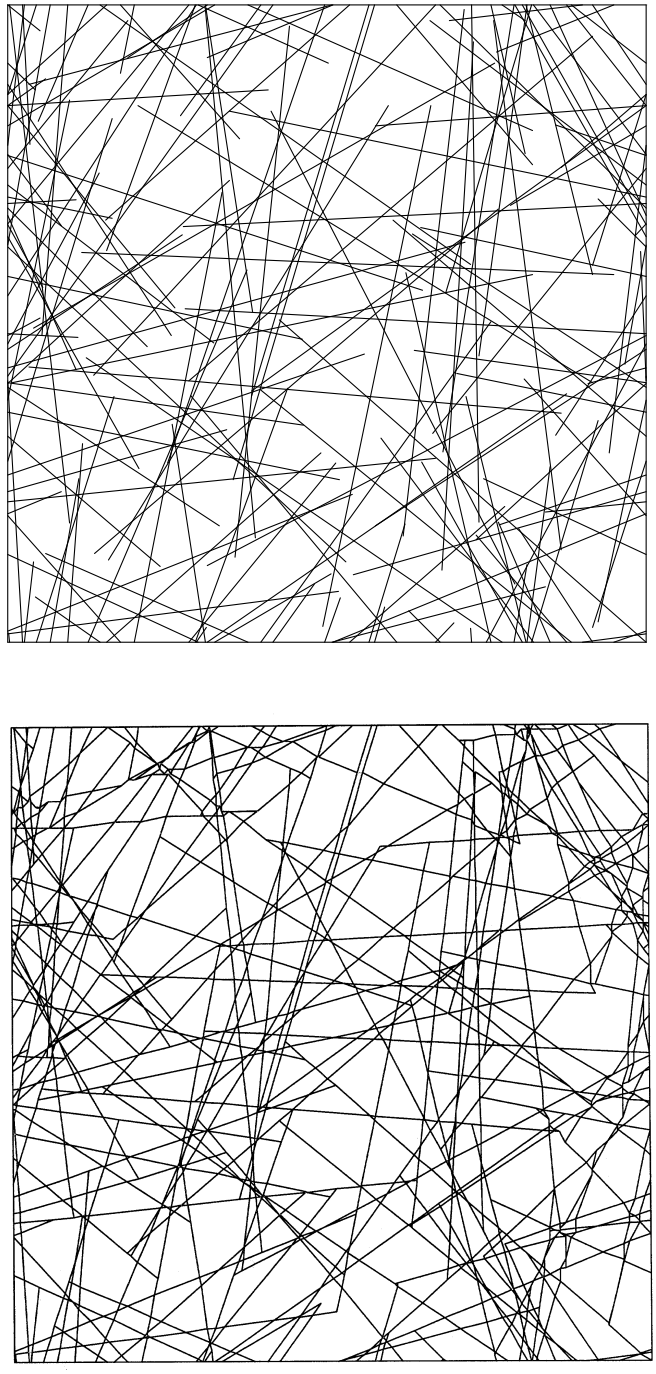

Figure 5.3: *a) Basic example network geometry. b) Basic example network with non-active parts removed.*

Table 5.1: *Input parameters of basic example network.*

Parameter	Value and unit
l_f	1 mm
κ	0 mm^{-1}
A_f	$2.5 \cdot 10^{-10}$ m^2
I_f	$2.0 \cdot 10^{-21}$ m^4
E_f	$35 \cdot 10^9$ Pa
$k_{x1} = k_{y1}$	8750 N/m
$k_{\phi 1}$	$2.8 \cdot 10^{-7}$ Nm/rad
L	1.2 mm
ρ	60 mm^{-1}
N_α	$\frac{1}{\pi}, \quad 0 < \alpha < \pi$
s	1.0
$d(x, y)$	1.0

Table 5.2: *Geometry output for the basic example network and for ten other nominally equal networks generated by other random number seeds.*

Parameter	Result for basic example network	Result for ten nominally equal networks	
		Average value	Standard deviation
Number of fibres	86	86	0
Total fibre length	86 mm	86 mm	0 mm
Number of beam elements	3213	3228	25
Number of connection elements	1603	1612	14
Mean no. of connections/fibre	37	37	0.3
Structure connected	yes	yes, all	
Active part	95.3%	94.8%	0.6%
Number of active beam elements	3211	3223	25
Number of active connection elements	1603	1611	13
Number of degrees of freedom in FEM model	10164	10181	64

5.2. Number of fibre crossings

According to Kallmes and Corte, [15], the average number of fibre crossings, n_c, in a 2D random assembly of fibres of uniform orientation distribution, as given in (2.1) is

$$\bar{n}_c = \frac{(n_f \bar{l}_f)^2 \bar{c}^2}{L^2 \pi}. \tag{5.4}$$

For the basic example network, (5.4) gives 1635 crossings, and this agrees well with the value of 1612 crossings obtained as the mean value for ten simulated networks, see Table 5.2. The standard deviation, as obtained by the numerical simulations, was equal to 14 crossings.

According to (5.4) the number of fibre crossings in a network of straight fibres and uniform orientation distribution depends only on the total fibre length, $n_f \bar{l}_f$, and this agrees well with results from simulations, see Figure 5.4. This diagram shows the number of crossings relative to the number of crossings predicted by (5.4). The network density is 20 mm^{-1}, and the orientation distribution is uniform. The variable on the x-axis is fibre length l_f, that is all networks have the same network density but the networks to the left are made up of many short fibres and the ones to the right are made of fewer but longer fibres. The L/l_f ratio is 1.2, except for fibre lengths 10 and 12mm where it is only 1.0 and 0.8 respectively. This is to avoid an unreasonably large number of crossings. Ten simulations were made for each fibre length considered; the mean value of those is shown as a dashed line. The values are slightly more scattered for the smallest values of l_f, and for $l_f = 12$ mm there is a drop down to $n_c/n_{c_{eq.(5.4)}} = 0.97$.

This is probably because there are so few fibres that the orientation distribution is not uniform any longer, the latter being an assumption used in the derivation of (5.4).

The length of the fibres does not affect the number of crossings, but if the orientation distribution is not uniform, the number of fibre crossings is affected, and in the extreme case when all fibres are parallel there are no crossings at all.

The average curl index, $\bar{c}$, appears in (5.4), but this equation is not believed to be good to use for estimating number of fibre-to-fibre connections in an assembly of curled fibres, since in the derivation of [15], it is disregarded that two curled fibres may cross each other twice (or more). For the case of circle-arc shaped fibres of constant length, a derivation is given here for the number of crossings in a network, and it turns out that in this case the curvature has no influence.

Consider an area A on which n_f circle arcs of constant length l_f and radius of curvature r are placed independently of each other, with equal probability of every position and orientation. A is large compared to the fibre length, and n_f is large.

Firstly, we study two fibres F_1 and F_2, see Figure 5.5. What is the average number of crossings between those two fibres? If the distance between the center points of the circle arcs exceeds $2r$, the average number of crossings is zero. If, on the other hand, the distance is shorter than $2r$ the circles of which the fibres are

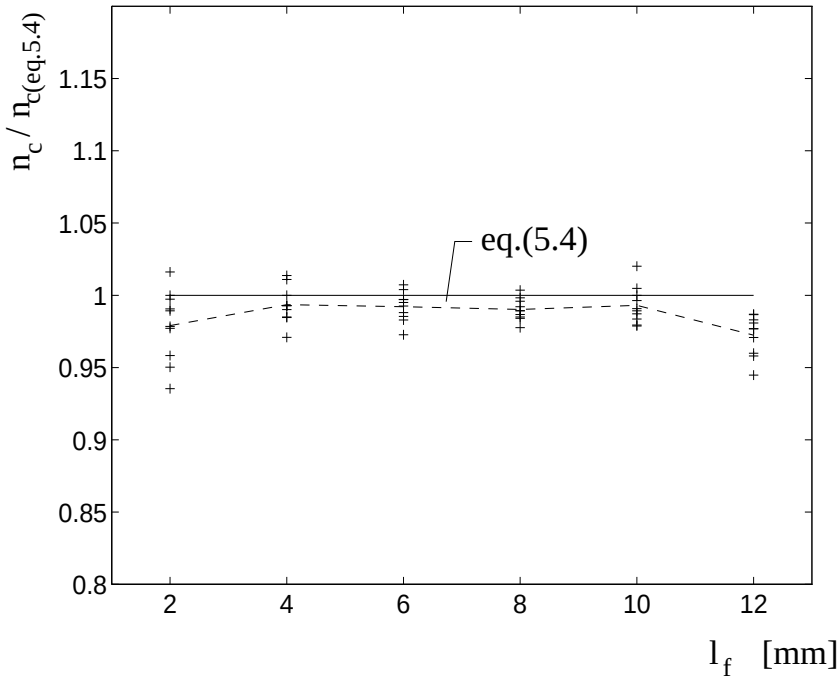

Figure 5.4: *Normalized n_c against fibre length, l_f.*

parts cross. In this case the average number of crossings between the fibres is

$$2\frac{\alpha}{2\pi}\frac{\alpha}{2\pi} = \frac{\alpha^2}{2\pi^2}. \tag{5.5}$$

Thus, the average number of crossings between two fibres in the area A is the probability that the center points are within a distance of $2r$ from each other, times the average number of crossings when they are within this distance:

$$\bar{n}_{c(F_1-F_2)} = \frac{\pi(2r)^2}{A}\frac{\alpha^2}{2\pi^2} \tag{5.6}$$

Fibre F_1 may cross $n_f - 1$ other fibres. This applies to all the n_f fibres, but on multiplying by $(n_f - 1)n_f$ we have counted every crossing twice. To obtain the average total number of crossings in A we therefore multiply $n_{c(F_1-F_2)}$ by

$$\frac{1}{2}(n_f - 1)n_f \approx \frac{n_f^2}{2},$$

which gives

$$\bar{n}_c = \frac{n_f^2}{2}\frac{\pi(2r)^2}{A}\frac{\alpha^2}{2\pi^2} = \frac{(n_f r\alpha)^2}{A\pi} = \frac{(n_f l_f)^2}{A\pi}. \tag{5.7}$$

As indicated before we have arrived at the result that in this case the degree of curl of the fibres has no influence on the number of crossings.

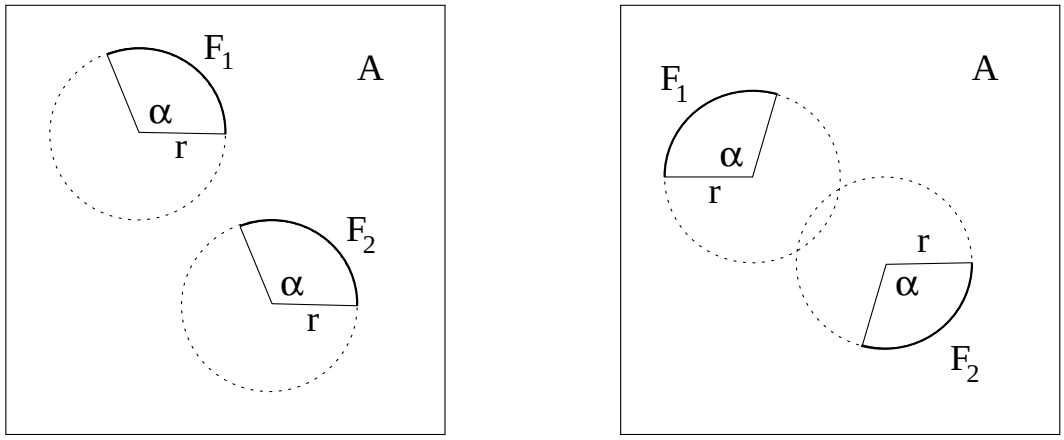

Figure 5.5: *a) Circles not intersecting. b) Circles intersecting.*

A comparison between the two equations (5.4) and (5.7) as well as results from numerical simulations are shown in Figure 5.6. The simulations have the basic example network as starting point, and the curvature and the size of the square, L, are varied.

Four different values of curvature are simulated, 0, 1000, 2000 and 3000 mm^{-1}, 0 mm^{-1} representing a straight fibre and 3000 mm^{-1} being close to a semi-circle. The transition from curvature to curl index can be seen in Figure 3.2.

Three different values of L are considered, representing L/l_f ratios of 0.6, 1.2 and 2.4 respectively. The variation of L means that the assumptions of A and n_f being large are violated to different degrees.

In the diagram the number of crossings relative to the number of crossings predicted by (5.7) is plotted against curl index. The relative standard deviation of the simulation results, which are averages from ten simulations, is 4-9% for L/l_f=0.6 and 1-2% for L/l_f=1.2 and 2.4. (5.4) predicts a pronounced decrease in the number of crossings as the fibres get more curled, while (5.7) proposes the number of crossings to be independent of curl index.

The simulations agree well with (5.7), but as the L/l_f ratio decreases, the results deviate more from the prediction of (5.7), especially for low curl indices. As for Figure 5.4, this is probably because a lower L/l_f ratio means fewer fibres, and fewer fibres means that the orientation distribution tends to be more non-uniform. Another assumption which is not fulfilled when the L/l_f ratio decreases is that of A being large. In the derivation of n_c, a large A is assumed. We can say that A in the simulations is also large by considering many cells, but then we have a periodicity in position and orientation of the fibres which does not agree with the assumptions.

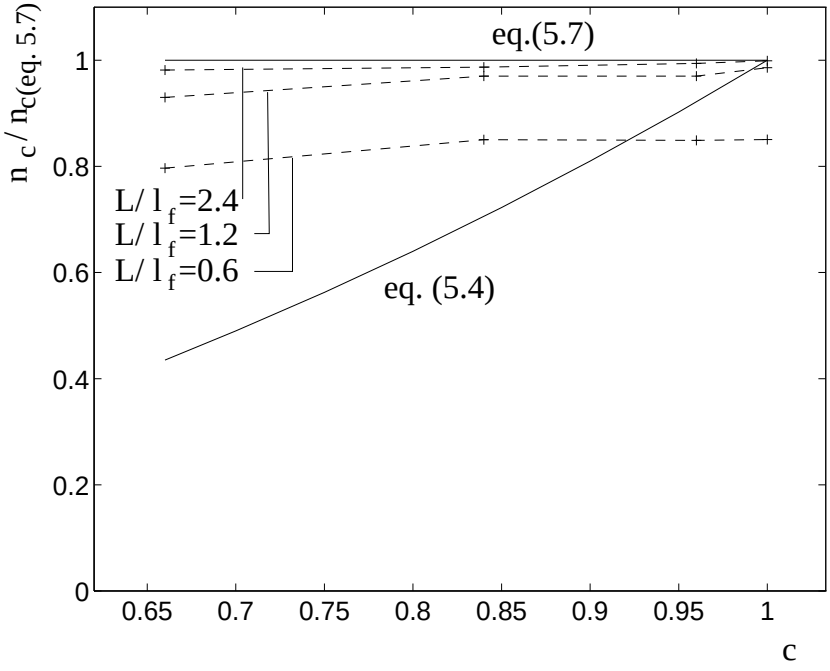

Figure 5.6: *Normalized n_c against curl index, c.*

5.3. Percolation and active part of network

Non-active parts are those parts of a network which are in a state of zero stress regardless of loading at the boundary of the network. In Figure 5.3a the basic example network is shown as it appears when first generated, and Figure 5.3b shows the active part of the network.

As seen in Section 5.2, for a reasonably large network the mean number of fibre crossings in an area depends on the total fibre length only. The active part of the network, however, depends on the length distribution of the fibres as well.

Figure 5.7 shows the active percentage of the network as a function of fibre length for network densities of 2 and 4 mm^{-1}. The values for $\rho = 2$ mm^{-1} are averages from three simulations and the values for $\rho = 4$ mm^{-1} represent one single simulation. The straight fibres have a uniform orientation distribution and interact at all crossings. In each simulation all fibres are of the same length. As the diagram shows, for a given network density a small number of long fibres yields a higher active percentage than does a large number of short fibres.

The marks on the horizontal axis of Figure 5.7 refer to $\rho = 2$ mm^{-1}, and represent non-continuous networks, that is networks that are not connected and hence have no load-bearing function. The fibre length at which a network of given density theoretically reaches the percolation threshold, that is, becomes unconnected, is given in [2] as being

$$l_f \approx 5.7/\rho, \tag{5.8}$$

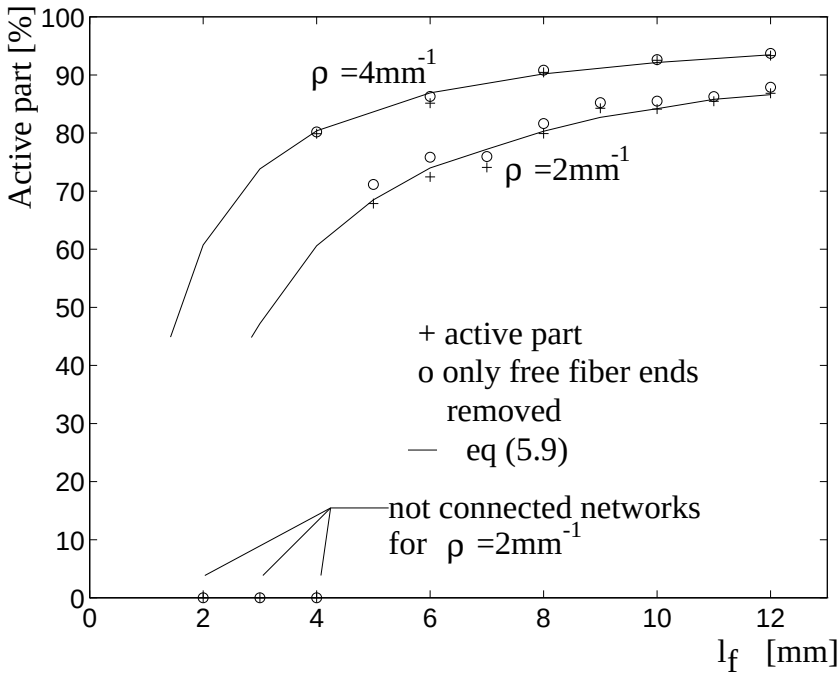

Figure 5.7: *Active part of network against fibre length, l_f.*

which yields $l_f = 2.85$ mm in the case of $\rho = 2$ mm^{-1}, Figure 5.7. Despite this the simulated networks are not connected until $l_f = 5$ mm. This is probably because the results are very scattered as the percolation threshold is approached. Figure 5.7 shows both the active part and the part of the network that is left when only the free fibre ends have been removed. It should be noted that a fibre that is not in contact with any other fibre, as well as clusters composed of only two fibres, are included in free fibre ends in this case, although they can also be viewed as 'isolated clusters'. Even at this low density there is little difference between the two parameters. This indicates that an approximate expression for the active part of a network is fibre length minus length of the two free end segments, divided by fibre length. On using (2.2), this yields the approximate active part, p

$$p = \frac{\bar{l}_f - 2\bar{l}_s}{\bar{l}_f} = 1 - \frac{n_f}{\bar{n}_c} = 1 - \frac{\pi}{\rho \bar{l}_f}. \tag{5.9}$$

This approximate value is shown as a solid line in Figure 5.7, and is supposed to fit to the 'o'-marks, indicating the corresponding numerical results.

When the probability of interaction $s \neq 0$ this equation is modified to

$$p = 1 - \frac{n_f}{s\bar{n}_c} = 1 - \frac{\pi}{s\rho \bar{l}_f}. \tag{5.10}$$

In Figure 5.8 the approximate active part, p, as of (5.9) is given for different network densities. From (5.8), at the percolation threshold fibre length $\rho l_f = 5.7$,

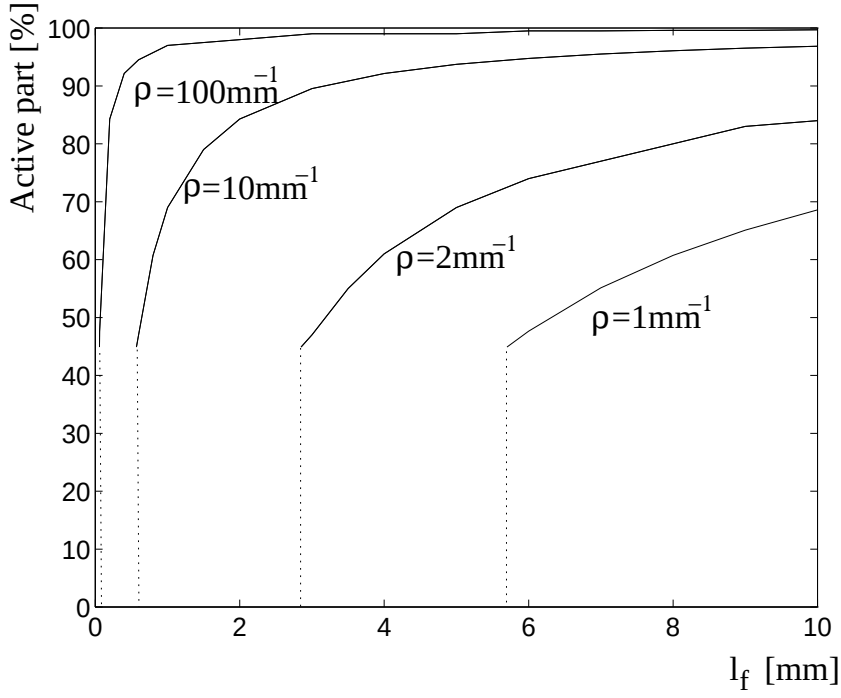

Figure 5.8: *Approximate active part of network against fibre length, l_f.*

which gives $p = 0.45$. That is, at the percolation threshold fibre length, p is the same for all densities, which can also be seen from the diagram. For the higher network densities the active part is rapidly increasing towards 1.0, but for $\rho = 1$ mm^{-1} the increase is slower.

6. FEM model and analysis of stiffness

For describing the pre-fracture global constitutive properties of a network, which is a heterogeneous structure, the terminology of elasticity of continuous media is employed. In linear elasticity of continuous materials, the constitutive properties are contained in the coefficients describing stress as a linear function of strain, i.e. the matrix $\boldsymbol{D}$ in Hooke's law, [19]:

$$\boldsymbol{\sigma} = \boldsymbol{D}\boldsymbol{\epsilon} \tag{6.1}$$

$\boldsymbol{D}$ is symmetric when a strain-energy function exists, [19], and this is assumed to be the case.

The stiffness properties of a fibre network are here characterized by the *D-matrix of a continuous medium which yields the same resultant forces on the boundaries as the network when subjected to the same boundary displacements.*

The finite element method (FEM), see [22], [30], is used to obtain the stiffness properties. This is done by dividing the network into beam and connection elements (fibre segments and fibre-to-fibre connections), computing the element stiffness matrix for each element, and assembling all element stiffness matrices into a global system stiffness matrix. The element stiffness matrices for straight and curved beam elements and for the connection element are given in the next section. The next step is to prescribe the load on the structure. In this case the network is loaded by prescribing a global strain, that is boundary displacements. This is done according to the principles in Section 6.2. The system of equations is then solved, Section 6.3, and the resultant forces and $\boldsymbol{D}$ are evaluated as shown in Section 6.4.

$\boldsymbol{D}$ obtained from a simulation contains nine constants, of which only six are independent due to symmetry of $\boldsymbol{D}$. To reduce the number of independent constants to that of an isotropic material, that is two, a method of approximation is given in Section 6.6. The corresponding method for orthotropic material is given in Section 6.7.

The computer code used for the FEM calculations is CALFEM, [5], which works in a Matlab, [20], environment, supplemented with some special functions.

6.1. Element stiffness matrices

The element stiffness matrix $\boldsymbol{K}_e$ gives the reaction forces $\boldsymbol{f}$ when the element is subjected to displacements $\boldsymbol{u}$, that is

$$\boldsymbol{K}_e\boldsymbol{u} = \boldsymbol{f}, \tag{6.2}$$

where $\boldsymbol{u}$ is the vector of displacements in the directions of the degrees of freedom of the element, see Figures 6.1-6.3, and $\boldsymbol{f}$ is the corresponding force vector.

The stiffness matrix for a plane straight beam element, Figure 6.1, can e.g. be found in [22]. On assuming small strain, neglecting shear deformation and assuming

Figure 6.1: *Straight beam element with degrees of freedom* $u_1 \dots u_6$.

that plane sections perpendicular to the beam axis remain plane during deformation, the stiffness matrix for a straight beam element is

$$\boldsymbol{K}_e = \begin{bmatrix} \frac{EA}{L} & 0 & 0 & -\frac{EA}{L} & 0 & 0 \\ 0 & \frac{12EI}{L^3} & \frac{6EI}{L^2} & 0 & -\frac{12EI}{L^3} & \frac{6EI}{L^2} \\ 0 & \frac{6EI}{L^2} & \frac{4EI}{L} & 0 & -\frac{6EI}{L^2} & \frac{2EI}{L} \\ -\frac{EA}{L} & 0 & 0 & \frac{EA}{L} & 0 & 0 \\ 0 & -\frac{12EI}{L^3} & -\frac{6EI}{L^2} & 0 & \frac{12EI}{L^3} & -\frac{6EI}{L^2} \\ 0 & \frac{6EI}{L^2} & \frac{2EI}{L} & 0 & -\frac{6EI}{L^2} & \frac{4EI}{L} \end{bmatrix}. \tag{6.3}$$

Here E denotes Young's modulus of the beam material, A and I denote area and moment of inertia of the cross section respectively, and L denotes length of the beam element.

The stiffness matrix for a curved beam element of constant curvature is derived in [18], from where (6.6) - (6.9) are cited. For a curved beam a modified bending stiffness, J, is used instead of moment of inertia, I.

$$J = \int_A \frac{(r-R)^2}{r/R} \mathrm{d}A, \tag{6.4}$$

where r denotes radius of the circle through an arbitrary point on the cross section and R is the radius of the centroid line. For the case of rectangular cross section, J is, see [8],

$$J = R^3 b \ln\left(\frac{2R+h}{2R-h}\right) - R^2 bh = I\left(1 + \frac{3}{5}\left(\frac{h}{2R}\right)^2 + \frac{3}{7}\left(\frac{h}{2R}\right)^4 + \cdots\right), \tag{6.5}$$

where I is moment of inertia of the cross section and b and h denote width and depth of the cross section. For common values of the ratio h/R, the serial expansion converges fast, and only the first few terms need to be considered.

To form the stiffness matrix $\boldsymbol{K}_e$ matrices $\boldsymbol{G}$ and $\boldsymbol{D}$ are evaluated as follows, where R, θ and a are defined in Figure 6.2, and E and A denote Young's modulus of material and area of cross section.

$$\boldsymbol{G} = \begin{bmatrix} -1 & 0 & 0 & 1 & 0 & 0 \\ 0 & 0 & -a & 0 & 0 & a \\ 0 & 1 & a & 0 & -1 & a \end{bmatrix}, \tag{6.6}$$

$$\boldsymbol{D} = \begin{bmatrix} H_{22}/H & -H_{12}/H & 0 \\ -H_{12}/H & H_{11}/H & 0 \\ 0 & 0 & 1/H_{33} \end{bmatrix}, \tag{6.7}$$

where

$$\begin{aligned} H_{11} &= 2\left(\frac{R}{EA} + \frac{R^3}{EJ}\right)\theta\cos^2\theta + \frac{R^3}{EJ}(\theta - 3\sin\theta\cos\theta) \\ H_{22} &= 2\left(\frac{R}{EA} + \frac{R^3}{EJ}\right)\theta\sin^2\theta \\ H_{12} &= 2\left(\frac{R}{EA} + \frac{R^3}{EJ}\right)\theta\sin\theta\cos\theta - 2\frac{R^3}{EJ}\sin^2\theta \\ H_{33} &= \frac{R^3}{EJ}(\theta - \sin\theta\cos\theta) \\ H &= H_{11}H_{22} - H_{12}^2. \end{aligned} \tag{6.8}$$

This finally gives $\boldsymbol{K}_e$, in local coordinates:

$$\boldsymbol{K}_e = \boldsymbol{G}^T\boldsymbol{D}\boldsymbol{G} \tag{6.9}$$

A fibre-to-fibre connection is modelled by three uncoupled springs and with the spring stiffnesses k_x, k_y, k_ϕ according to Figure 6.3, the stiffness matrix for the connection element is

$$\boldsymbol{K}_e = \begin{bmatrix} k_x & 0 & 0 & -k_x & 0 & 0 \\ 0 & k_y & 0 & 0 & -k_y & 0 \\ 0 & 0 & k_\phi & 0 & 0 & -k_\phi \\ -k_x & 0 & 0 & k_x & 0 & 0 \\ 0 & -k_y & 0 & 0 & k_y & 0 \\ 0 & 0 & -k_\phi & 0 & 0 & k_\phi \end{bmatrix}. \tag{6.10}$$

In Figure 6.3 the connection element has been separated into three figures, to make the illustration clearer.

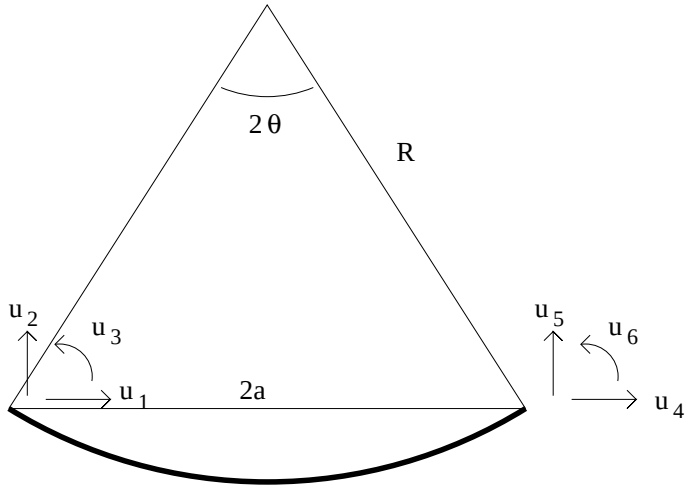

Figure 6.2: *Curved beam element.*

All the element stiffness matrices given above are referred to a coordinate system with axes parallel to the element's degrees of freedom, e.g. (u_1, u_2). In the fibre network the beams may have an orientation that differs from the global coordinate axes. When this is the case, the element stiffness matrix has to be transformed, see [22]:

$$\boldsymbol{K}_e^g = \boldsymbol{A}^T \boldsymbol{K}_e^l \boldsymbol{A}, \tag{6.11}$$

where superscript g denotes global, superscript l denotes local,

$$\boldsymbol{A} = \begin{bmatrix} \cos\phi & \sin\phi & 0 & 0 & 0 & 0 \\ -\sin\phi & \cos\phi & 0 & 0 & 0 & 0 \\ 0 & 0 & 1 & 0 & 0 & 0 \\ 0 & 0 & 0 & \cos\phi & \sin\phi & 0 \\ 0 & 0 & 0 & -\sin\phi & \cos\phi & 0 \\ 0 & 0 & 0 & 0 & 0 & 1 \end{bmatrix} \tag{6.12}$$

and ϕ denotes the counter-clockwise angle from the global to the local x-axis.

The stiffness matrix of the connection element always refers to the global coordinate axes, that is, the directions of the k_x- and k_y-spring are independent of the directions of the crossing beam elements. When all the beam elements have been transformed into the global coordinate directions, each element stiffness matrix is assembled into the global stiffness matrix.

6.2. Methods of applying strain

To obtain the response of a network, it is subjected to deformations corresponding to various modes of strain, and the resulting forces on the boundaries of the network are registered.

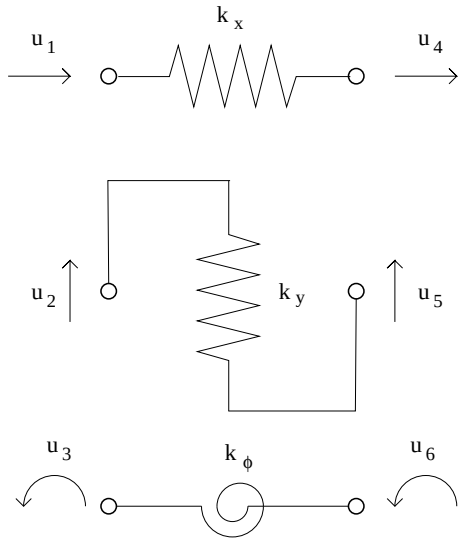

Figure 6.3: *Connection element.*

A deformation to which the network is subjected, reflects a certain global mean strain, $\boldsymbol{\epsilon}$, of the cell. There are several different methods of applying such a mean strain. A natural concept would be to imitate the situation when testing a fibre material in the laboratory. This could be a strip of material clamped at the ends and otherwise free, see Figure 6.4. This method would facilitate direct comparison

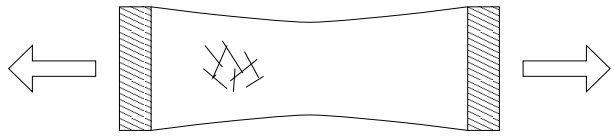

Figure 6.4: *Fibre network in simple tension test.*

between the results obtained from tests and simulations respectively. One problem is, however, that with today's computer performance it is not feasible to carry out simulations on a piece of material as large as a test specimen. It is also complicated to evaluate the stiffness parameters in this deformation mode: for example, how large is the contraction in this case when contraction is prevented at the edges and becomes gradually more free towards the centre?

To avoid these problems a concept of cyclic geometry and boundary conditions is employed. The essence of those is that the network cell under observation is regarded as one of many identical cells making up a global network structure of infinite size. This leads to certain continuity requirements, namely that the cells are to match also in a deformed condition. Two different sets of cyclic boundary conditions are considered, both of which fulfill the necessary continuity requirements. In the first

set of boundary conditions, denoted below by S for straight, the boundaries are forced to remain straight during deformation, and in the second set, denoted below by C for curved, the boundaries are allowed to deform. In Figure 6.5, a cell subjected to strain $\boldsymbol{\epsilon} = (\epsilon_0, 0, 0)$ is shown for the cases of boundary conditions S and C.

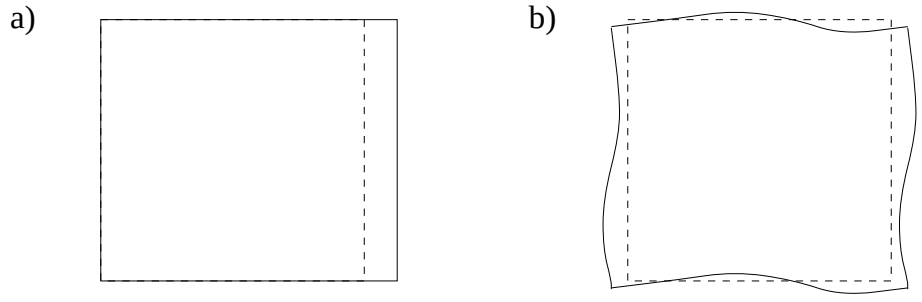

Figure 6.5: *Cell subjected to* $\epsilon = (\epsilon_0, 0, 0)$ *for a) boundary conditions S, b) boundary conditions C.*

For boundary conditions S, strain $\boldsymbol{\epsilon} = (\epsilon_x, \epsilon_y, \gamma_{xy})$ is applied by prescribing the following displacements and rotation to every node i at the boundary:

$$\begin{bmatrix} u_i \\ v_i \\ \theta_i \end{bmatrix} = \begin{bmatrix} x_i & 0 & y_i \\ 0 & y_i & 0 \\ 0 & 0 & -\sin^2 \alpha_i \end{bmatrix} \begin{bmatrix} \epsilon_x \\ \epsilon_y \\ \gamma_{xy} \end{bmatrix} \tag{6.13}$$

Here (x_i, y_i) are the coordinates of the boundary node, when the origin is in the lower left corner of the network and α_i is the inclination of the fibre. The considerations that lead to the factor $-\sin^2 \alpha_i$ are presented in Appendix C.

For the case of boundary conditions C, displacements are specified in the manner given by the following equation:

$$\begin{bmatrix} u_2 - u_1 \\ v_2 - v_1 \\ \theta_2 - \theta_1 \\ u_4 - u_3 \\ v_4 - v_3 \\ \theta_4 - \theta_3 \end{bmatrix} = \begin{bmatrix} L_x & 0 & 0 \\ 0 & 0 & 0 \\ 0 & 0 & 0 \\ 0 & 0 & L_y \\ 0 & L_y & 0 \\ 0 & 0 & 0 \end{bmatrix} \begin{bmatrix} \epsilon_x \\ \epsilon_y \\ \gamma_{xy} \end{bmatrix} \tag{6.14}$$

The subscript 1 denotes nodes at the left boundary of the network and subscripts 2, 3 and 4 denote nodes at the right, lower and upper boundaries of the network respectively; see also Figure 6.6. L_x and L_y are side-lengths of the rectangle in the x- and y-directions.

The consequences of the different kinds of boundary conditions are further discussed in Section 6.4.

6.3. Solution of the system of equations

The system of equations for boundary conditions S is straightforward to solve. All boundary nodes have prescribed values of displacement, and thus there are reaction forces on all the boundary nodes and no reaction forces occur on any interior node.

For boundary conditions C the prescribed displacements are specified in terms of relations between different degrees of freedom, that is constraints. The constrained degrees of freedom are removed from the system of equations, see [26]. The original system of equations is:

$$\boldsymbol{K}\boldsymbol{u} = \boldsymbol{f} \tag{6.15}$$

The constraints can be formulated as relations between a full and a reduced displacement vector $\boldsymbol{u}$ and $\boldsymbol{u}_{red}$,

$$\boldsymbol{u} = \boldsymbol{B}\boldsymbol{u}_{red} + \boldsymbol{C}. \tag{6.16}$$

For the nodes located along the boundaries, equation (6.14) rewritten in the form of (6.16) is

$$\begin{bmatrix} u_1 \\ u_2 \\ v_1 \\ v_2 \\ \theta_1 \\ \theta_2 \\ u_3 \\ u_4 \\ v_3 \\ v_4 \\ \theta_3 \\ \theta_4 \end{bmatrix} = \begin{bmatrix} 1 & 0 & 0 & 0 & 0 & 0 \\ 1 & 0 & 0 & 0 & 0 & 0 \\ 0 & 1 & 0 & 0 & 0 & 0 \\ 0 & 1 & 0 & 0 & 0 & 0 \\ 0 & 0 & 1 & 0 & 0 & 0 \\ 0 & 0 & 1 & 0 & 0 & 0 \\ 0 & 0 & 0 & 1 & 0 & 0 \\ 0 & 0 & 0 & 1 & 0 & 0 \\ 0 & 0 & 0 & 0 & 1 & 0 \\ 0 & 0 & 0 & 0 & 1 & 0 \\ 0 & 0 & 0 & 0 & 0 & 1 \\ 0 & 0 & 0 & 0 & 0 & 1 \end{bmatrix} \begin{bmatrix} u_1 \\ v_1 \\ \theta_1 \\ u_3 \\ v_3 \\ \theta_3 \end{bmatrix} + \begin{bmatrix} 0 \\ L_x\epsilon_x \\ 0 \\ 0 \\ 0 \\ 0 \\ 0 \\ L_y\gamma_{xy} \\ 0 \\ L_y\epsilon_y \\ 0 \\ 0 \end{bmatrix}. \tag{6.17}$$

Insertion of (6.16) in (6.15) gives

$$\boldsymbol{K}\boldsymbol{B}\boldsymbol{u}_{red} + \boldsymbol{K}\boldsymbol{C} = \boldsymbol{f}. \tag{6.18}$$

In order to obtain a symmetric stiffness matrix, all terms are multiplied by $\boldsymbol{B}^T$:

$$\boldsymbol{B}^T\boldsymbol{K}\boldsymbol{B}\boldsymbol{u}_{red} = \boldsymbol{B}^T\boldsymbol{f} - \boldsymbol{B}^T\boldsymbol{K}\boldsymbol{C} \tag{6.19}$$

Defining

$$\boldsymbol{K}_{red} = \boldsymbol{B}^T\boldsymbol{K}\boldsymbol{B} \tag{6.20}$$

$$\boldsymbol{f}_{red} = \boldsymbol{B}^T\boldsymbol{f} - \boldsymbol{B}^T\boldsymbol{K}\boldsymbol{C}, \tag{6.21}$$

we now have

$$\boldsymbol{K}_{red}\boldsymbol{u}_{red} = \boldsymbol{f}_{red}. \tag{6.22}$$

This system of equations is solved for $\boldsymbol{u}_{red}$, $\boldsymbol{u}$ is obtained from (6.16) and the reaction forces are obtained from (6.15).

In (6.22) rigid body translation must be prevented, by e.g. prescribing zero displacement in x- and y-directions in an interior node. Rigid body rotation is prevented automatically by the constraints; since e.g. v_1 and v_2 must always be the same, the cell is not able to rotate.

As in the case of boundary conditions S, there are reaction forces on all boundary nodes, and none on the interior nodes. Moreover, the reaction forces in two opposite nodes are always equal in magnitude and opposite in direction. Should reaction forces occur in the interior node prescribed to zero translation, this indicates lack of equilibrium due to numerical reasons or some other error.

6.4. Evaluation of resultant forces and D-matrix

To obtain the D-matrix of the equivalent continuous material, the network is successively subjected to three modes of deformation, corresponding to the three components of in-plane strain. First the strain $\boldsymbol{\epsilon} = (1, 0, 0)$ is applied, representing extension in the x-direction, without either strain in the y-direction or shear strain. The resultant forces on the network are registered and are divided by side-length to obtain stress. This means that the unit of stress for a network is N/m. The procedure is illustrated in Figure 6.6 . Note that moments in the boundary nodes are omitted in the figure.

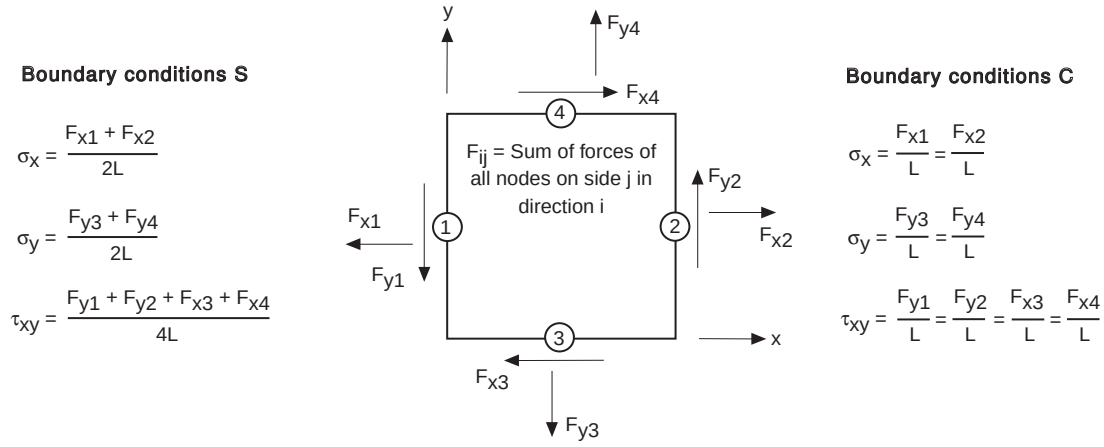

Figure 6.6: *Evaluation of stresses.*

From (6.1) it follows that

$$\begin{bmatrix} \sigma_x \\ \sigma_y \\ \tau_{xy} \end{bmatrix} = \begin{bmatrix} D_{11} & D_{12} & D_{13} \\ D_{12} & D_{22} & D_{23} \\ D_{13} & D_{23} & D_{33} \end{bmatrix} \begin{bmatrix} 1 \\ 0 \\ 0 \end{bmatrix} = \begin{bmatrix} D_{11} \\ D_{12} \\ D_{13} \end{bmatrix}. \tag{6.23}$$

Thus, the first column of $\boldsymbol{D}$ is equal to the registered stress vector. The two remaining columns of $\boldsymbol{D}$ are obtained analogously through applying $\boldsymbol{\epsilon} = (0, 1, 0)$ (extension in the y-direction) and $\boldsymbol{\epsilon} = (0, 0, 1)$ (pure shear).

For the case of boundary conditions C the reaction forces in two opposite boundary nodes are equal in magnitude, and opposite in direction. This means that the sums of normal forces on opposite boundaries are equal, and the resultants are situated exactly opposite each other. In Figure 6.6 this means that F_{x1} and F_{x2} as well as F_{y3} and F_{y4} are collinear. Since the moments in the boundary nodes are also equal in size and opposite in direction, two by two, the total moment on the network from moments in boundary nodes is zero. For the global moment equilibrium to be satisfied it is then necessary that the forces F_{y1}, F_{y2} and F_{x3}, F_{x4} are of equal magnitude. The $\boldsymbol{D}$ obtained from boundary conditions C is automatically symmetric.

When boundary conditions S are used the forces in opposite nodes are not equal, and thus F_{x1} and F_{x2} are not collinear, and F_{y1}, F_{y2}, F_{x3} and F_{x4} need not be the same. Despite this, the global equilibrium of the cell is of course satisfied. When requiring that the boundaries remain straight, the network is not allowed to deform in the way that is most natural to it. One could imagine a rigid frame being attached onto the network, which transfers the forces needed for the prescribed deformation to be possible. Intuitively this stiffens up the structure. A somewhat absurd consequence of forces in opposite nodes not being equal, is that if one imagines two nearby cells, the forces are not the same in the two fibre ends that are supposed to be attached to each other in the global network. $\boldsymbol{D}$ obtained from boundary conditions S is not symmetric. Since we want a symmetric $\boldsymbol{D}$, the mean values across the diagonal are taken as $\boldsymbol{D}$.

6.5. Anisotropic, orthotropic and isotropic materials

A linear elastic continuous material can be classified into different categories with respect to symmetries in the material. If there are no preferred directions the material is isotropic, otherwise it is anisotropic and $\boldsymbol{D}$ contains in the most general case six independent constants:

$$\boldsymbol{D} = \begin{bmatrix} D_{11} & D_{12} & D_{13} \\ D_{12} & D_{22} & D_{23} \\ D_{13} & D_{23} & D_{33} \end{bmatrix} \tag{6.24}$$

In case of symmetry with respect to two perpendicular axes, the material is orthotropic and the number of independent constants is reduced to four. On assuming plane stress this gives

$$\boldsymbol{D} = \frac{1}{1 - \nu_{xy}\nu_{yx}} \begin{bmatrix} E_x & E_x\nu_{yx} & 0 \\ E_y\nu_{xy} & E_y & 0 \\ 0 & 0 & G_{xy}(1 - \nu_{xy}\nu_{yx}) \end{bmatrix}, \qquad E_x\nu_{yx} = E_y\nu_{xy}. \tag{6.25}$$

The simplest possible material is isotropic, and has the same properties in every direction. In this case $\boldsymbol{D}$ contains only two independent constants, namely modulus of elasticity E and Poisson's ratio ν:

$$\boldsymbol{D} = \frac{E}{1-\nu^2}\begin{bmatrix} 1 & \nu & 0 \\ \nu & 1 & 0 \\ 0 & 0 & \dfrac{1-\nu}{2} \end{bmatrix} \tag{6.26}$$

For an isotropic material, $\boldsymbol{D}$ is the same for every material orientation, while for anisotropic materials $\boldsymbol{D}$ depends on the orientation of the material. The orthotropic $\boldsymbol{D}$ given above refers to the case when the coordinate axes coincide with the principal directions of the material.

For a three-dimensional isotropic material, it is known that certain restrictions can be imposed on the elastic moduli. Assuming positive definiteness of the strain energy, [19] leads to the conditions

$$E > 0 \quad \text{and} \quad -1 < \nu < \frac{1}{2}. \tag{6.27}$$

Even if a two-dimensional network is approximately isotropic in its own plane, there is no reason to believe that it has the same properties in the out-of-plane direction. Because of this, the restrictions given above are not generally applicable to the moduli of two-dimensional networks.

Although a network is in general anisotropic, one would expect nearly transversely isotropic behaviour for fairly dense two-dimensional networks, if the fibres have a uniform orientation distribution. If the orientation distribution N_α is symmetric with respect to two perpendicular axes, nearly orthotropic network properties can be expected.

If the network is to be represented as an anisotropic material, the $\boldsymbol{D}$ obtained from the simulations needs no further processing, except for symmetrization for boundary conditions S. For boundary conditions C, the anisotropic representation describes *exactly* how the simulated network responds when subjected to strain, but it has the drawback of an intuitive physical interpretation of the constants being difficult and requires as many as six constants to characterize the material.

In the cases where the network is nearly isotropic it would be advantageous to characterize the material with the two well-known parameters E and ν instead.

6.6. Approximation of nearly isotropic D-matrix

It is desired to have a method of finding the parameters that describe an isotropic material that is, in some sense, as close as possible to the simulated material, and to quantify the closeness in some way. A least squares procedure is applied to obtain an isotropic approximation of the anisotropic simulated $\boldsymbol{D}$.

A material is imagined subjected to simple tensile strain $\boldsymbol{\epsilon} = (\epsilon_0, 0, 0)$ for every direction. This results in stresses that are in general functions of material orientation

angle θ. For an isotropic material, $\boldsymbol{D}$ is however independent of θ. From (6.1) and (6.26) we have, for an exactly isotropic material

$$\begin{bmatrix} \sigma_x^e(\theta) \\ \sigma_y^e(\theta) \\ \tau_{xy}^e(\theta) \end{bmatrix} = \frac{E}{1-\nu^2} \begin{bmatrix} 1 & \nu & 0 \\ \nu & 1 & 0 \\ 0 & 0 & \frac{1-\nu}{2} \end{bmatrix} \begin{bmatrix} \epsilon_0 \\ 0 \\ 0 \end{bmatrix} = \begin{bmatrix} \frac{E}{1-\nu^2}\epsilon_0 \\ \frac{\nu E}{1-\nu^2}\epsilon_0 \\ 0 \end{bmatrix}, \tag{6.28}$$

where superscript e denotes exactly isotropic material. That is, σ_x and σ_y are constant with respect to material orientation angle θ, and τ_{xy} is identically zero for every value of θ.

For an anisotropic material all stress components vary with θ. Since it is not practically possible to simulate tension of a network in all directions, σ_x^s, σ_y^s and τ_{xy}^s are obtained by transforming $\boldsymbol{D}$ from one simulation to all material orientations. Superscript s here denotes simulated material. If the coordinate frame is rotated an angle θ, $\boldsymbol{D}$ is transformed as, see [30]

$$\boldsymbol{D}'(\theta) = \boldsymbol{T}\boldsymbol{D}\boldsymbol{T}^T, \tag{6.29}$$

where

$$\boldsymbol{T} = \begin{bmatrix} \cos^2\theta & \sin^2\theta & 2\sin\theta\cos\theta \\ \sin^2\theta & \cos^2\theta & -2\sin\theta\cos\theta \\ -\sin\theta\cos\theta & \sin\theta\cos\theta & \cos^2\theta - \sin^2\theta \end{bmatrix}. \tag{6.30}$$

This gives

$$\begin{bmatrix} \sigma_x^s(\theta) \\ \sigma_y^s(\theta) \\ \tau_{xy}^s(\theta) \end{bmatrix} = \boldsymbol{D}'(\theta) \begin{bmatrix} \epsilon_0 \\ 0 \\ 0 \end{bmatrix} = \begin{bmatrix} D'_{11}(\theta)\epsilon_0 \\ D'_{21}(\theta)\epsilon_0 \\ D'_{31}(\theta)\epsilon_0 \end{bmatrix}. \tag{6.31}$$

On denoting $\cos\theta$ by c and $\sin\theta$ by s this yields:

$$\begin{aligned} \sigma_x^s(\theta) &= (c^4 D_{11} + 2c^2 s^2 D_{12} + 4sc^3 D_{13} + s^4 D_{22} + 4s^3 c D_{23} + 4s^2 c^2 D_{33})\epsilon_0 \\ \sigma_y^s(\theta) &= (s^2 c^2 D_{11} + (s^4 + c^4) D_{12} + 2sc(s^2 - c^2) D_{13} + s^2 c^2 D_{22} + \\ &\quad 2sc(c^2 - s^2) D_{23} - 4s^2 c^2 D_{33})\epsilon_0 \\ \tau_{xy}^s(\theta) &= (-sc^3 D_{11} + sc(c^2 - s^2) D_{12} + ((c^2 - s^2)c^2 - 2s^2 c^2) D_{13} + s^3 c D_{22} + \\ &\quad ((c^2 - s^2)s^2 + 2s^2 c^2) D_{23} + 2sc(c^2 - s^2) D_{33})\epsilon_0 \end{aligned} \tag{6.32}$$

In Figure 7.23 stresses $\boldsymbol{\sigma}^s$ and $\boldsymbol{\sigma}^e$ are plotted as functions of θ. The components of $\boldsymbol{\sigma}^s$ plotted are those of the basic example network. We are looking for the value of $\boldsymbol{\sigma}^e$ that will best approximate $\boldsymbol{\sigma}^s$, and in the figure the components of $\boldsymbol{\sigma}^e$ are plotted in the position that the calculations will finally give.

We choose to minimize the square of the area between the curves for exactly isotropic and simulated material. Thus, we want to find the values of E and ν that minimize the functional Q:

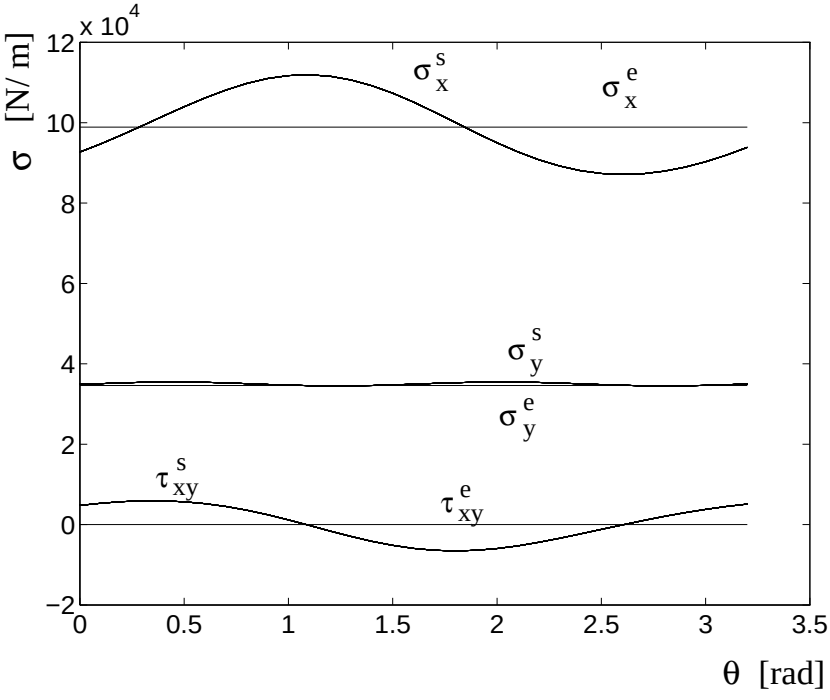

Figure 6.7: *Stresses as function of angle θ.*

$$Q = \int_0^\pi (\sigma_x^s - \sigma_x^e)^2 + (\sigma_y^s - \sigma_y^e)^2 + (\tau_{xy}^s - \tau_{xy}^e)^2 \mathrm{d}\theta \tag{6.33}$$

On inserting (6.28) we have

$$Q = \int_0^\pi (\sigma_x^s - \frac{E}{1-\nu^2}\epsilon_0)^2 + (\sigma_y^s - \frac{\nu E}{1-\nu^2}\epsilon_0)^2 + \tau_{xy}^{s^2} \mathrm{d}\theta. \tag{6.34}$$

Minimize Q with respect to $\frac{E}{1-\nu^2}$ and $\frac{\nu E}{1-\nu^2}$:

$$\begin{aligned} \frac{\partial Q}{\partial \frac{E}{1-\nu^2}} &= \int_0^\pi -2\epsilon_0(\sigma_x^s - \frac{E}{1-\nu^2}\epsilon_0)\mathrm{d}\theta = 0 \\ \frac{\partial Q}{\partial \frac{\nu E}{1-\nu^2}} &= \int_0^\pi -2\epsilon_0(\sigma_y^s - \frac{\nu E}{1-\nu^2}\epsilon_0)\mathrm{d}\theta = 0 \end{aligned} \tag{6.35}$$

Integrating the last term and rearranging the equations give

$$\begin{aligned} \int_0^\pi \sigma_x^s \mathrm{d}\theta &= \frac{E}{1-\nu^2}\epsilon_0 \pi \\ \int_0^\pi \sigma_y^s \mathrm{d}\theta &= \frac{E\nu}{1-\nu^2}\epsilon_0 \pi. \end{aligned} \tag{6.36}$$

These equations imply that the areas under the curves for exactly isotropic and simulated material should be the same. Now it remains to evaluate the area under the stress curves for a simulated material.

Integrating (6.32) gives

$$\begin{aligned} \int_0^\pi \sigma_x^s \mathrm{d}\theta &= \frac{\pi}{8}(3D_{11} + 2D_{12} + 3D_{22} + 4D_{33}) \\ \int_0^\pi \sigma_y^s \mathrm{d}\theta &= \frac{\pi}{8}(D_{11} + 6D_{12} + D_{22} - 4D_{33}) \\ \int_0^\pi \tau_{xy}^s \mathrm{d}\theta &= 0. \end{aligned} \tag{6.37}$$

From (6.36) and (6.37) we can now calculate the values of ν and E that minimize Q:

$$\nu = \frac{\int_0^\pi \sigma_y^s \mathrm{d}\theta}{\int_0^\pi \sigma_x^s \mathrm{d}\theta} = \frac{(D_{11} + 6D_{12} + D_{22} - 4D_{33})}{(3D_{11} + 2D_{12} + 3D_{22} + 4D_{33})}$$

$$E = \frac{1-\nu^2}{\epsilon_0 \pi} \int_0^\pi \sigma_x^s \mathrm{d}\theta = \frac{1-\nu^2}{8\epsilon_0}(3D_{11} + 2D_{12} + 3D_{22} + 4D_{33})$$

An invariant, with respect to rotation of coordinate frame, of the D-matrix is taken as a measure of the error caused by classifying the material as isotropic. The fourth rank constitutive tensor has the following four independent invariants, see [11], given in terms of the elements of the D-matrix.

$$\begin{aligned} I_D &= D_{11} + D_{22} + 2D_{33} \\ II_D &= D_{11}D_{22} + 2D_{33}(D_{11} + D_{22}) - D_{12}^2 - 2D_{13}^2 - 2D_{23}^2 \\ III_D &= (-D_{11} + D_{22})^2 + 4(D_{13} + 4D_{23})^2 \\ IV_D &= D_{11} + D_{22} + 2D_{12} \end{aligned} \tag{6.38}$$

For an isotropic material this reduces to

$$\begin{aligned} I_D &= \frac{E}{1-\nu^2}(3-\nu) \\ II_D &= \frac{E^2}{(1-\nu^2)^2}(3-2\nu-\nu^2) \\ III_D &= 0 \\ IV_D &= \frac{E}{1-\nu^2}(2+2\nu). \end{aligned} \tag{6.39}$$

III_D is equal to zero for an isotropic material, but not for the simulated anisotropic material. III_D is chosen as a measure of the error caused by classifying the material as isotropic, and to achieve a scale-indifferent measure it is normalized by dividing with the square of the estimated Young's modulus:

$$err = \frac{(-D_{11}+D_{22})^2 + 4(D_{13}+4D_{23})^2}{E^2} \tag{6.40}$$

Equations (6.38) and (6.39) provide an alternative possibility to estimate E and ν. For the isotropic material there are three non-trivial equations and two unknowns, E and ν. This implies that there is a dependence between the equations and therefore the two linear equations can be used to solve for E and ν. Thus, if I_D and IV_D are calculated from (6.38) for the simulated $\boldsymbol{D}$, E and ν can be solved for in (6.39). After some calculations it is concluded that this procedure gives exactly the same E and ν as the least-squares approach.

6.7. Approximation of near orthotropic D-matrix

If the orientation distribution of the fibres is not uniform, but still symmetric with respect to two perpendicular axes, there is no longer any reason to believe that the material is transversely isotropic, but rather orthotropic. Thus, we want to know what is the best estimation of orthotropic material parameters.

One problem that arises is that of finding the principal directions of the simulated material. The simplest solution would be to assume that the principal directions are coincident with the symmetry axes of the orientation distribution, which they should be on taking the average of many networks. A second way would be to transform the $\boldsymbol{D}$ obtained from simulations to different material orientations and check where a principal direction criterion is best fulfilled. This criterion could be maximum value of D_{11} or D_{22} and close to zero value of D_{31} and D_{32}. We choose to use the first approach since this seems to be a reasonable approximation in the cases where it is used, see Section 7.5.

Thus we assume that the principal directions are known to coincide with the coordinate axes. We use the same approach as for isotropic material, that is minimize

$$Q = \int_0^\pi [(\sigma_x^s - \sigma_x^e)^2 + (\sigma_y^s - \sigma_y^e)^2 + (\tau_{xy}^s - \tau_{xy}^e)^2]\mathrm{d}\theta \tag{6.41}$$

with respect to the four independent components of the orthotropic $\boldsymbol{D}$, see (6.25).

$\boldsymbol{\sigma}^s$ is the same as in the preceding section, that is

$$\begin{aligned}
\int_0^\pi \sigma_x^s \mathrm{d}\theta &= \frac{\pi}{8}(3D_{11}^s + 2D_{12}^s + 3D_{22}^s + 4D_{33}^s) \\
\int_0^\pi \sigma_y^s \mathrm{d}\theta &= \frac{\pi}{8}(D_{11}^s + 6D_{12}^s + D_{22}^s - 4D_{33}^s) \\
\int_0^\pi \tau_{xy}^s \mathrm{d}\theta &= 0,
\end{aligned} \tag{6.42}$$

where superscript s has been added to emphasize that we refer to the components of $\boldsymbol{D}$ obtained from simulations. $\boldsymbol{\sigma}^e$ is not as simple as in the isotropic case, superscript e here denoting exactly orthotropic material, since it is dependent on material orientation angle θ. That is

$$\begin{bmatrix} \sigma_x^e(\theta) \\ \sigma_y^e(\theta) \\ \tau_{xy}^e(\theta) \end{bmatrix} = \boldsymbol{D}^{e'}(\theta) \begin{bmatrix} \epsilon_0 \\ 0 \\ 0 \end{bmatrix} = \begin{bmatrix} D_{11}^{e'}(\theta)\epsilon_0 \\ D_{21}^{e'}(\theta)\epsilon_0 \\ D_{31}^{e'}(\theta)\epsilon_0 \end{bmatrix}. \tag{6.43}$$

In analogy with $\boldsymbol{\sigma}^s$, this yields

$$\begin{aligned}
\int_0^\pi \sigma_x^e \mathrm{d}\theta &= \frac{\pi}{8}(3D_{11}^e + 2D_{12}^e + 3D_{22}^e + 4D_{33}^e) \\
\int_0^\pi \sigma_y^e \mathrm{d}\theta &= \frac{\pi}{8}(D_{11}^e + 6D_{12}^e + D_{22}^e - 4D_{33}^e) \\
\int_0^\pi \tau_{xy}^e \mathrm{d}\theta &= 0.
\end{aligned} \tag{6.44}$$

On inserting the expressions for $\boldsymbol{\sigma}^e$ and $\boldsymbol{\sigma}^s$ in (6.41), it appears that the best estimation is to take the coefficients directly from the simulated $\boldsymbol{D}$, that is

$$\begin{aligned}
D_{11}^e &= D_{11}^s \\
D_{12}^e &= D_{12}^s \\
D_{22}^e &= D_{22}^s \\
D_{33}^e &= D_{33}^s.
\end{aligned} \tag{6.45}$$

The components D_{31}^s and D_{32}^s provide a measure of the correctness of the approximation to orthotropic material, since they should be identically zero in a truly orthotropic material. We could for example take

$$err = \frac{4(D_{13}^s + 4D_{23}^s)^2}{E^2} \tag{6.46}$$

as an error measure, although this quantity is not invariant under rotation of coordinate frame, as is that of (6.40).

The step from components of $\boldsymbol{D}^e$ to the individual physical constants $E_x, E_y, G_{xy}, \nu_{xy}$ and ν_{yx} consists of solving the non-linear system of equations

$$\begin{cases} \dfrac{E_x}{1-\nu_{xy}\nu_{yx}} = D^e_{11} \\ \dfrac{E_y}{1-\nu_{xy}\nu_{yx}} = D^e_{22} \\ \dfrac{E_x\nu_{yx}}{1-\nu_{xy}\nu_{yx}} = D^e_{12} \\ \dfrac{E_y\nu_{xy}}{1-\nu_{xy}\nu_{yx}} = D^e_{12} \\ G_{xy} = D^e_{33} \end{cases} . \tag{6.47}$$

The solution to this is

$$\begin{cases} E_x = D^e_{11}(1 - \dfrac{(D^e_{12})^2}{D^e_{11}D^e_{22}}) \\ E_y = D^e_{22}(1 - \dfrac{(D^e_{12})^2}{D^e_{11}D^e_{22}}) \\ \nu_{yx} = \dfrac{D^e_{12}}{D^e_{11}} \\ \nu_{xy} = \dfrac{D^e_{12}}{D^e_{22}} \\ G_{xy} = D^e_{33} \end{cases} , \tag{6.48}$$

providing the parameters used for describing an orthotropic network in the next chapter.

7. Results from analysis of initial global stiffness properties

The initial global stiffness properties are given in terms of the parameters defined in the preceding chapter, in the case of an isotropic network Young's modulus E and Poisson's ratio ν. Those values are obtained from the results of three simulations, pure tension in the x- and y-directions respectively and pure shear, which are combined by means of a least squares procedure. In Section 7.1, however, stiffness is given in terms of the reaction force in the x-direction when the sample is subjected to strain in the x-direction. It is thus based on the result of only one simulation. In this section change in stiffness due to change in sample size rather than the absolute value of the stiffness is the primary concern. Because of this the simpler method of evaluating stiffness is considered to be sufficient. In addition, normalized quantities are used in Section 7.1. Young's modulus, which is here $F_x/L\epsilon_x$, is divided by $E_f l_f$ to obtain a normalized stiffness measure.

7.1. Effect of sample size and boundary conditions

An interesting issue is what size as compared with fibre length a network unit must have. Since computer resources are limited, it is important to know how small a square can be analyzed without the relevance of the results being lost.

Numerical simulations were carried out to examine the dependence of stiffness on sample size and boundary conditions. The networks that were simulated had material properties like those specified for the basic example network, Section 5.1. In Figures 7.1-7.3 and 7.6, the relationship between normalized stiffness

$$\frac{F_x}{E_f L l_f \epsilon_x}$$

and ratio L/l_f is plotted. In the normalized stiffness, F_x is the resultant force in the x-direction when the quadratic network of side L is subjected to strain $\boldsymbol{\epsilon}=(\epsilon_x,0,0)$.

Figures 7.1 and 7.2 show the results from simulation of networks in which $\rho l_f = 40$. For every L/l_f considered, ten different geometries were simulated, each geometry being subjected to the two sets of boundary conditions discussed in Section 6.2: S in Figure 7.1 and C in Figure 7.2 .

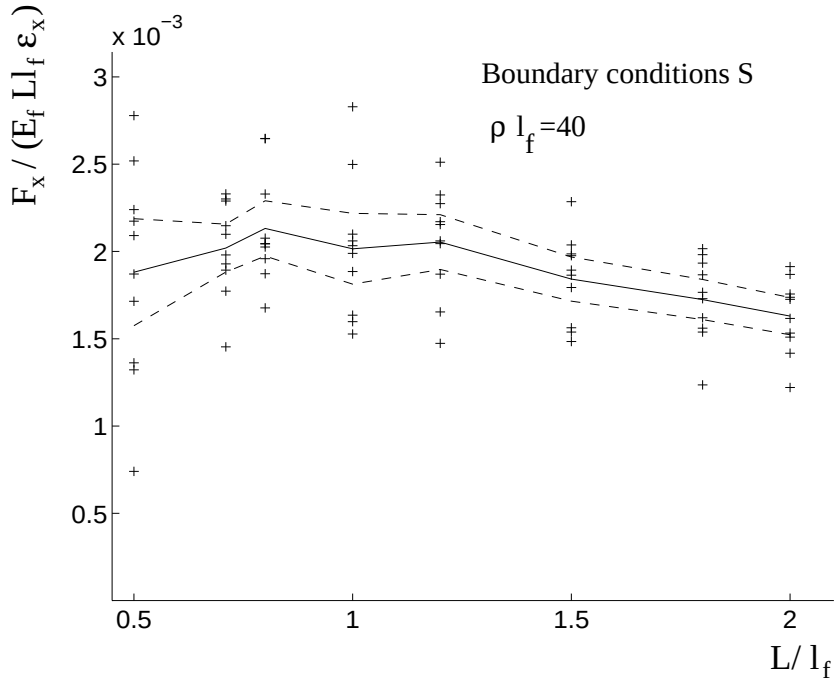

Figure 7.1: *Normalized stiffness against L/l_f: Boundary conditions S.*

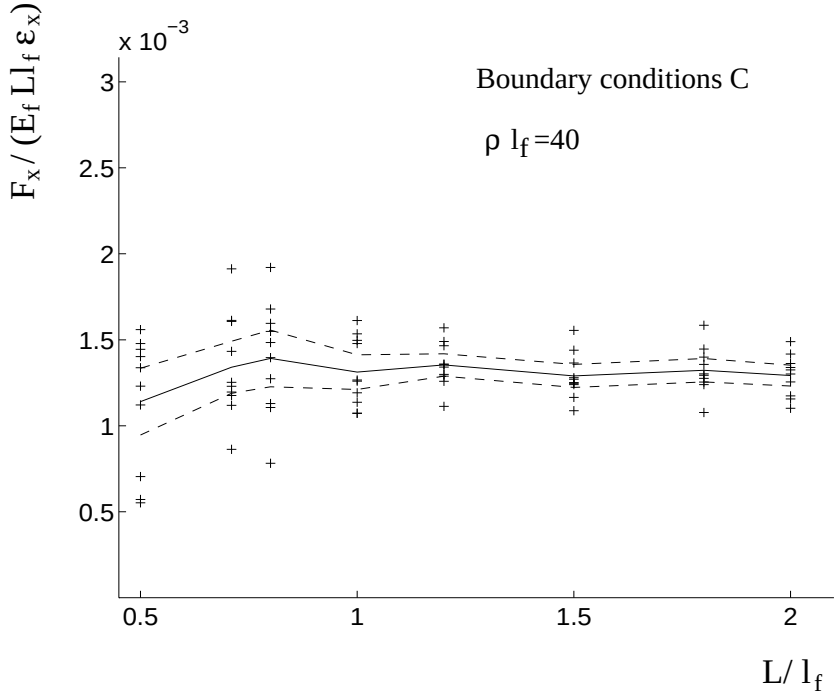

Figure 7.2: *Normalized stiffness against L/l_f: Boundary conditions C.*

By using normalized quantities the stiffness can be extracted for all networks having the same normalized density ρl_f and ratio L/l_f, provided that the ratios

$$\frac{b_f}{l_f}, \quad \frac{b_f}{h_f}, \quad \frac{E_f b_f h_f}{l_f}/k_x \quad \text{and} \quad \frac{E_f b_f h_f^3}{l_f}/k_\varphi$$

are also the same.

It can be seen from the diagrams that the scatter of the points is considerable for low values of L/l_f, and that it gradually decreases as L/l_f increases. It is also noted that the scatter is larger for boundary conditions S. The solid line is the average from the ten simulations, and the dashed lines denote standard deviation. For boundary conditions S the average stiffness varies up and down to begin with, but from $L/l_f = 1.2$ it is steadily decreasing. Boundary conditions C, on the other hand, show a rather constant stiffness from $L/l_f = 1.0$ and forward. This indicates that the stiffness is sample size-dependent for boundary conditions S at these values of L/l_f and ρl_f, while boundary conditions C seem to give an almost constant value of the stiffness already from $L/l_f = 1.0$.

Figure 7.3 shows normalized stiffness, average from ten calculations, against L/l_f for three different densities, $\rho l_f = 30$, 40 and 50. Both boundary conditions are shown for each density. The tendency from $\rho l_f = 40$ is also found for the other densities.

That is, when using the set of boundary conditions S, one must analyse a much larger network in order to obtain a correct stiffness value than is the case for boundary conditions C. It is concluded that for boundary conditions C, $L/l_f \geq 1$ is a minimum requirement for obtaining relevant stiffness values.

For the conventional boundary conditions S, the corresponding minimum requirement can be estimated as being approximately $L/l_f \geq 3$.

A larger L/l_f ratio means more degrees of freedom and requires much more computer time and memory. Thus it is concluded that use of boundary conditions C is by far the more economic alternative. The gain is not quite as large, however, as one might at first anticipate. This is because conditions C involve the use of constraints, which makes the solution of the system of equations more time-consuming and requires more memory. If nothing else is said, boundary conditions C are used in all the simulations cited in the following.

The results from Figure 7.3 are repeated in another form in Figure 7.4. In Figure 7.4 normalized stiffness for boundary conditions S relative to normalized stiffness for boundary conditions C is plotted against L/l_f. The relative difference between the two boundary conditions decreases as ρl_f increases, but for $\rho l_f = 50$ and $L/l_f = 2$ there is still close to 25% overestimation of the stiffness when using boundary conditions C.

The results above suggest that the initial stiffness is approximately independent of sample size for squares of $L/l_f \geq 1.2$, for boundary conditions C, at the investigated levels of network densities. This conclusion may, however, not be general for all network densities. This is due to the effects of statistical distribution of stiffness properties in different areas of a heterogeneous material. The case of

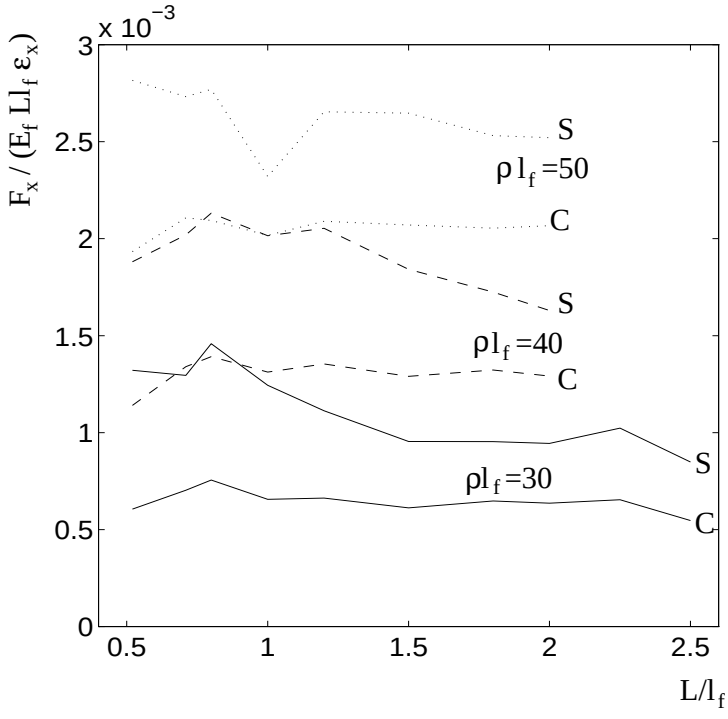

Figure 7.3: *Normalized stiffness against L/l_f.*

a growing square lies somewhere between the extreme cases of coupling more and more material cells in series or in parallel. In a parallel coupling the total stiffness is not affected by scatter in properties of the components, while a structure coupled in series is weakened by scatter. This effect is illustrated by a simple example of springs coupled in series and parallel in Figure 7.5. The average spring stiffness is the same in all four cases. As a growing square could be viewed as a combination of serial and parallel coupling, the weakening effect of scatter on global stiffness may be of significance if the scatter is large enough. As the scatter in stiffness results increases for decreasing network density this would be an issue in particular for low network densities. In Figure 7.6 results are shown from simulations of $\rho l_f = 15$ and 20, boundary conditions C. The solid lines denote averages of ten calculations and the dotted lines denote standard deviation. There is a weak tendency of increasing slope of the curves as ρl_f decreases, but the large standard deviation makes definite conclusions difficult. This issue is further discussed in Section 9.1.

In the simulations cited here, all fibres are of the same length. For the case of a statistical distribution of fibre length, the requirement $L/l_f \geq 1.2$ must be modified according to the distribution.

The standard deviation decreases moderately with increasing L/l_f, which means that the number of simulations can be decreased for larger L/l_f. Since the computational time increases dramatically, however, as L/l_f increases, it is from the

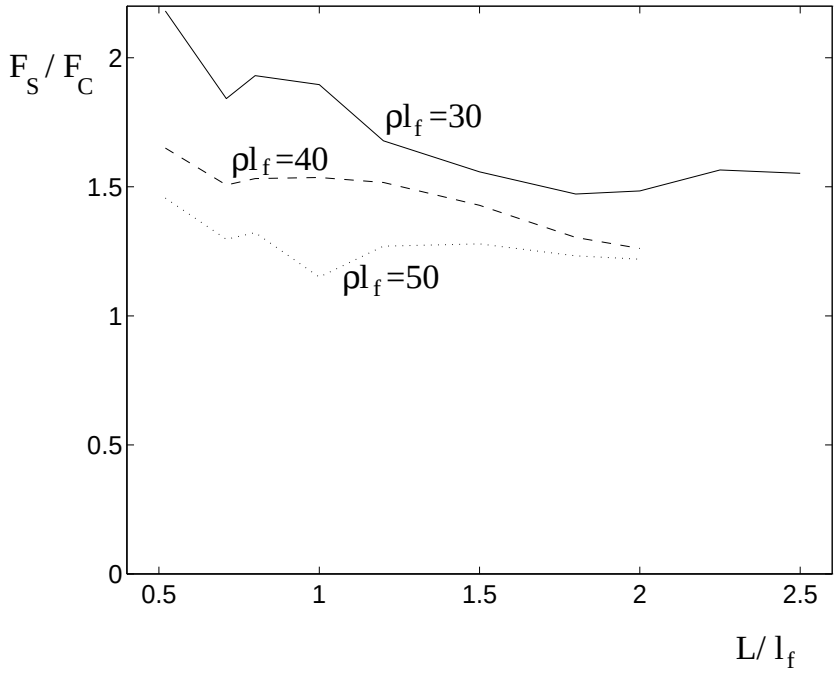

Figure 7.4: *Normalized stiffness of b.c. S relative to b.c. C against L/l_f.*

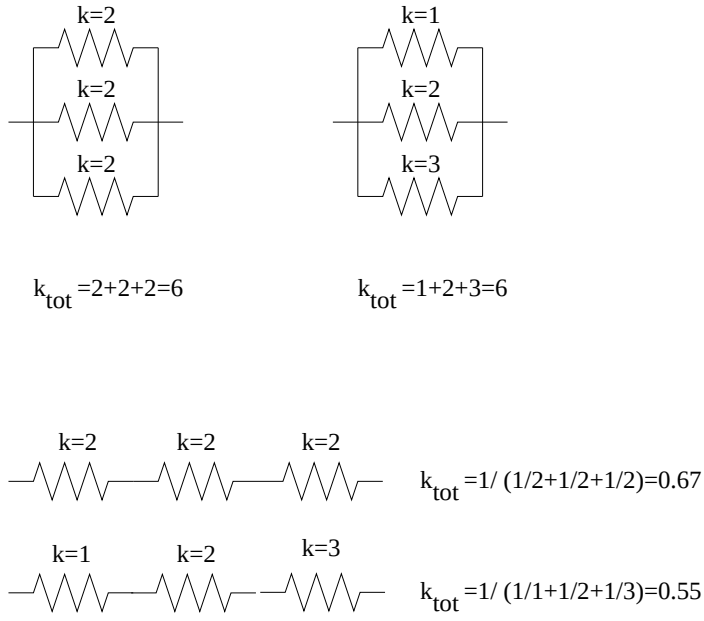

Figure 7.5: *Example showing effect of scatter in stiffness properties for spring couplings.*

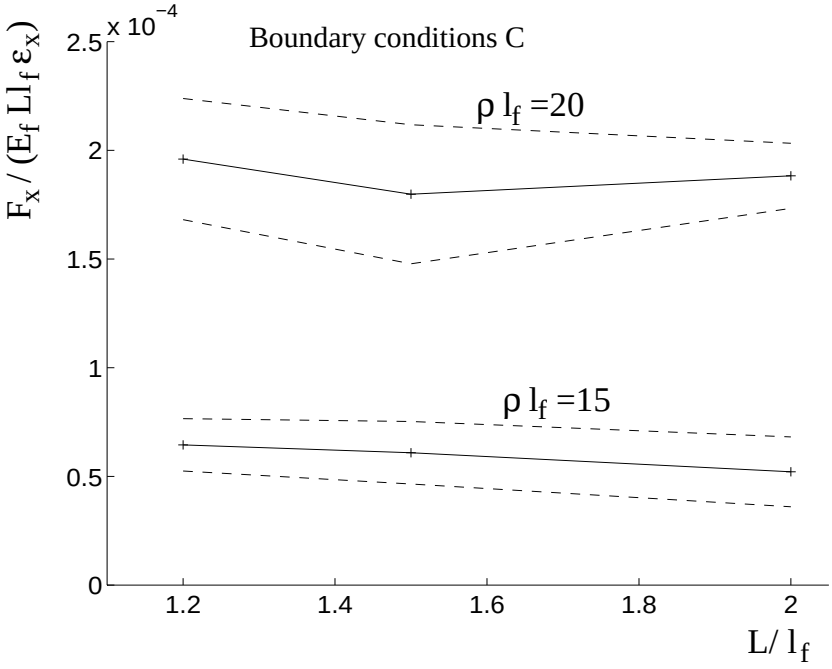

Figure 7.6: *Normalized stiffness against L/l_f: Boundary conditions C.*

computational point of view best to select a minimal value of L/l_f.

7.2. Global elastic stiffness vs stiffness of components

The global elastic stiffness of a network depends on the stiffness properties of the components, and on how these are geometrically arranged. To examine the dependence on the components' stiffness, simulations were made on the basic example network geometry. Each stiffness parameter was varied, one at a time, over a wide range. The parameters considered were stiffness of connections, $k_x = k_y$ and k_ϕ, and moment of inertia, I_f, cross-sectional area, A_f, and Young's modulus, E_f, of fibres. Each point in the diagrams is an average from three calculations, and the relative standard deviation for E is $< 1\%$, except for the I_f-curve in Figure 7.8 where it is $1 - 5\%$. For ν the relative standard deviation is $1 - 5\%$ except for a few values in the lower ranges of I_f, Figure 7.8, where it rises to at most 11%.

In Figure 7.7 the influence of the stiffness of the connections is plotted. The variable on the x-axis is $\log(k_x/k_x^0)$, where k_x^0 denotes k_x for the basic example network. Analogous notation is used in Figures 7.8 and 7.9. Since it turns out that the rotational stiffness has very little influence on E, two curves for the variation of k_x and k_y are plotted, one with an extremely high and one with an extremely low value of k_ϕ. When $k_x = k_y$ approaches zero, global stiffness obviously also approaches zero. When the value of $k_x = k_y$ increases, a plateau is reached when the

connections are approximately rigid. One can compare this plateau value with the value predicted by a homogeneous field approximation. As discussed in Section 2.1, Cox, in [6], shows that in an isotropic fibre network experiencing a homogeneous strain field, that is where every fibre is strained exactly to the extent of the global strain in the network,

$$\begin{aligned} E &= K/3 \\ G &= K/8 \\ \nu &= 1/3, \end{aligned} \tag{7.1}$$

$$\text{where } K = A_f E_f \rho. \tag{7.2}$$

For the basic example network (7.1) gives $E = 17.5 \cdot 10^4$ N/m and the plateau value from the simulations is $E = 13.2 \cdot 10^4$ N/m. Accordingly the homogeneous field assumption predicts a significantly stiffer network even when assuming the connections to be rigid. This is probably due to bending of the fibres, as discussed in Section 2.1.

Poisson's ratio, in contrast to Young's modulus, is affected by k_ϕ, as can be seen in Figure 7.7. For a weak ϕ-spring ν is approximately constant, whereas ν is strongly dependent on k_x and k_y in the case of stiffer ϕ-springs. For the stiffer x- and y-springs ν is close to the value of 1/3 predicted by (7.1) for a network experiencing homogeneous strain.

E and ν as a function of $\log(I_f/I_f^0)$, $\log(A_f/A_f^0)$ and $\log(E_f/E_f^0)$ are shown in Figure 7.8. It is seen that A_f is the most important variable and that I_f has not so much influence on E, when varying the parameters around the values of the basic example network. To change the ratio A_f/I_f means primarily to distort the cross section, and this is not very realistic over the wide ranges shown here. However, second order effects resulting from fibres not being straight can be approximately taken into account by modifying A_f. In Figure 7.8 it is also seen that ν shows moderate variations, except for very small values of A_f. Here ν suddenly drops, and even reaches negative values. Negative values of ν are also found experimentally in paper, see [23], which can be regarded as a dense cellulose fibre network.

G, obtained from the above results as $E/(2(1+\nu))$, shows a similar dependence on k_x and k_y as E, as is seen in Figure 7.9. One would expect G to depend more on k_ϕ, since ν does so, but the variation of ν only starts at such low values of k_x and k_y that E is already close to zero.

From Figure 7.9 it is seen that also when fibre properties are varied, G shows a variation similar to that of E.

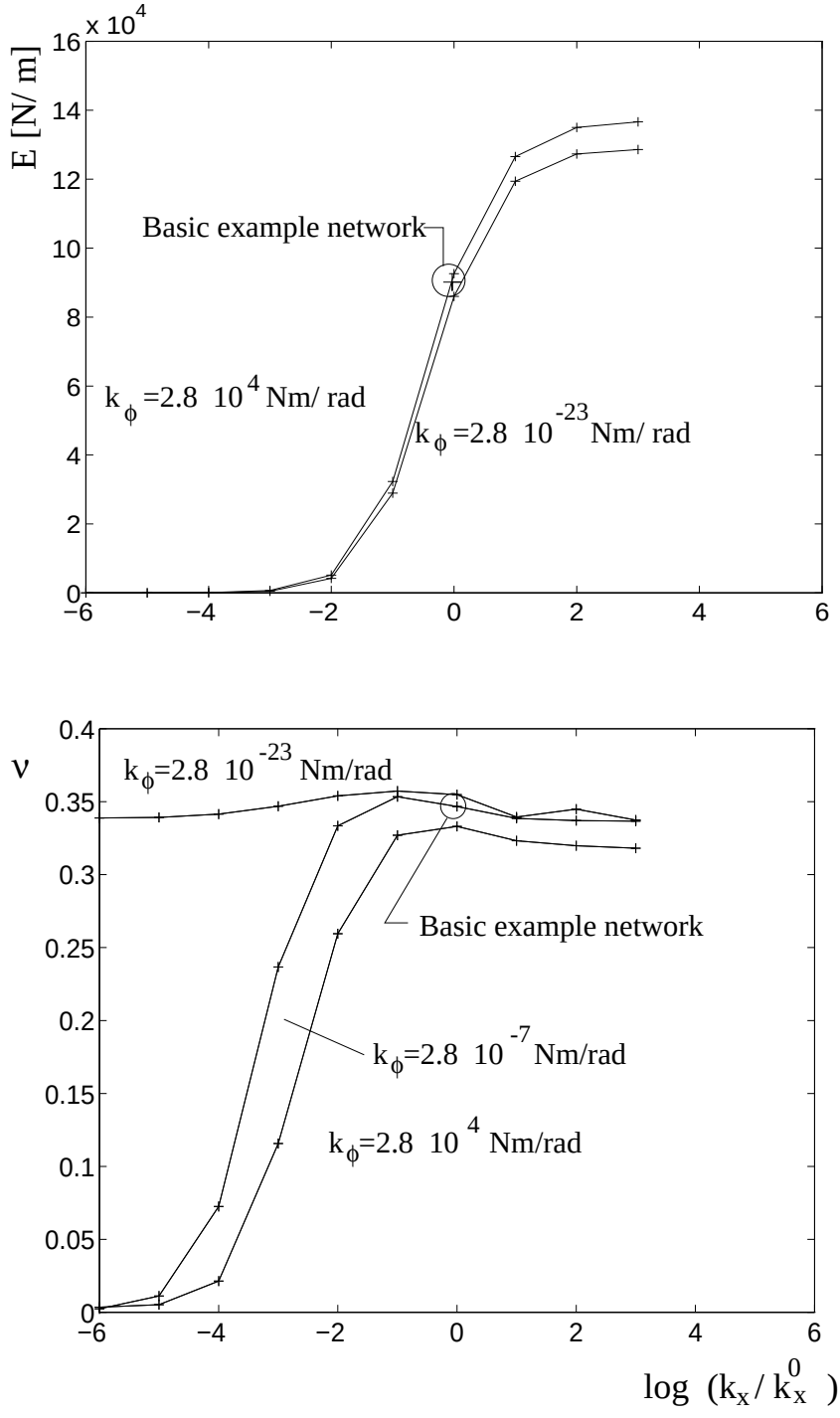

Figure 7.7: *E and ν against $log(k_x/k_x^0)$.*

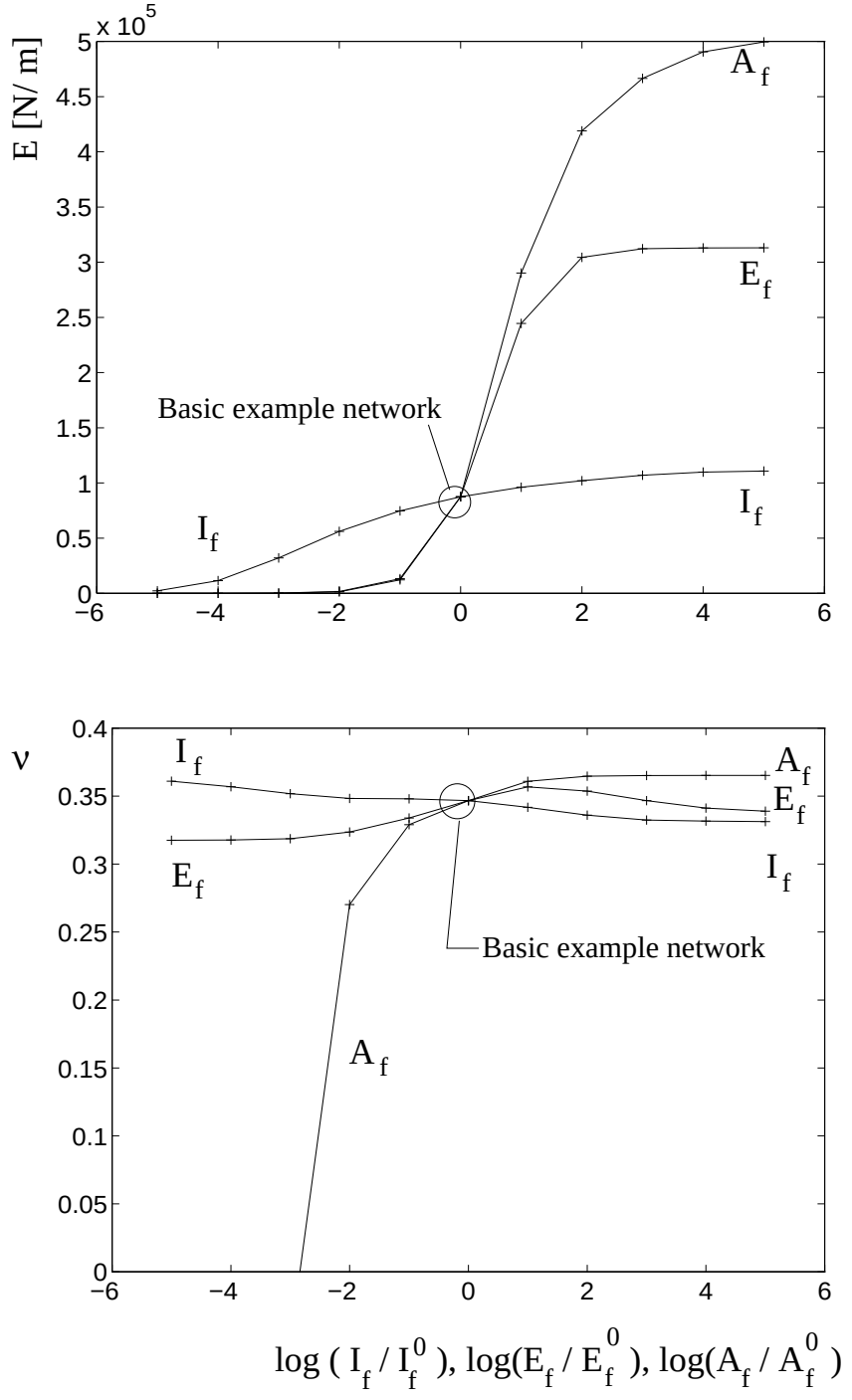

Figure 7.8: *E and ν against $log(I_f/I_f^0)$, $log(E_f/E_f^0)$, $log(A_f/A_f^0)$.*

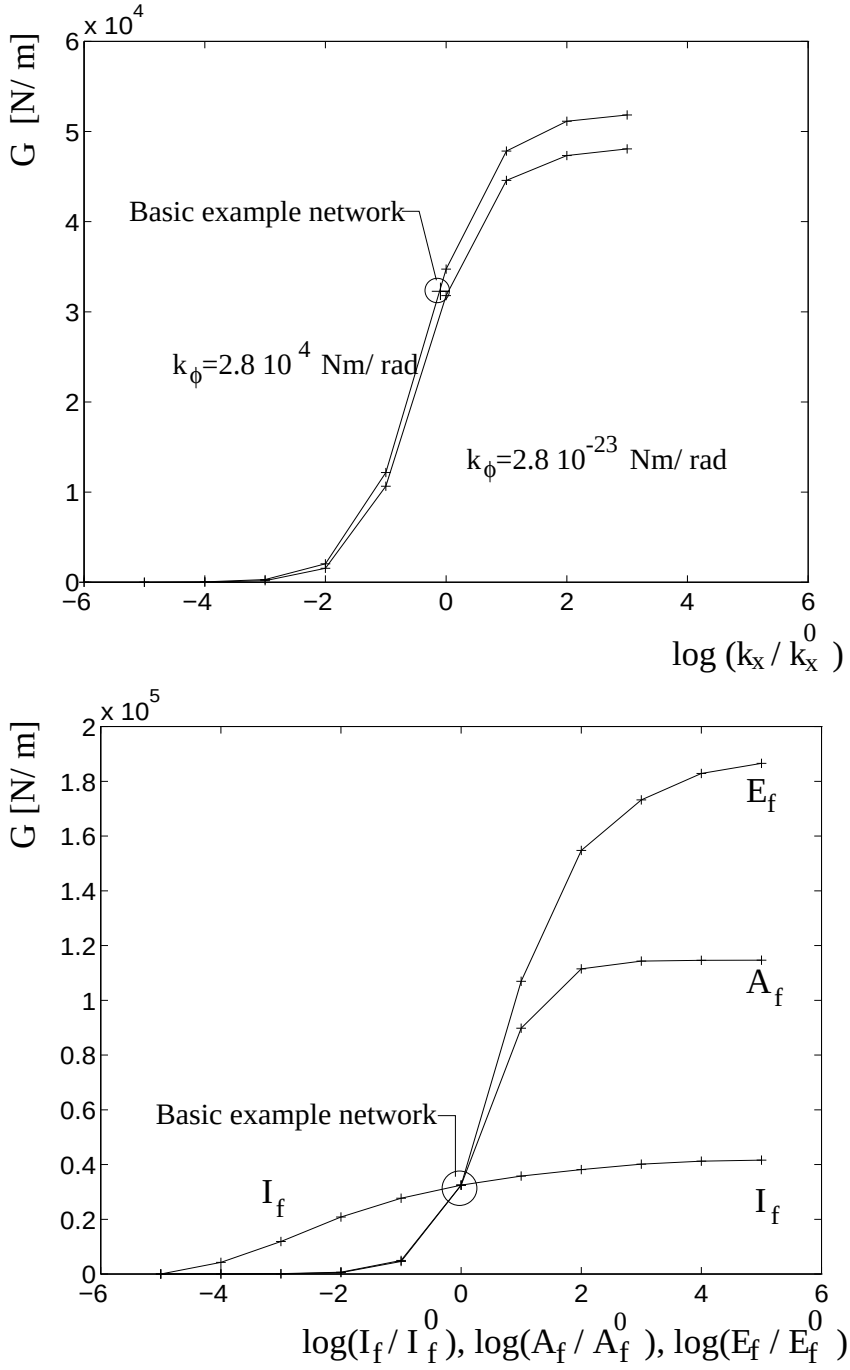

Figure 7.9: *G against* $log(k_x/k_x^0)$ *and* $log(I_f/I_f^0)$, $log(E_f/E_f^0)$, $log(A_f/A_f^0)$.

7.3. Global elastic stiffness vs network density and degree of fibre-to-fibre interaction

The network density is found to have a strong influence on the elastic stiffness of the network structure. Simulations were made for six different densities. In Figure 7.10 and 7.11 E and ν are plotted against network density ρ. The five curves represent different probabilities for interaction at a fibre crossing, s=1.0, s=0.8, s=0.6, s=0.4 and s=0.2. For densities ρ=30-60 mm^{-1} ten simulations were made for each value of ρ, but for ρ=70 and 80 mm^{-1} it was sufficient to make seven and three simulations respectively to reach the same level of standard deviation. Vertical lines indicate standard deviation for E in Figure 7.10. The lower densities are omitted for s=0.4 and s=0.2, since the simulation results show too much scatter to be relevant. The lines in Figure 7.10 are almost parallel, indicating s to be of greater importance for lower values of ρ. This is further emphasized in Figure 7.12, in which $E/E_{s=1.0}$ is plotted against ρ. Here $E_{s=1.0}$ denotes E for the case when $s = 1$.

The value of Poisson's ratio ν is rather stable at around 0.34; it is only due to the scale of the diagram that one can detect any differences, irrespective of changes in ρ and s, except for $s = 0.2$ which yields a somewhat higher value of ν.

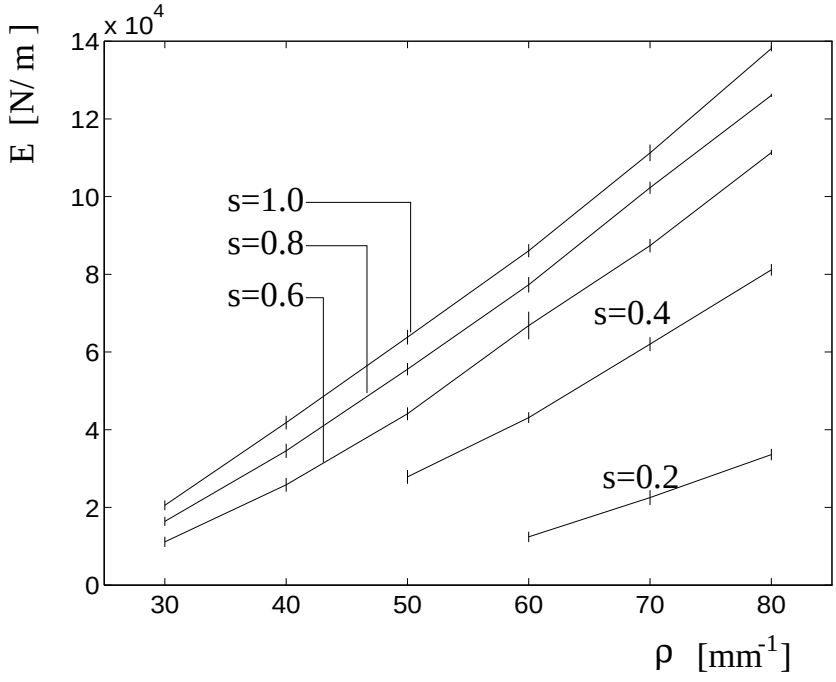

Figure 7.10: *E against ρ and s.*

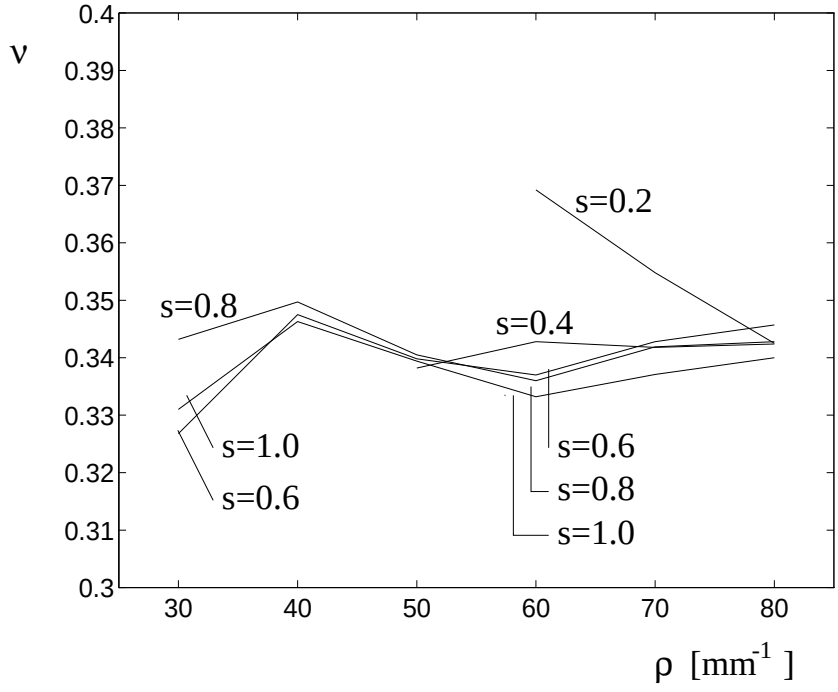

Figure 7.11: *ν against ρ and s.*

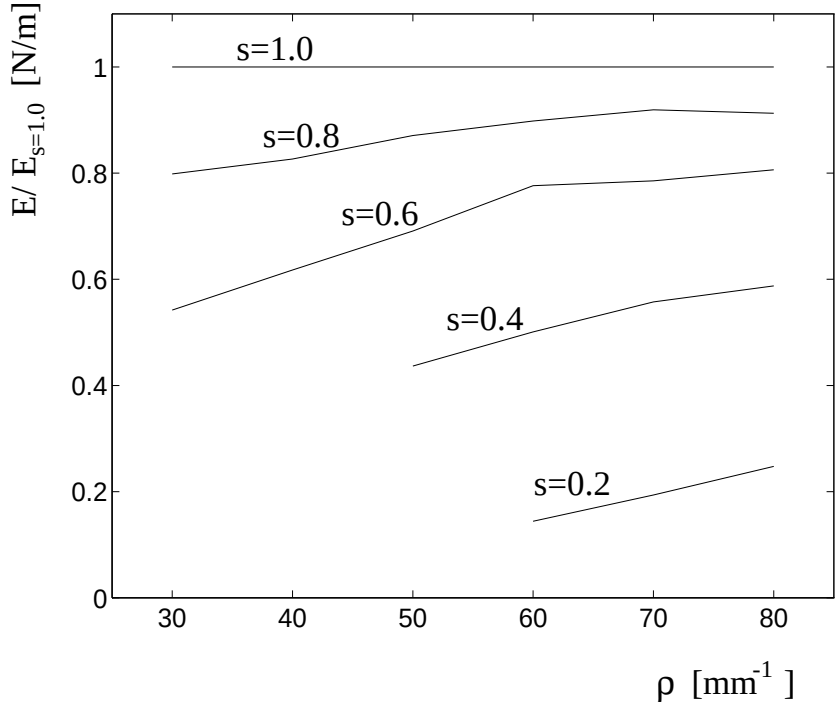

Figure 7.12: *$E/E_{s=1.0}$ against ρ and s.*

7.4. Global elastic stiffness vs fibre curl

Fibre curl is found to have a strong influence on the global elastic stiffness of a network. This is because curled fibres have lower values of axial stiffness, and also because the geometry structure of the network becomes different. The load-bearing lines no longer extend as straight lines, but take a curved path.

Simulations have been made, for two different network densities, to evaluate the dependence of E and ν on the degree of curl of the fibres. The curl indices considered were 0.7, which is close to a semi-circle, 0.8, 0.9 and 1.0, which is a straight fibre. The results are shown in Figures 7.13 and 7.14. Each point is the average from two or three simulations; standard deviations are indicated by vertical lines. It can be seen that E increases with increasing curl index for both $\rho = 40$ mm^{-1} and $\rho = 60$mm^{-1}, but c has as expected more influence on the less dense network. Here the ratio between E for straight fibres and E for $c = 0.7$ is equal to 3.6, while the same ratio for $\rho = 60$ mm^{-1} is only 1.9. ν does not differ much between the two densities, but has a clear tendency to increase as the fibres become more curled, as can be seen in Figure 7.14. It does even increase above 0.5, a fact that is commented in Section 6.5.

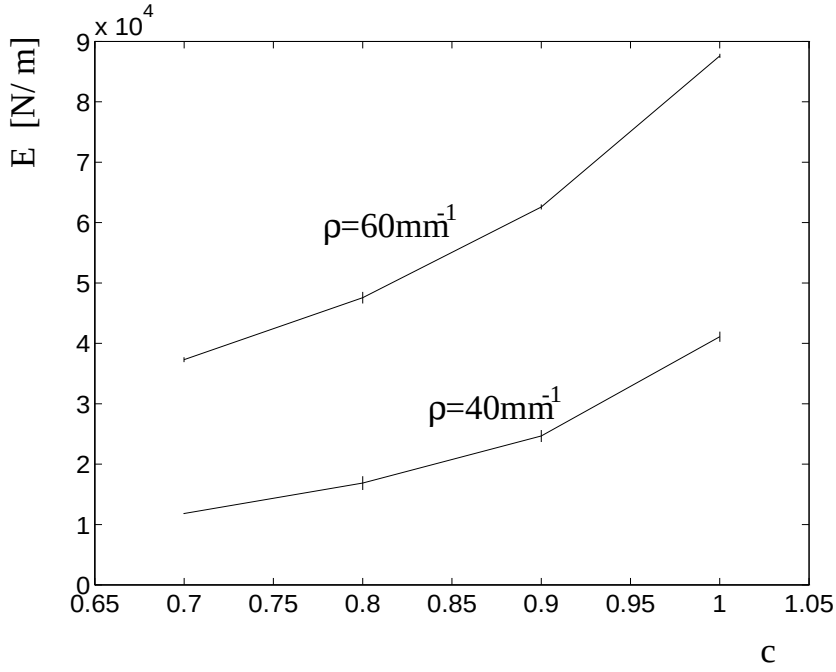

Figure 7.13: *E against curl index, c.*

The effect of fibre curl can be imagined to consist of two interactive separate effects. One is that the whole fibre does not extend straight across the network, but describes a curved path. The other is that the fibre segment between two

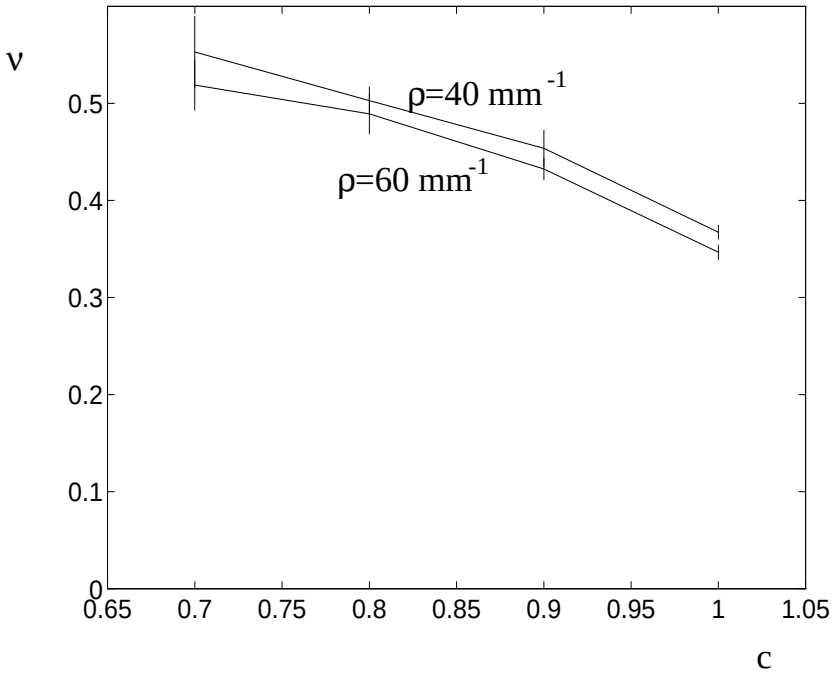

Figure 7.14: ν *against curl index, c.*

neighboring connections is curved, and thus is weaker in the axial direction. The relative importance of those two effects has been investigated. In addition to the simulations with curled fibres mentioned earlier, simulations have been made in which the beam elements have been substituted by straight ones in the curled global geometry. A network of straight fibres has also been generated, with the same nominal properties as the curled one, but the beam elements have been substituted by curly ones with the curl indices that were considered before. A symbolical sketch of the networks and notations used is given in Figure 7.15.

Figure 7.16 shows E against curl index for the different types of networks. E for a network of curled fibres, Figure 7.13, is repeated here by solid lines. The dotted lines marked CS and SC represent networks according to Figure 7.15, and on top a dash-dotted line indicates the value of E for a network of straight fibres. It is concluded that the effect of the fibres not extending straight across the network is more important than that of the axial stiffness being lower. Moreover, in the cases shown in the diagram the two effects seem to be fairly additive.

Figure 7.17 shows the corresponding curves for ν. It can be seen that a network of type SC gives a value of ν that is practically identical to that of a network of straight fibres. Somewhat surprisingly, a network of type CS gives even higher values of ν than the network made of curled fibres. Obviously, ν is not very dependent on the axial stiffness of the fibres, which is also consistent with the results of Figure 7.8, in the range close to the basic example network. A geometry structure made up of

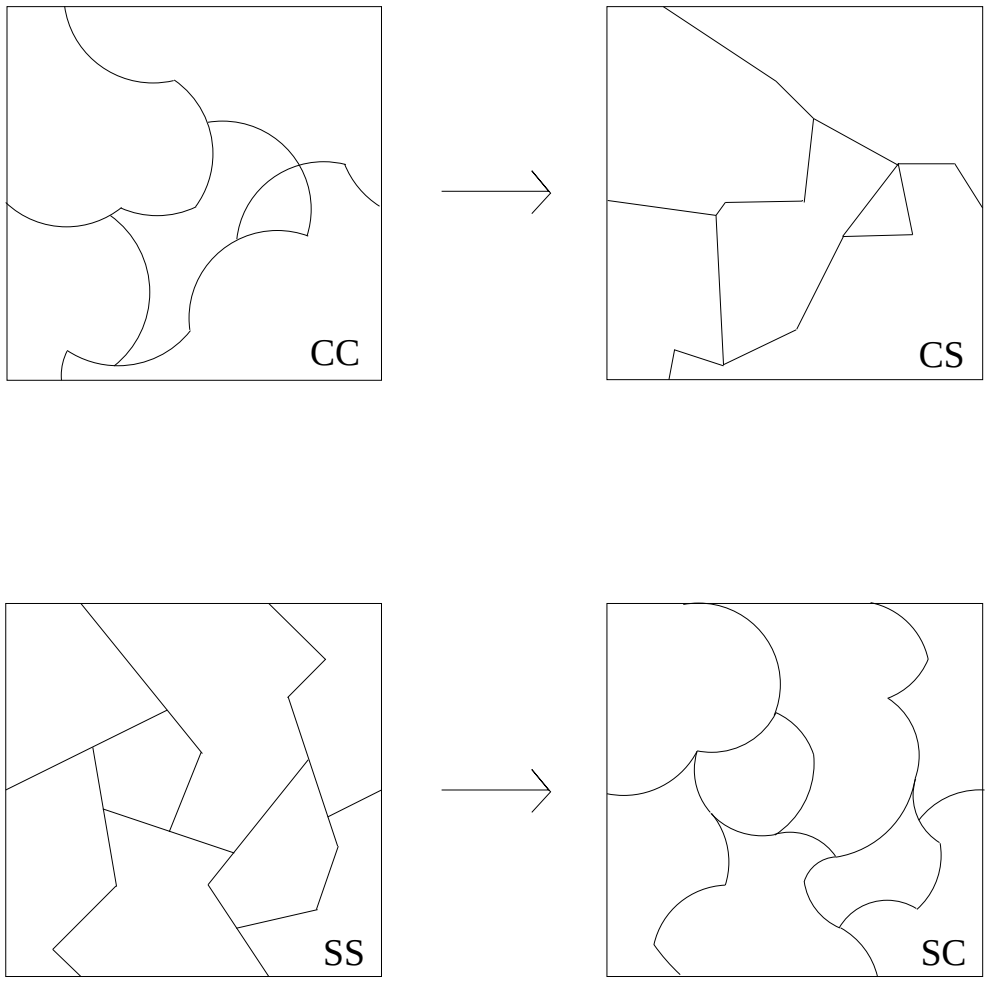

Figure 7.15: *Different combinations of straight and curled properties.*

curled fibres, on the other hand, has a rather strong increasing effect on ν.

As mentioned earlier, an approximate method of accounting for curled fibres might be to reduce the axial stiffness of the beam elements. The results presented here indicate, however, that this approach would not give satisfactory results.

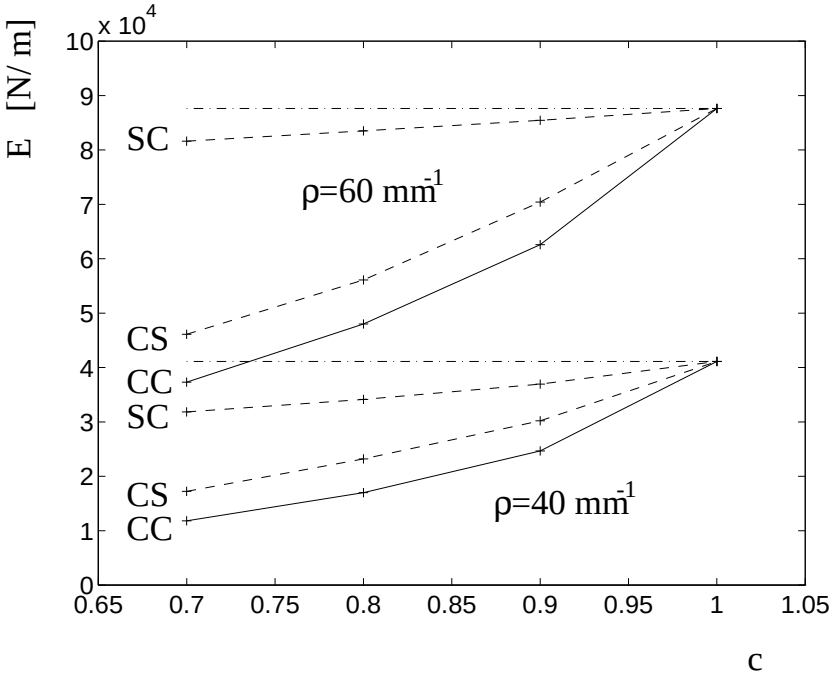

Figure 7.16: *E against curl index, c.*

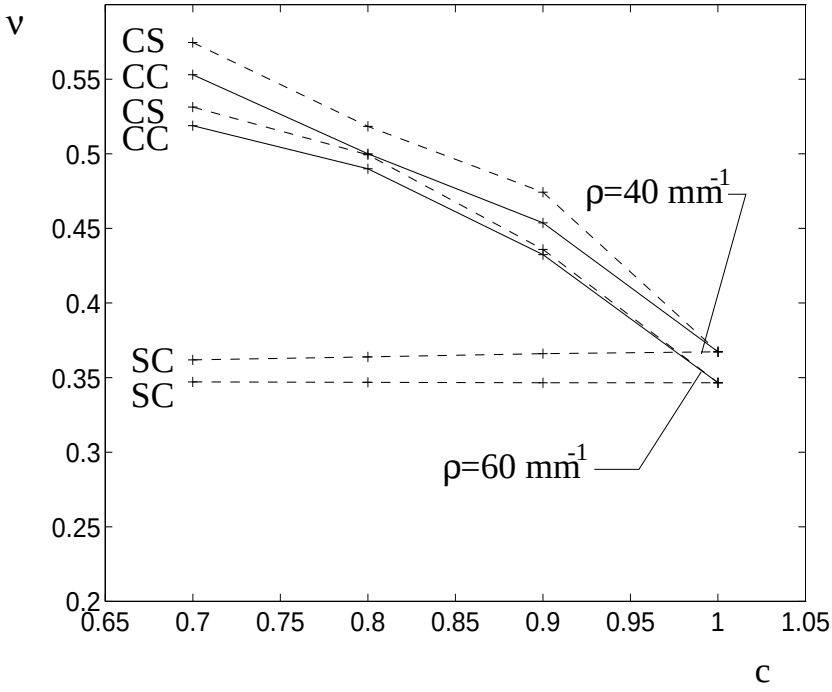

Figure 7.17: *ν against curl index, c.*

7.5. Global elastic stiffness vs orientation distribution

In the preceding sections the results have been presented by giving Young's modulus and Poisson's ratio for the isotropic material which most closely resembles the simulated material in mechanical behaviour. This has been done because when the fibres have a uniform orientation distribution the network is expected to be close to isotropic, at least at sufficiently high network densities.

Now, we also want to investigate the influence on the elastic stiffness of non-uniform orientation distribution of the fibres. Then there is no longer any reason to believe that the network's performance will be the same in every direction. If, however, the orientation distribution is symmetric with respect to two perpendicular directions, we can expect nearly orthotropic behaviour. Some orientation distributions satisfying this condition are examined, and the results are given as orthotropic material parameters according to the principles presented in Section 6.7.

One possible way to define an orientation distribution is, see [29],

$$f(\alpha) = \frac{1}{\pi} - a\cos 2\alpha. \tag{7.3}$$

This distribution function satisfies the criterion

$$\int_0^\pi f(\alpha)\mathrm{d}\alpha = 1, \tag{7.4}$$

for all values of the constant a, but to avoid negative probabilities it should only be used for $0 \leq a \leq 1/\pi$. Simulations have been made for the cases of $a = 0$, $1/(2\pi)$ and $1/\pi$, which give the distribution functions shown in Figure 7.18. In the diagram the curves have been approximated by ten straight line segments, and this is also the input given to the program which generates the network. As a comparison, Figure 7.19 shows an example of a fibre orientation distribution of a commercial kraft paper, taken from [29]. The network with $a = 0$ is the basic example network, and for the other values of a all properties except the orientation distribution are the same as for the basic example network. Figure 7.20 shows examples of network geometries for the three different values of a. For each value of a, 10 simulations were made of nominally equal networks.

The simulations for $a = 0$ are the same as those made for the basic example network, but they are now evaluated as for an orthotropic material. Ideally, E_x and E_y as well as ν_{yx} and ν_{xy} should be identical. That they are not, implies that the networks which have nominally uniform orientation distribution are not exactly isotropic, but still they are quite close. As a increases there is a stronger tendency for the fibres to be oriented vertically, as can be seen from Figures 7.18 and 7.20. This results in an increasing modulus E_y and decreasing E_x, as can be seen in Figure 7.21, where the mean values and standard deviation of the E_x, E_y and G_{xy} obtained are indicated. The shear modulus G_{xy} decreases only slightly as a increases. In Figure 7.22 Poisson's ratios ν_{yx} and ν_{xy} are shown against a. At a=0 they are almost the same, but as a increases, ν_{yx} increases a considerable amount while ν_{xy} decreases moderately.

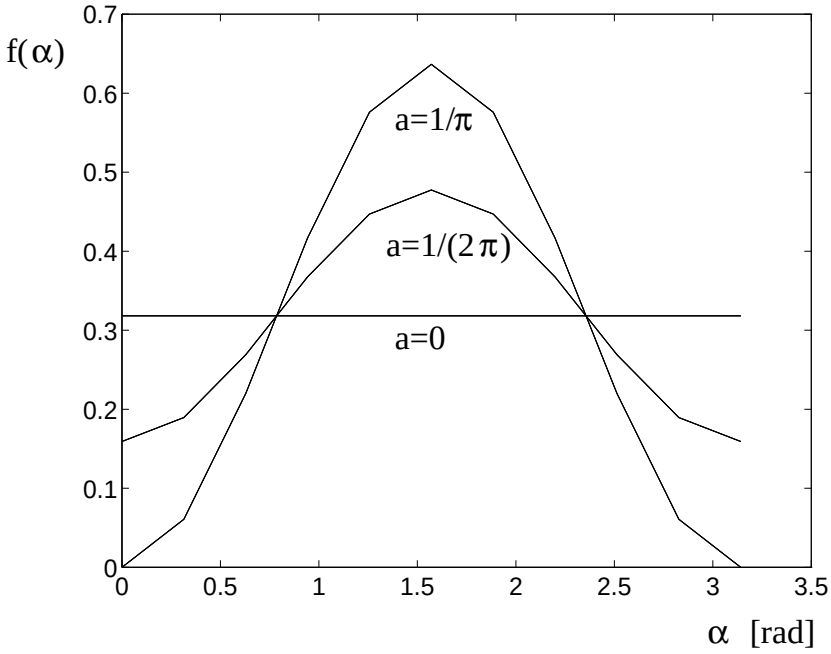

Figure 7.18: *Fibre orientation distribution.*

Finally, Figure 7.23 shows a typical example illustrating the difference between $\boldsymbol{D}$ from a simulation, denoted $\boldsymbol{D}^s$, and the corresponding estimated orthotropic $\boldsymbol{D}$, denoted $\boldsymbol{D}^e$, as a function of θ. The diagram is from a simulation where $a = 1/(2\pi)$ and $\boldsymbol{D}^s$ is

$$\boldsymbol{D}^s = \begin{bmatrix} 0.6130 & 0.3340 & 0.0273 \\ 0.3340 & 1.3236 & 0.0328 \\ 0.0273 & 0.0328 & 0.3146 \end{bmatrix} \cdot 10^5,$$

and the estimated orthotropic $\boldsymbol{D}^e$ is, from Section 6.7,

$$\boldsymbol{D}^e = \begin{bmatrix} 0.6130 & 0.3340 & 0 \\ 0.3340 & 1.3236 & 0 \\ 0 & 0 & 0.3146 \end{bmatrix} \cdot 10^5.$$

The difference between the solid lines which represent $\boldsymbol{D}^s$ and the dotted lines which are $\boldsymbol{D}^e$ is rather small. This indicates that the assumption discussed in Section 6.7, i.e. assuming the principal directions of the simulated material to be coincident with the symmetry axes of the orientation distribution, seems to be acceptable.

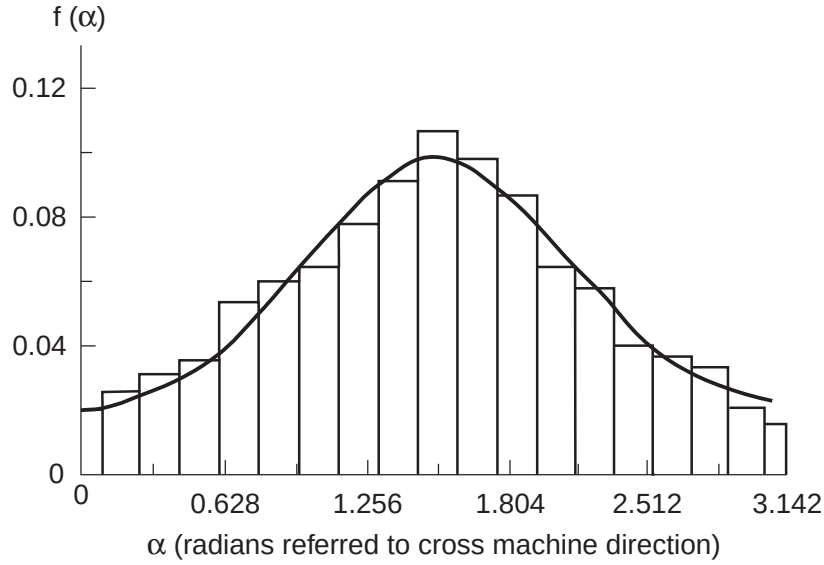

Figure 7.19: *Fibre orientation distribution of commercial kraft paper,* [29].

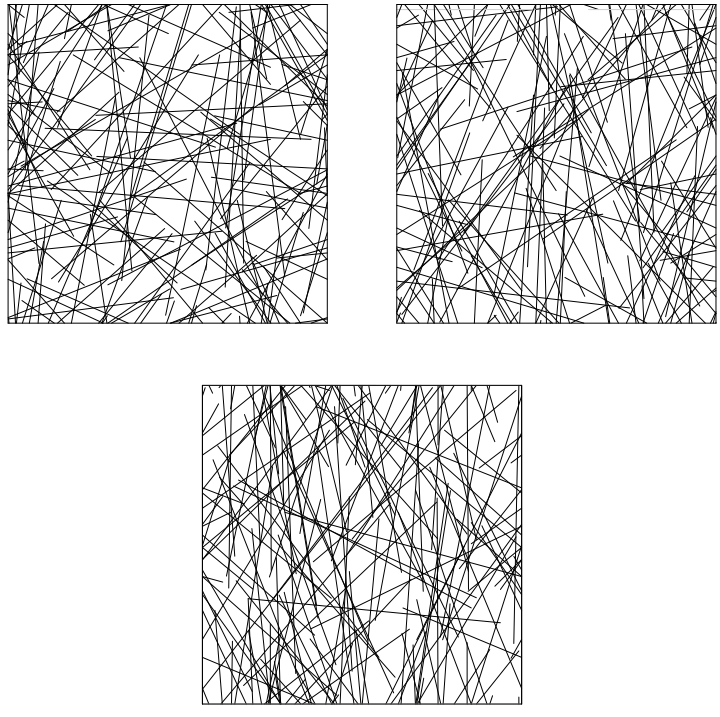

Figure 7.20: *Examples of network geometries for the cases a=0,* $a = 1/(2\pi)$ *and* $a = 1/\pi$.

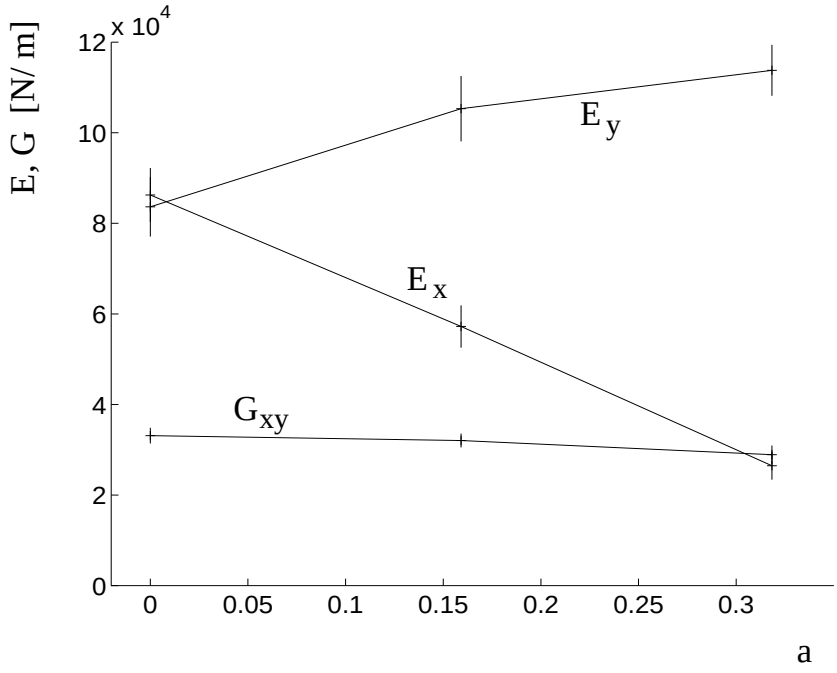

Figure 7.21: *Elastic moduli against orientation distribution parameter a.*

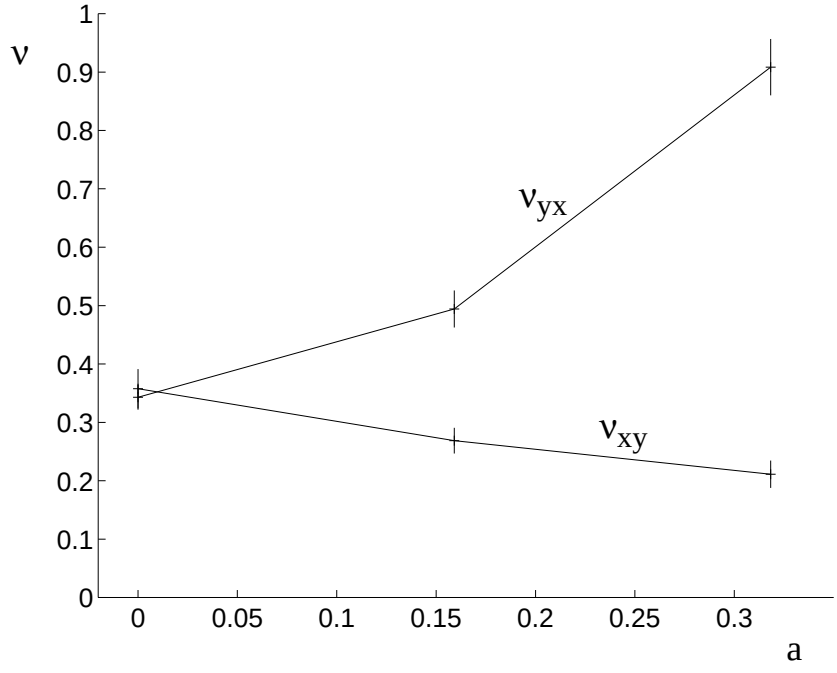

Figure 7.22: *Poisson's ratios against orientation distribution parameter a.*

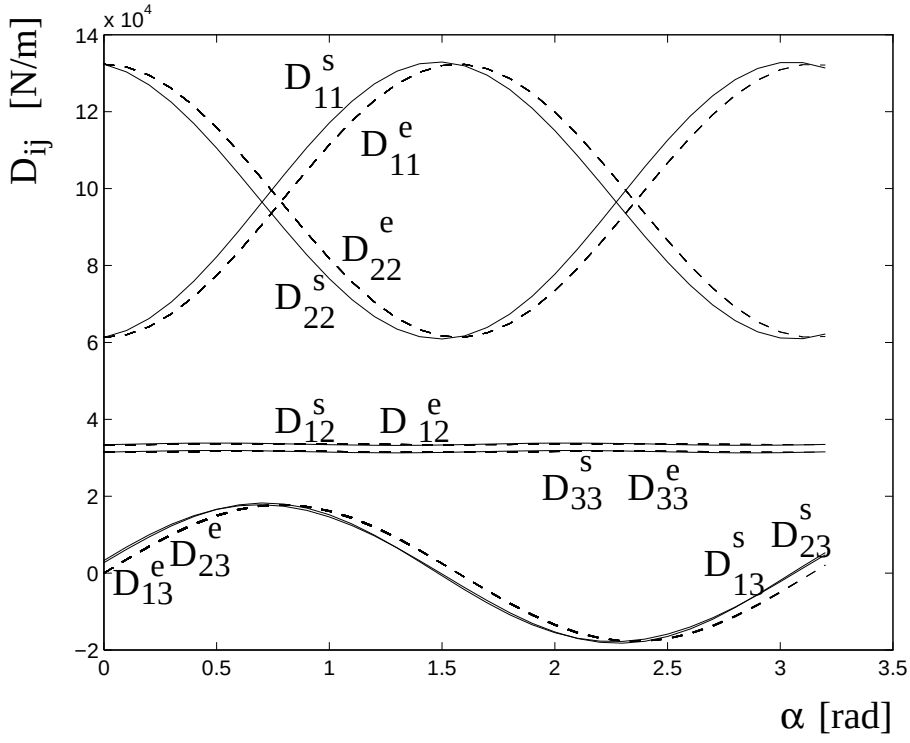

Figure 7.23: *Components D_{ij} against α.*

7.6. Global elastic stiffness vs length distribution

The length of the fibres has great influence on the stiffness properties of a network. Extremely short fibres are like dust and do not constitute a connected structure. As fibres get longer the structure gradually becomes more like a real network and gets stiffer. This effect can be seen from Figure 7.24, where E is plotted against fibre length for networks which are all of constant fibre length and network density 40 mm^{-1}. The solid line in the diagram connects points which show averages from ten calculations. Vertical lines denote standard deviation. Young's modulus increases considerably as the fibre length is increased at constant network density. Poisson's ratio, on the other hand, is stable around 0.33-0.34 for all fibre lengths investigated, which can be seen from Figure 7.25.

When all fibres are of the same length the simulations show quite clearly that longer fibres give a stiffer network and that Poisson's ratio is not much affected. In order to investigate the case when fibre length is given by a statistical distribution, networks with the same network density, 40 mm^{-1}, but length distribution similar to that of Figure 5.1 are simulated. The population distribution in length, the weighted length distribution and the cumulative population distribution in length of the fibres are given in Figure 7.26. It should be noted that in the last column

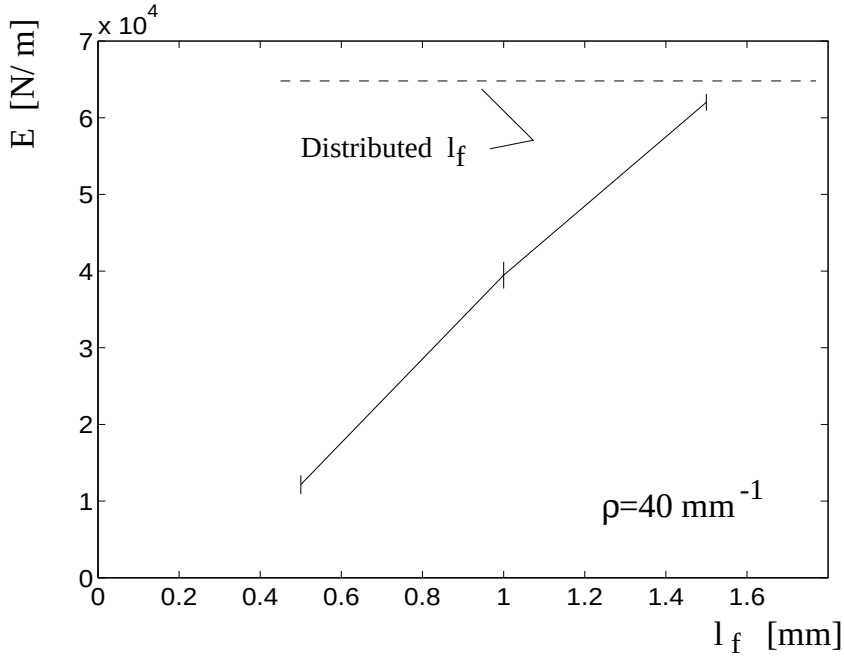

Figure 7.24: *Young's modulus against fibre length.*

of the population distribution there is an overrepresentation of 4 mm fibres, since from the cumulative population distribution 2 % of the fibres are exactly 4 mm. The arithmetic mean fibre length is 0.85 mm and the weighted mean fibre length 1.77 mm. The mean value of E from ten simulations is $6.48 \cdot 10^4$ N/m; this value is shown by the dashed line in Figure 7.24. If the network with varying fibre length is going to be described by some characteristic fibre length with regard to initial Young's modulus, the arithmetic mean fibre length does not seem to be the appropriate value. For the case investigated the constant fibre length which gives the same value of E is approximately 1.55 mm, which is closer to the weighted mean fibre length. More simulations are needed to confirm this hypothesis, but it seems probable that this tendency holds, since longer fibres contribute more to the stiffness of the network. Average Poisson's ratio for the networks of varying fibre length is 0.336, that is, Poisson's ratio does not seem to be affected by either mean fibre length or length distribution.

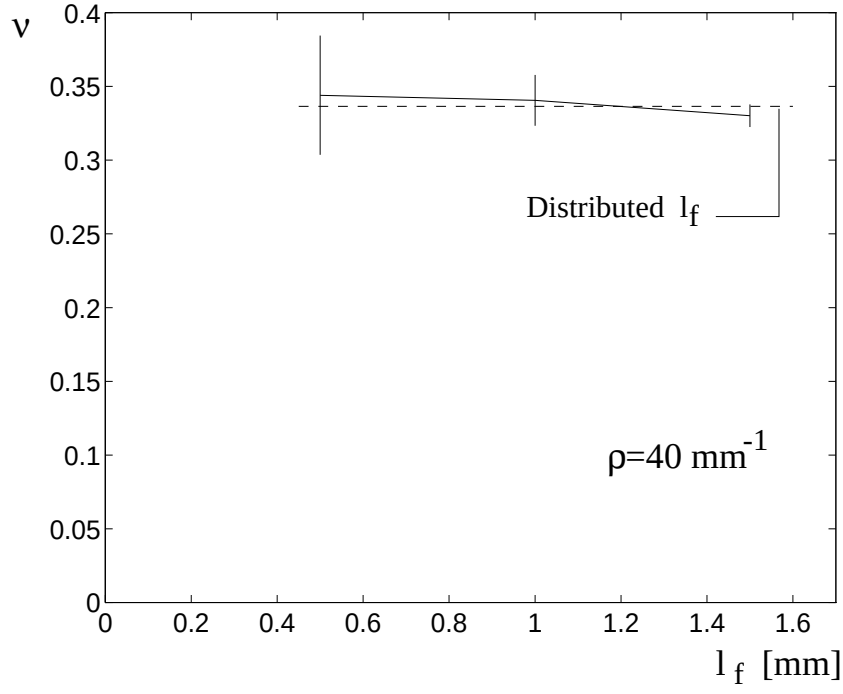

Figure 7.25: *Poisson's ratio against fibre length.*

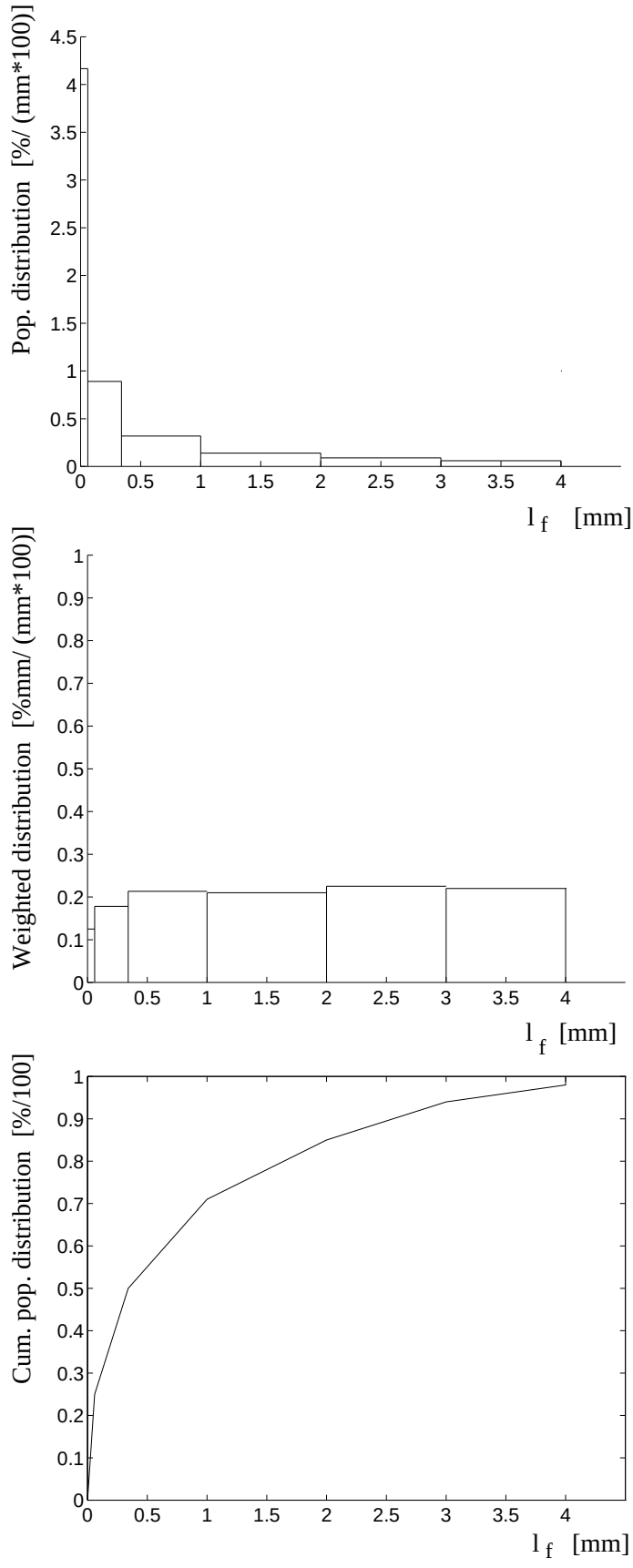

Figure 7.26: *Population distribution, weighted distribution and cumulative population distribution of fibre length.*

8. Analysis of fracture process

The fracture of a heterogeneous structure is a non-linear process, the properties of the structure changing as the failure progresses in the material. The non-linear analysis of fracture can, however, be performed as a series of linear steps, if it is assumed that the behaviour of each component of the structure is step-wise linear. This approach is used, and it is further described in Section 8.2. The fracture criteria and behaviour of the components of the network are defined in Chapter 3, and the numerical values used are given in the next section. The fracture process of a material is more complex to quantify than are the initial stiffness properties. The output parameters used to characterize fracture in this study are discussed in Section 8.3.

8.1. Input parameters to fracture analysis

The input parameters for the fracture analysis are given in the form of an example network. In the next chapter different parameters from this basic fracture example network are varied, and their influence on the fracture behaviour of the network is obtained.

The input parameters needed for the basic fracture example network are much the same as those of the basic example network of Section 5.1. The fibre length, however, is changed, and the parameters relevant for fracture calculations are added.

Since the results from Section 7.6 indicate that the weighted mean fibre length is more relevant for the mechanical properties of a network than is the arithmetic mean, the fracture simulations are performed with a fibre length of 2 mm. This means that the square studied needs to be bigger. If the initial stiffness is considered, it was concluded in Section 7.1 that a side-length of the square of 1.2 times the fibre length is sufficient. When fracture localization phenomena are studied, results in the next chapter indicate that the square needs to be about twice the fibre length. For the basic fracture example a side-length L=4 mm is thus chosen. Most of the initial stiffness simulations were made with a value of L=1.2 mm. This means that for the same density, there is approximately $4^2/1.2^2 = 11$ times more degrees of freedom for the fracture example network. This and the fact that each simulation now consists of many steps entails numerically very much heavier calculations. On the other hand, it has been decided to assume a lower network density in the basic fracture example network; ρ=8.7 mm^{-1} instead of 60 mm^{-1}. In relation to a typical fluff material of the kind used in diapers, ρ=8.7 mm^{-1} is estimated to be more realistic in terms of the corresponding number of fibre-to-fibre connections per unit fibre length.

The ultimate tensile stress of softwoods such as spruce or pine, containing no faults, is about 100 MPa in the direction of the fibres. The cross section of wood, however, partly consists of pore-space, indicating a higher value of ultimate stress for the material in a single fibre. Yet the fibre is weakened by the defibration process, and the ultimate normal stress for a fibre is therefore set to 100 MPa in the basic fracture example network. The ultimate shear stress is set to a lower value, 50 MPa.

The strength parameters of the fibre-to-fibre bonds can at present be estimated only in a very rough manner. It is known that in a dry-shaped cellulose fibre material where no adhesive have been added, it is the bonds that break, and not the fibres. From this consideration, and the intention that the parts of degree of utilization originating from translation and rotation respectively be of the same order of size, the values have been chosen to F_{ult}=3.5·10^{-3} N and M_{ult}=5.6·10^{-9} Nm. For the basic fracture example network, completely brittle failure of connections is assumed, and n_s is thus set to 1.

The input parameters of the basic fracture example network are summarized in Table 8.1, which also indicates in which section a certain parameter is varied. Where nothing else is said, the simulations in Chapter 9 refer to networks having the properties of Table 8.1.

Table 8.1: *Input parameters of the basic fracture example network.*

Parameter	Value and unit	Varied in Section
l_f	2 mm	9.5
κ	0 mm^{-1}	9.5
A_f	$2.5 \cdot 10^{-10}$ m^2	
I_f	$0.2 \cdot 10^{-20}$ m^4	
E_f	$35 \cdot 10^9$ Pa	
σ_{ult}	100 MPa	9.2
τ_{ult}	50 MPa	9.2
$k_{x1} = k_{y1}$	8750 N/m	9.3
$k_{\phi 1}$	$2.8 \cdot 10^{-7}$ Nm/rad	9.3
F_{ult1}	$3.5 \cdot 10^{-3}$ N	9.2, 9.3
M_{ult1}	$5.6 \cdot 10^{-9}$ Nm	9.2, 9.3
n_s	1	9.3, 9.5
β_1	1.0	9.3, 9.5
β_2	1.0	
L_x, L_y	4 mm	9.1, 9.5
ρ	8.7 mm^{-1}	9.4, 9.5
N_α	$\frac{1}{\pi}, \quad 0 < \alpha < \pi$	
s	1.0	9.5
$d(x, y)$	1.0	

8.2. Method of analysis

A fracture analysis can be performed as a series of linear steps, on assuming that the behaviour of each component of the structure is step-wise linear. Using this method for non-linear analysis, the equilibrium conditions are, apart from effects of round-off errors, fulfilled exactly during the entire course of loading and fracture. The drift from the equilibrium path that may occur in conventional incremental analysis is avoided, and there is no need for iterations as in methods of the Newton-Raphson kind.

In the present analysis, in each step a unit strain is first applied to the structure. The degree of utilization, see (8.2) and (8.3), is then calculated for each element, and the element that is utilized the most is detected. The applied strain is proportioned so that the degree of utilization is exactly unity in the most severely stressed element. The reaction forces obtained are proportioned to the same degree, and thus we obtain corresponding values of stress and strain for the situation when the first element is about to break, or more general, change its properties into new linear characteristics. Next, the global stiffness matrix is adjusted according to the new properties of the partly broken element, and a new linear step is performed. This process can go on until the structure has collapsed entirely and cannot sustain load any more.

Each linear step is performed according to the principles of Chapter 6, using cyclic boundary and loading conditions. The procedure of finding and removing the most severely loaded element between two successive steps is described in the following.

The element forces are calculated from (6.2), which is repeated here:

$$\boldsymbol{K}_e \boldsymbol{u} = \boldsymbol{f} \tag{8.1}$$

$\boldsymbol{K}_e$ is the element stiffness matrix, referred to global coordinate directions, and $\boldsymbol{u}$ is the vector of displacements in the directions of the global degrees of freedom of the element. $\boldsymbol{f}$ is also referred to global directions, and has to be transformed to the local element directions before it is used in a fracture criterion. This is valid for the beam elements, since, in the model used in this study, the connection elements have the same local and global directions.

From the fracture criterion (3.2) we can see that the degree of utilization, m, for a beam element is

$$m = \max \left\{ \begin{array}{c} \dfrac{|\sigma_n|}{\sigma_{ult}} \\ \dfrac{|\tau|}{\tau_{ult}} \end{array} \right. , \tag{8.2}$$

where, according to (3.3) and (3.4), for a straight beam of rectangular cross section

$$\sigma_n = \pm \frac{N}{A_f} \pm \frac{M}{I_f} \sqrt{\frac{3I_f}{A_f}},$$

and

$$\tau = \frac{1.5V}{A_f}.$$

N, M and V denote normal force, bending moment and shear force in the most stressed section of the beam. Since there is no load on the beams between the connection elements, N and V are constant throughout the element, and M varies linearly and thus reaches its maximum value in one of the element ends.

The degree of utilization for a spring element is, from (3.7),

$$m = \frac{\sqrt{F_x^2 + F_y^2}}{F_{ult}} + \frac{|M|}{M_{ult}}. \tag{8.3}$$

When an element of the structure reaches a degree of utilization of unity it breaks, and the properties of the network structure become different. When a beam element breaks, it does so in a brittle manner. This is taken care of by assembling into the system stiffness matrix the negative of the broken element's stiffness matrix, that is by removing this element from the system. When the fracture criterion for a connection is fulfilled, the system stiffness matrix is adjusted in a similar way, except that the spring element is not removed altogether. If we have the reduction coefficient for spring stiffness, β_1, see Figure 3.4, the negative element stiffness matrix multiplied by $(1 - \beta_1)$ is assembled into the system stiffness matrix, except when the connection reaches final failure and is removed altogether.

Loading of a network is defined in terms of global straining of the network. The strain state is described by the strain vector $\boldsymbol{\epsilon}=(\epsilon_x, \epsilon_y, \gamma_{xy})$, which has three components. A strain state can thus be viewed as a point in a three- dimensional strain space, and the loading of a structure can be represented by a path in strain space. When using the method outlined above the path must be composed of piece-wise straight lines.

The simplest case is to follow a straight line from the origin. This means that the ratios between the single strain components are fixed, and only one calculation needs to be performed during each step. All simulations reported on in the next chapter are of this type, and the line followed from the origin is the ϵ_x-axis. Typically, the path from original structure to complete failure consists of a 'two-steps-forward one-step-back' walk on the ϵ_x-axis. It is equally simple to follow one line from the origin to a certain extent and thereafter change into another one. An example of this is to strain the material in the x-direction until it is partly broken, unload the structure and then subject it to pure tension in the y-direction until complete failure. A more complex situation arises if one wants to study a strain path that does not pass the origin, for example constant strain in the x-direction under increasing strain in the y-direction. Under these circumstances three calculations have to be performed in each step, corresponding to pure tension in the x-direction, in the y-direction and pure shear. This is because, since the strain components do not increase proportionally, the effect of each strain component on each element of the structure must be obtained.

It should be noted that all simulations in this study are based on small-strain-theory. Most of the results in the next chapter are within the small-strain range, the few which are not might be unreliable.

8.3. Output parameters from fracture analysis

One important output from a fracture analysis is the set of points in the $\sigma_x\epsilon_x$-plane, representing global force in the direction of straining versus global straining. By definition

$$\sigma_x = F_x/L_y, \tag{8.4}$$

$$\epsilon_x = \Delta u_x/L_x. \tag{8.5}$$

Each $\sigma_x\epsilon_x$-point corresponds to the fracture, partial or complete, of one component of the structure. Each linear step performed can be represented by a line extending from the origin to the point where the first element fails in that step. Since the stiffness of a structure decreases as more components fail, the chronological order of the failure points is defined by a successively smaller inclination of the lines from the origin to the point.

A lot of information can be extracted from the points. The inclination of the line from the origin to the first point is the initial stiffness of the network, denoted $(\sigma_x/\epsilon_x)_0$. The highest value of the global mean stress reached is denoted maximum stress, σ_{max}, and the corresponding value of strain is denoted limit strain, ϵ_{lim}. The ultimate strain, ϵ_{ult}, that is the strain at which the last component fails and leaves the network completely separated, is not used to characterize the material in this study, since there is a considerable scatter in this value between different nominally equal networks. The very last point may also be dubious due to numerical problems arising when the structure approaches zero stiffness. An integrated measure of the straining capacity which is not so sensitive to the variations in single points is preferred. Fracture energy is such a measure. The different output parameters, except fracture energy, obtained from the global $\sigma_x\epsilon_x$-response are summarized in Figure 8.1, where the points have been joined by straight lines. Fracture energy and its coupling to internal elastic energy is discussed in more detail in the following.

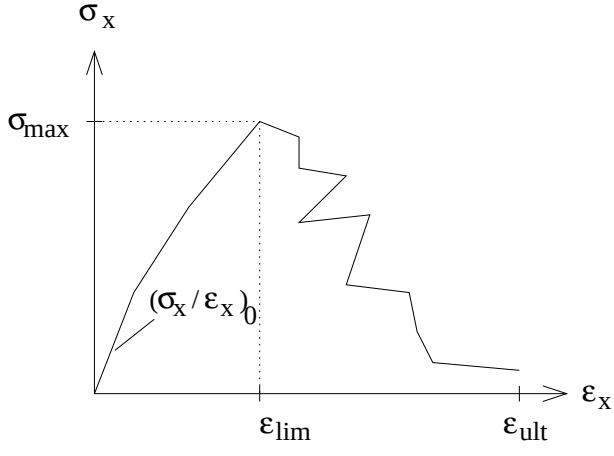

Figure 8.1: *Illustration of some fracture output parameters.*

The amount of energy that has to be supplied to a network to cause its complete failure is an important parameter. Other parameters kept constant, a low fracture energy implies a sudden, brittle mode of failure, while a higher value means fracture in a more ductile manner.

In each linear step, the external energy that has been supplied to the system is equal to the internal energy stored in the structure. Since the work w of a force F is

$$w = \int F \mathrm{d}(\Delta u), \tag{8.6}$$

the internal elastic strain energy stored in a linear spring, w_i^s, is

$$w_i^s = \int k(\Delta u)\mathrm{d}(\Delta u) = \frac{k(\Delta u)^2}{2}. \tag{8.7}$$

Here k denotes spring stiffness and Δu extension of spring. For a connection element of the type used in this study, made up of three springs, this gives the total elastic strain energy, w_i^c

$$w_i^c = \frac{k_x(\Delta u_x)^2}{2} + \frac{k_y(\Delta u_y)^2}{2} + \frac{k_\phi(\theta)^2}{2}. \tag{8.8}$$

Δu_x denotes extension in x-direction of the x-spring, and Δu_y and $\Delta\theta$ are the corresponding quantities for the other two springs.

Fracture has in (3.6) been defined to occur in a connection element when

$$g(\boldsymbol{F}) = 0,$$

where g is defined in (3.7). The path from the point where the fracture criterion is reached, down to zero force in the spring, has been defined to be a vertical line in Figure 3.4. This means that the fracture of a single connection is assumed to be a stable process, without any dynamic effects. An alternative assumption could be a fracture curve as in Figure 8.2, where the difference between the strain energy in the spring at start of fracture and the fracture energy consumed by the spring material, goes into kinetic energy during an unstable fracture resulting in dynamic effects.

For a fibre segment, which is modelled as a Bernoulli beam, axial extension and bending contributes to the internal elastic strain energy, w_i^f, cf. [24].

$$w_i^f = \int \frac{N^2}{2E_f A_f}\mathrm{d}x + \int \frac{M^2}{2E_f I_f}\mathrm{d}x, \tag{8.9}$$

where N and M denote axial force and bending moment in the fibre segment, and the integration is performed along the axis of the beam.

The external energy w_e^n supplied to a network is the integral of force times displacement in the boundary nodes. When cyclic boundary and loading conditions are used, the reaction forces in two opposite nodes are always equal in magnitude and opposite in direction. This means that if a network is subjected to strain $\boldsymbol{\epsilon}= (\epsilon_x, 0, 0)$ the external energy supplied to the network in a linear step, w_e^n, is simply

$$w_e^n = \frac{F_x \epsilon_x L_x}{2}, \tag{8.10}$$

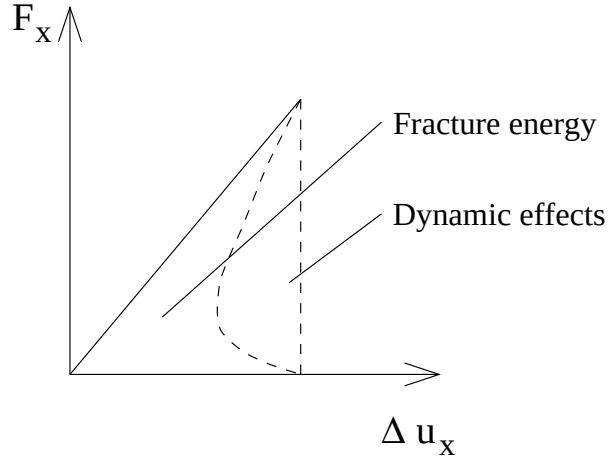

Figure 8.2: *Force-extension diagram for a spring. Alternative where part of the elastic energy gives dynamic effects at failure.*

F_x denoting resultant force in the x-direction on the faces of the network that are perpendicular to the x-axis, L_x being length of studied square in the x-direction.

In a linear step, w_e^n, which is equal to the area under the $F_x - \Delta u_x$-graph for the network is equal to the sum of the internal strain energies of all the elements of the network, see Figure 8.3,

$$w_e^n = \Sigma w_i^c + \Sigma w_i^f . \tag{8.11}$$

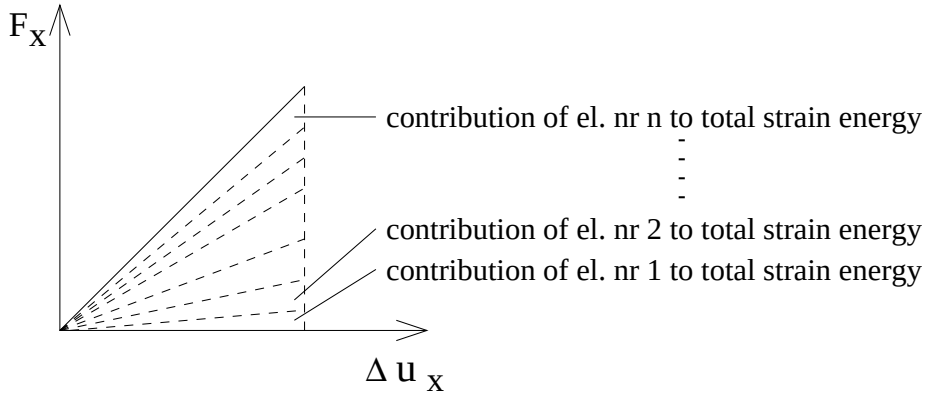

Figure 8.3: *The external energy is equal to the sum of the internal elastic strain energies of the components of the network.*

Within each linear step there is thus equality between external and internal energy. Now, we want to compare the internal elastic energy stored in the structure

in two successive steps. A network is assumed to be loaded to the extent of failure of the most severely stressed element; this element fails and the new structure obtained when the failed element is removed is loaded to the same strain. The value of F_x will now be lower for the same value of Δu_x since the structure has lost in stiffness due to the removal of the fractured element. Thus the internal strain energy is now smaller, and the difference between the total internal strain energies before and after the element failure consists of the fracture energy of the failed element plus energy lost because of load redistribution within the network; see Figure 8.4 for a simple symbolic example. The fracture energy of a network, w^n, is thus larger than the

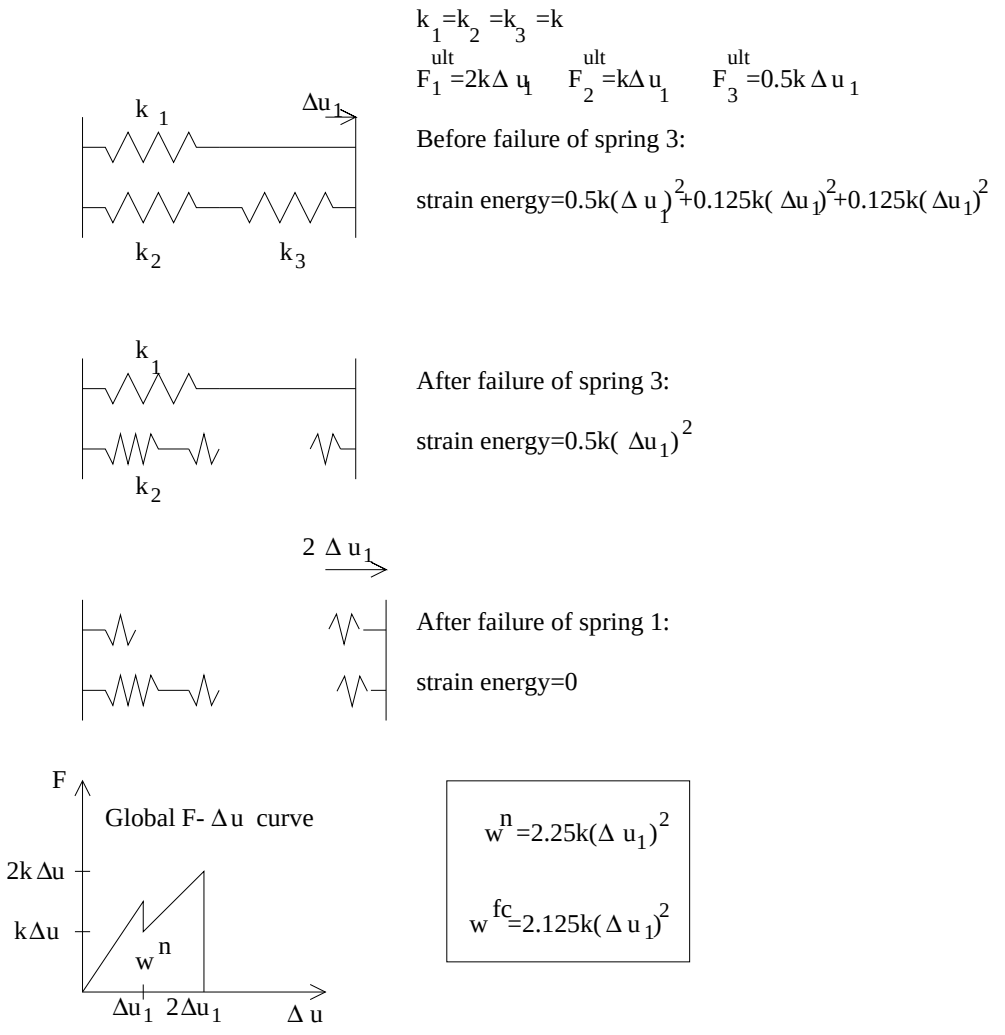

Figure 8.4: *Strain energy at different stages of failure.*

sum of the fracture energies of the failed components, Σw^{fc}.

$$w^n \geq \Sigma w^{fc}, \tag{8.12}$$

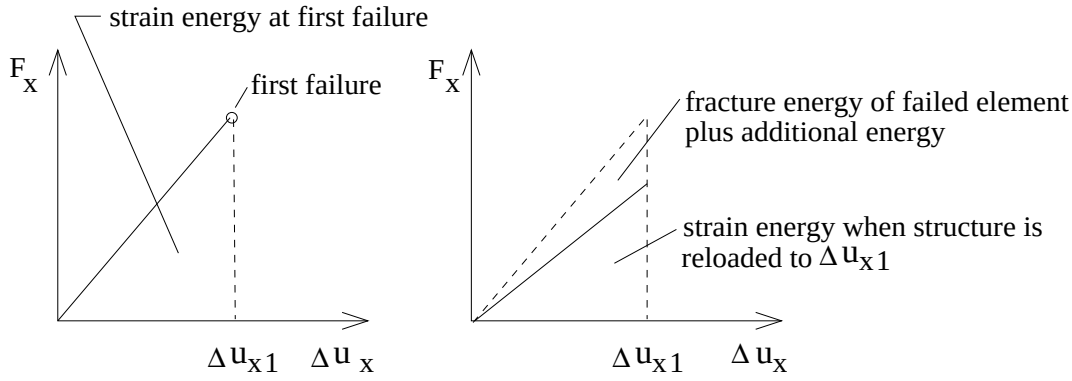

Figure 8.5: *Strain energy in system before and after element failure.*

$$w^n = \int_0^{\epsilon_{ult}} F_x L_x \mathrm{d}\epsilon_x. \tag{8.13}$$

The total fracture energy of a network is the area under a curve joining the points in some way. Figure 8.6 shows two different ways of joining the points, representing different fracture mechanisms, the second of which is used when fracture energy is evaluated in the next chapter.

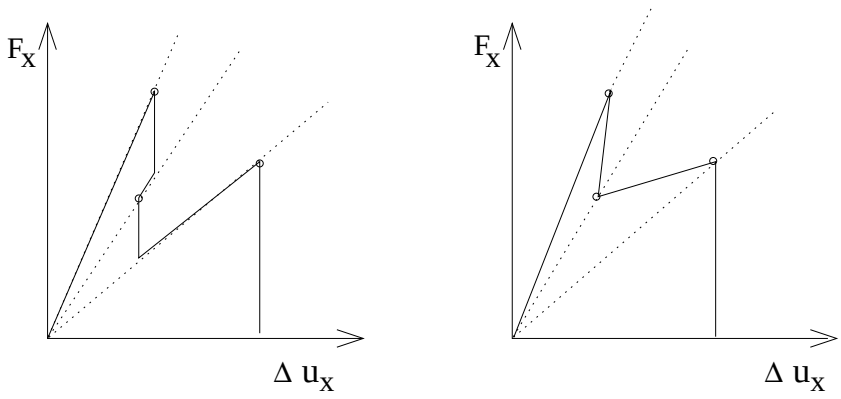

Figure 8.6: *Different ways of calculating the fracture energy.*

The total fracture energy, w^n, is divided into two parts, the part before maximum load is reached, w_1^n, and the part after maximum load, w_2^n, see Figure 8.7. w_1^n represents the loss of energy, the dissipation, when a structure is loaded to maximum load and then unloaded. This energy is related to the more or less evenly distributed damage of the material when the global load is increasing. If the network is reasonably homogeneous one may, as a first approximation, assume w_1^n to be proportional to the size of the network, $L_x L_y$.

w_2^n represents the dissipation when the global load F_x is decreasing, as Δu_x is

increasing. When F_x is decreasing the parts of the structure outside a localized fracturing region are unloaded and contract elastically without any dissipation. The dissipation w_2^n is instead due to the increasing strain and fracture taking place in the localized fracture process region. Since the fracture events after peak global load can be assumed to be localized to one section, one may, as a first approximation, assume w_2^n to be proportional to L_y. The ratio w_2^n/L_y corresponds directly to the material parameter 'critical energy release rate, G_c', used in linear elastic fracture mechanics, and to the fracture energy, G_f, used in non-linear fracture mechanics. Here the notation

$$G_f = w_2^n/L_y \tag{8.14}$$

will be used.

From the fracture energy G_f, the strength σ_{max} and the stiffness $(\sigma_x/\epsilon_x)_0$, an absolute length scale characteristic for the material can be defined as

$$l_{ch} = (\sigma_x/\epsilon_x)_0 G_f/\sigma_{max}^2. \tag{8.15}$$

Dealing with analysis of fracture, such an intrinsic length is needed due to the size effects during fracture, even for homogeneous materials. l_{ch} is also a measure of the brittleness of the material, a low value indicating a brittle material, and corresponding directly to the ratio $(K_c/\sigma_{max})^2$ used in linear elastic fracture mechanics, K_c being the fracture toughness of the material. Empirically it has been found that l_{ch} is usually related to the geometrical size of the particles and pores etc. in a material. In the present calculation of l_{ch}, $(\sigma_x/\epsilon_x)_0$ is used as the measure of the elastic stiffness of the material. For some applications E or $\sigma_{max}/\epsilon_{lim}$ can be more relevant alternative measures of the elastic stiffness. Values of l_{ch} for various materials are reported in [9].

The $\sigma_x\epsilon_x$-curves obtained from simulations show a strong saw-tooth behaviour. This kind of fracture behaviour is usually not seen in experimental curves. This is because a very fast unloading of the material would be required to be able to follow a curve that exposes snap-back performance, faster than is possible to obtain in practice. In deformation-controlled experiments the strain is not allowed to decrease at all, making it impossible to record the snap-back behaviour of the sample, see Figure 8.8. Although difficult to record experimentally, the saw-tooth kind of behaviour may not be unrealistic: if testing a sample as small as those studied by numerical simulations, each individual fracture event within the micro-structure of the material might very well give a noticeable saw-tooth in the global $\sigma_x\epsilon_x$-curve.

In addition to the stress-strain relationship of the network it is also interesting to study localization of the fracture. This is done by plotting the failed connections, the zero-stress beams or the remaining active structure of the network as fracture progresses.

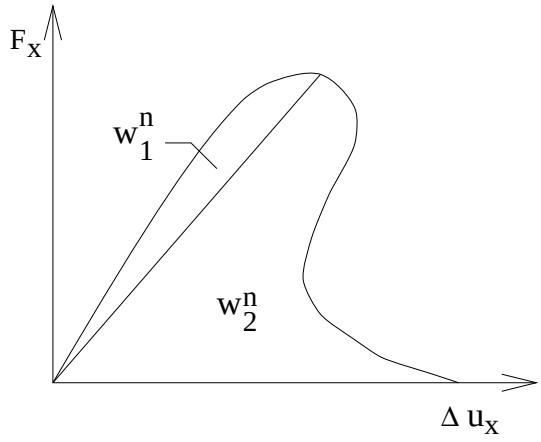

Figure 8.7: *Definition of w_1^n and w_2^n.*

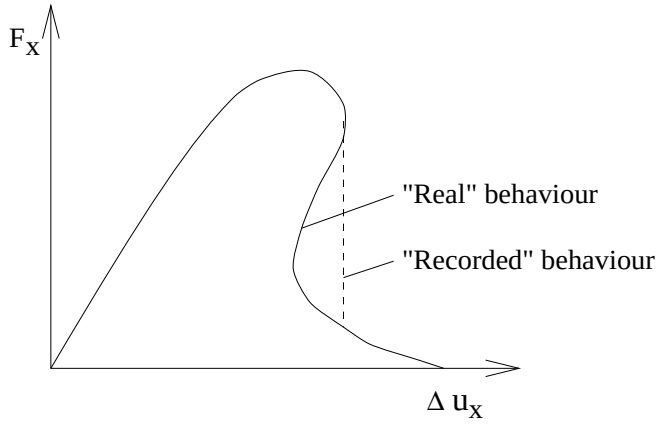

Figure 8.8: *Snap-back behaviour.*

9. Results from analysis of fracture process

9.1. Effect of sample size

The results obtained from a fracture test or simulation of a heterogeneous material are dependent on the sample size. This effect can be seen in a series of simulations where the shape and size of the sample have been varied. The cells shown in Figure 9.1 have been subjected to uniaxial tension in the x-direction, $\boldsymbol{\epsilon} = (\epsilon_x, 0, 0)$, and maximum stress, initial stiffness, fracture energy and localization have been evaluated. Apart from the cell size, all properties of the networks are according to Table 8.1. Only fracture of connections is considered. For each cell size five simulations were made, and the averages of those results are given in the following figures.

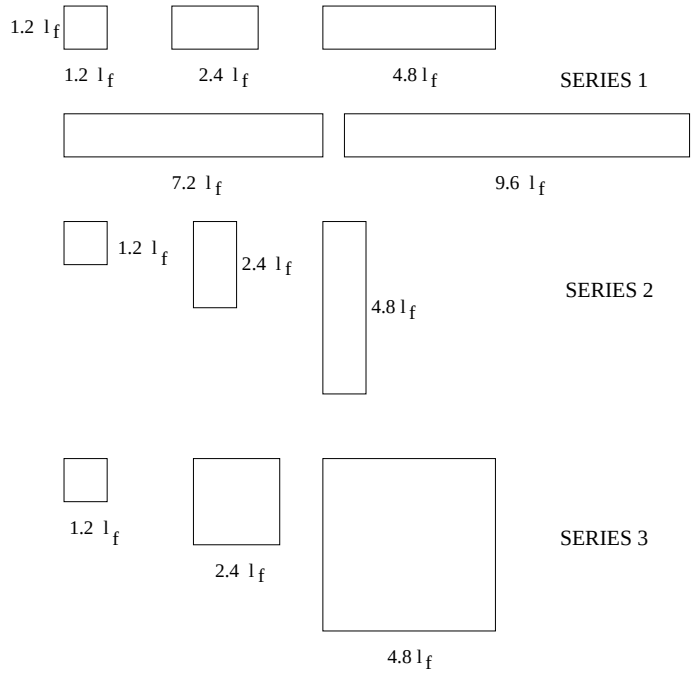

Figure 9.1: *Shape and size of investigated cells.*

If we regard the square with side-length $L = 1.2l_f$ as a basic unit cell, the

following samples in series 1 are 2, 4, 6 and 8 times as long as the basic cell. These longer samples should, however, not be regarded as a number of statistically equal unit cells coupled in series. In general the weakest link will determine the strength of a serial system. This phenomenon is described by Weibull theory for certain serial systems, cf. [4]. As the number of cells coupled in series increases, the probability of a really weak cell increases, and therefore it is expected that the strength will decrease as the length of the sample in the loading direction increases. That this is also the case for the computational results; see Figure 9.2, where maximum stress is plotted against L/l_f for series 1.

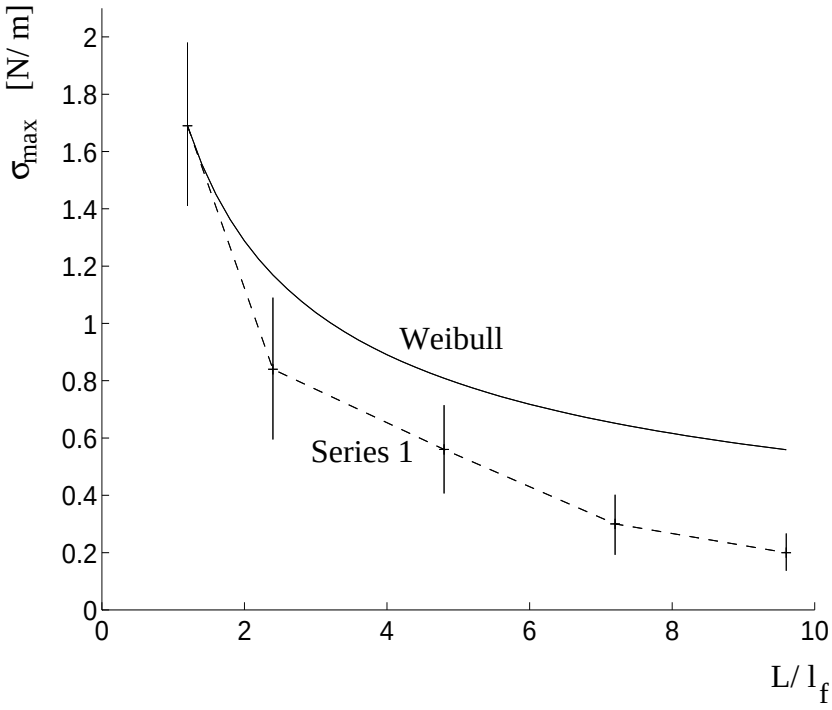

Figure 9.2: *Maximum stress against L/l_f for series 1.*

The dashed line connects the average of the simulation results with vertical lines denoting standard deviation. The solid line shows the size effect prediction of Weibull theory, which is

$$\frac{\sigma^a_{max}}{\sigma^b_{max}} = (\frac{l^a_s}{l^b_s})^{1/m}, \tag{9.1}$$

where l^a_s and l^b_s are lengths of two samples a and b, and m is a function of the coefficient of variation, cf. [9]. In Figure 9.2, m, which is 1.88, is based on the average coefficient of variation of the different cell sizes, 0.56. The simulation results show a stronger decrease in strength than is predicted by Weibull theory. This is because a basic assumption of Weibull theory is not fulfilled in the present case. In Weibull theory the cells coupled in series are assumed to have the same strength

distribution as the sample made up of a single cell. This condition would have been fulfilled if the network had been generated in such a way that the density in each of the square cells coupled in series had been the same. In the present case, however, the network is generated with a prescribed average network density for the whole sample, and due to the random positioning of the fibres there are variations in the average network density from one region of the basic cell to another. Since the weakest link determines the strength, fracture will in general occur in a region of low density. The average of the network density in the fracture zone, taken as a strip of width equal to the fibre length across the sample, is shown in Figure 9.3, vertical lines denoting standard deviation.

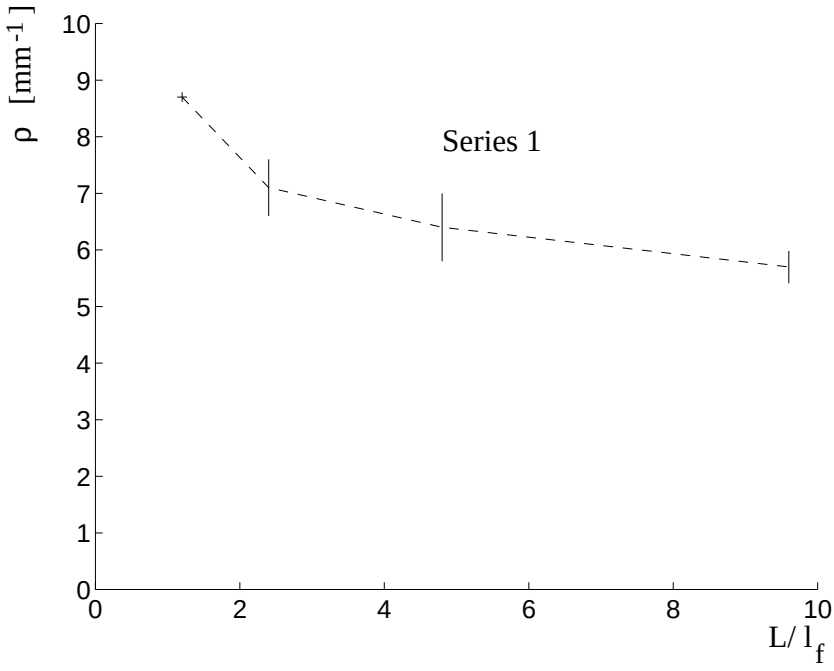

Figure 9.3: *Average network density in fracture zone against L/l_f for series 1.*

While the strength of a sample of length $9.6l_f$ is determined by a zone of density 5.7 mm^{-1}, the strength of a sample of length $1.2l_f$ is determined by a fracture zone which is almost the whole sample and hence of density 8.7 mm^{-1}. Figure 9.4 shows examples of the networks of series 1, with fracture zones indicated. Also from this figure it is obvious that the density in the fracture area decreases as sample length increases.

Series 2 can be compared to, though not being, unit cells coupled parallel. In this case fracture in the weakest cell does not imply global failure, since the forces can redistribute to new paths where the material is stronger. Because of this, Weibull theory is no longer applicable. Instead, one may as a first approximation expect that the maximum stress remains at an almost constant level as the sample height increases. The computational result is shown in Figure 9.5 and Table 9.1.

Series 3 is a combination of the former two, and the results should be somewhere between the extreme cases of series 1 and series 2.

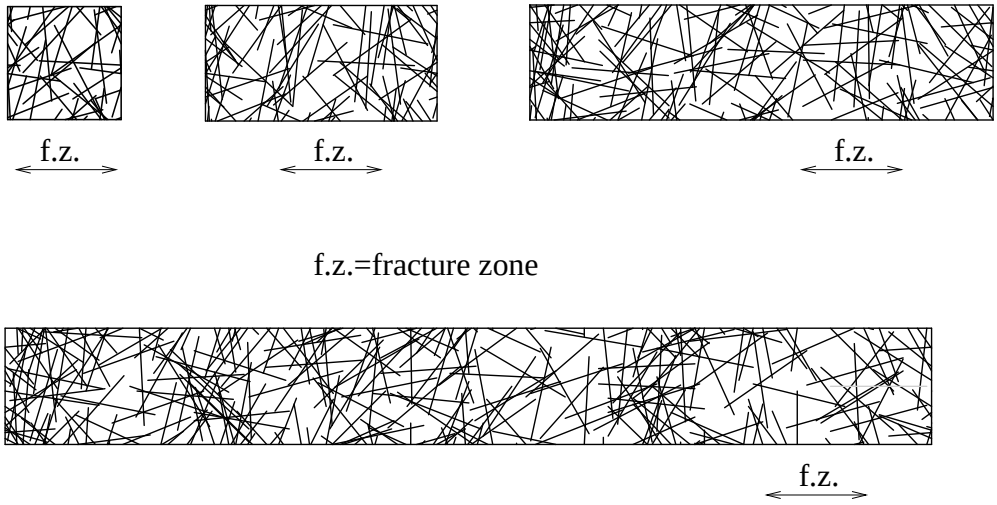

Figure 9.4: *Examples of networks and fracture zones from series 1.*

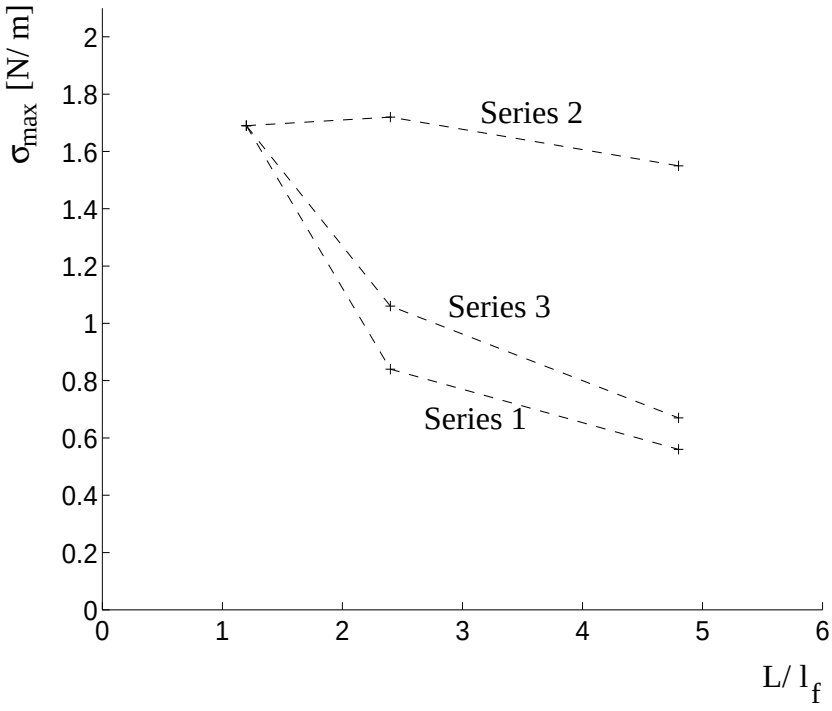

Figure 9.5: *Maximum stress against L/l_f for series 1, 2 and 3.*

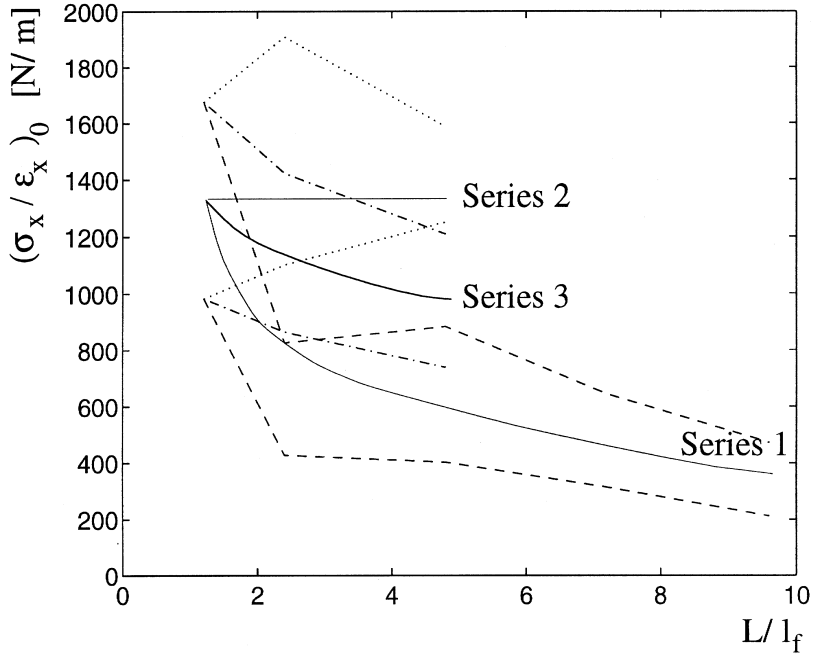

Figure 9.6: *Normalized initial stiffness against* L/l_f.

The maximum stress against the characteristic L/l_f-ratios of the different series are shown in Figure 9.5. In series 2 the maximum stress remains rather constant, and in series 3 it decreases, but not as strongly as in series 1. In Table 9.1, mean values and coefficients of variation for the calculated strengths as well as the other parameters studied with respect to sample size are given.

In Figure 9.6 the initial stiffness is plotted against L/l_f for the three series. The heavy lines are estimations made within the 90% confidence interval, the limits of which are also indicated in the figure. As far as strength is concerned, the weakest part of the material is decisive, and it is then obvious to expect a dependence on heterogeneity and sample size. The initial stiffness, on the other hand, is an integrated measure of the properties of the whole sample. As discussed in Section 7.1, the resulting global stiffness in a serial coupling is, despite this, dependent on variations in stiffness in a sample, since a weak part weakens the structure more than a stiff part stiffens it. As expected from this, the serial coupling of Series 1 shows a pronounced decrease in initial stiffness as the sample length increases. For series 2 the initial stiffness keeps constant, as is expected in a parallel coupling. Series 3 shows a moderate decrease, though much more obvious than that of Figure 7.6. It seems that the density is here low enough to make the effect of heterogeneity significant.

Another interesting property of a network is the fracture energy, see Section 8.3 for definition. The fracture energies G_f for the different series are plotted against L/l_f in Figure 9.7. The heavy lines are estimations made within the 90% confidence interval, as in Figure 9.6. For series 1, G_f is decreasing as L/l_f increases, although

not as strongly as is the case of the maximum stress. This means that the elongation of the fracture zone before complete fracture increases as L/l_f increases, as could be expected when the network density is decreasing. For series 2 both the maximum stress and G_f are approximately constant, which means that the elongation of the fracture zone is also approximately constant. The curve of series 3 is as usual situated between the two extreme cases. The fracture energy G_f shown in Figure 9.7 corresponds to the localized fracture dissipation. The part of the fracture energy corresponding to the pre-fracture distributed dissipation is almost negligible in this case. This result, though, is not estimated to be general. Instead a very different result might be obtained if a network with, for instance, other properties of connections is analysed.

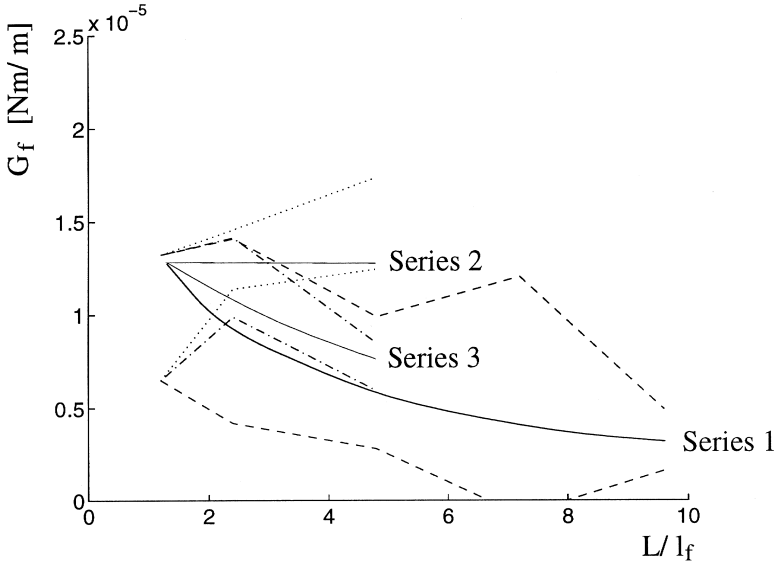

Figure 9.7: *Fracture energy against L/l_f.*

Figure 9.8 shows examples of networks and locations of the fractured connections for the three sample sizes of series 3. As indicated before, it is seen from the figure that the fracture process zone is of the same order of size as the fibre length. Hence, in the smallest network in which $L/l_f = 1.2$, one cannot distinguish a localized fracture zone since the entire area under observation represents a fracture zone. If one wishes to study localization phenomena, the dimension of the square studied should therefore be well over one fibre length; twice the fibre length will be used in the following.

The final conclusion is that the results of a fracture simulation of a heterogeneous material must always be considered in connection with the size and shape of the sample. The phenomenon of sample-size dependence cannot be avoided in either experiments or simulations.

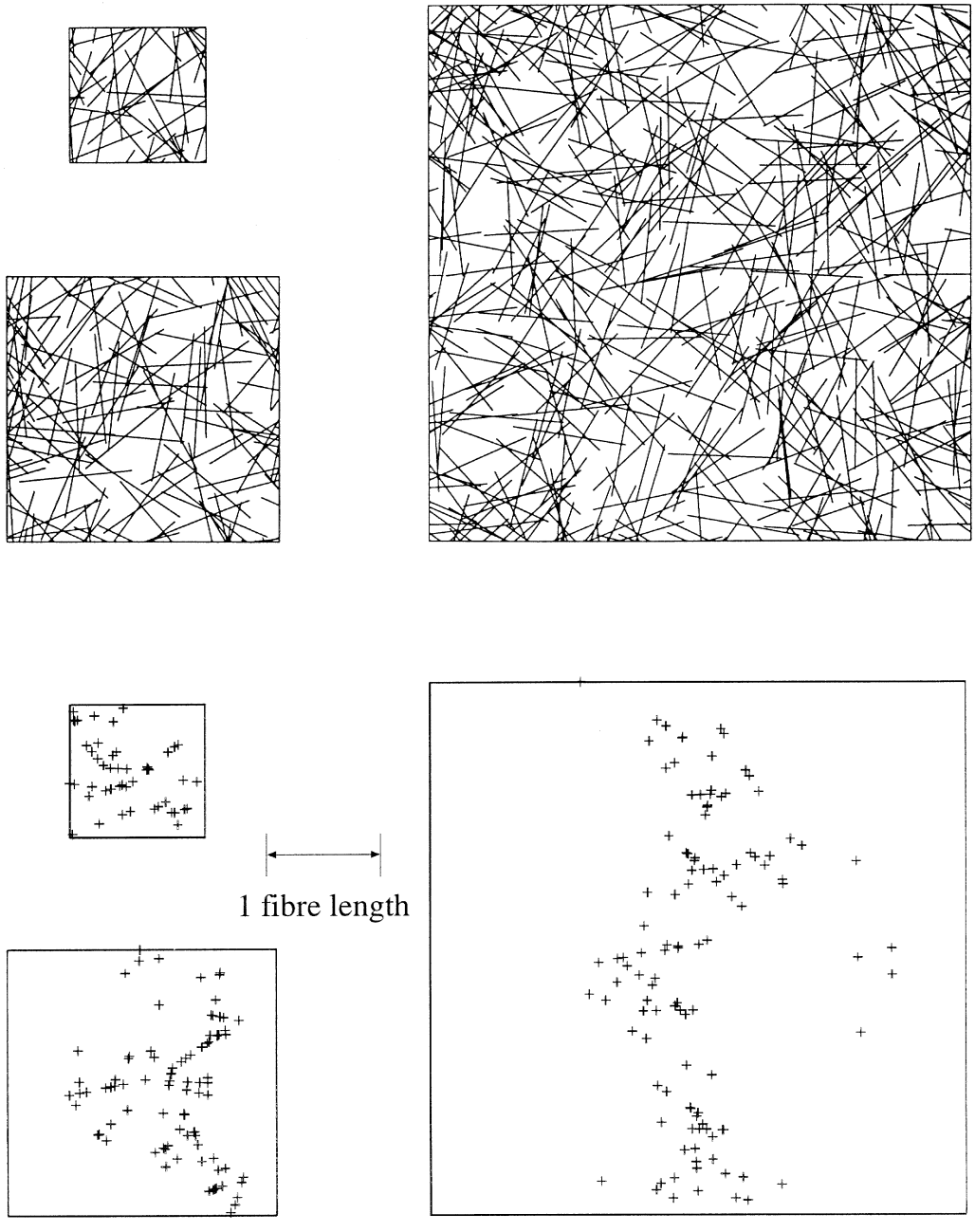

Figure 9.8: *Networks and locations of fractured connections.*

Table 9.1: *Average and coefficient of variation, (c.o.v.), of* $F_x/(E_f L_y l_f \epsilon_x)$, σ_{max} *and* G_f *versus sample size.*

$L_x L_y / l_f^2$	$(\sigma_x/\epsilon_x)_0$ [N/m]		σ_{max} [N/m]		G_f [Nm/m]	
	average	c.o.v.	average	c.o.v.	average	c.o.v.
series 1						
1.2×1.2	1300	0.50	1.70	0.34	$0.99 \cdot 10^{-5}$	0.46
2.4×1.2	630	0.61	0.84	0.58	$0.91 \cdot 10^{-5}$	0.74
4.8×1.2	640	0.72	0.56	0.55	$0.63 \cdot 10^{-5}$	0.76
7.2×1.2	480	0.66	0.30	0.71	$0.56 \cdot 10^{-5}$	1.55
9.6×1.2	340	0.73	0.20	0.64	$0.33 \cdot 10^{-5}$	0.69
series 2						
1.2×1.2	1300	0.5	1.70	0.34	$0.99 \cdot 10^{-5}$	0.46
1.2×2.4	1500	0.52	1.72	0.19	$1.30 \cdot 10^{-5}$	0.17
1.2×4.8	1400	0.23	1.55	0.30	$1.49 \cdot 10^{-5}$	0.23
series 3						
1.2×1.2	1300	0.5	1.70	0.34	$0.99 \cdot 10^{-5}$	0.46
2.4×2.4	1100	0.47	1.06	0.13	$1.20 \cdot 10^{-5}$	0.24
4.8×4.8	970	0.47	0.67	0.25	$0.72 \cdot 10^{-5}$	0.24

9.2. Fracture of an example network

The basic fracture example network of Section 8.1, shown in Figure 9.9, will be used to show the character of different kinds of network failure: only failure of connections allowed, only failure of fibre segments, and simultaneous failure of connections and fibres.

Figure 9.10 shows the progression of network failure for the case of failure allowed only in connections. This mode of failure is accomplished either by giving the beam elements a much higher strength, or by only evaluating degree of utilization in the connection elements. The three columns show active structure, zero-stress fibre segments and fractured connections respectively, initially and after 12, 50, 75 and 96 connections have failed. Final failure occurs after the 97th connection has failed, and after this step the entire structure is stress-less. The corresponding $\sigma_x\epsilon_x$-curve is given in Figure 9.11, with indications of which points on the curve correspond to the states shown in Figure 9.10.

The corresponding results from the case of beam failure only are shown in Figures 9.12 and 9.13.

Finally, Figure 9.14 shows the $\sigma_x\epsilon_x$-curve for the case when both strength of beams and connections are according to Section 8.1, and both degrees of utilization are evaluated. For the strength parameters chosen here, almost only connections fail; of the 88 failed elements at complete fracture only 5 are beam elements. The domination of connection failure reflects the performance of a dry-shaped material. If the strength parameters for the connections were adjusted to reflect the strength of connections of a wet-shaped material like paper, occurrence of beam failure, i.e. fibre failure, would become more frequent.

With respect to strength, Figures 9.11 and 9.14 show that prevention of beam failure does not give any increase at all for the present network. Comparing Figures 9.14 and 9.13, it can be seen that prevention of connection failure gave approximately 60 % increase in strength. For a real network, connection failures can be avoided by use of an adhesive aerosol, as discussed in Chapter 1.

The character of the fracture process is somewhat different if connection or beam failure is considered. When a beam has failed a load-bearing path has been completely destroyed, whereas when a connection fails load may still be transmitted. There is more of a pull-out fracture phenomenon when connections fail; only when a fibre end has been completely pulled out of the structure is the load-bearing path entirely destroyed. This explains why it takes fewer element failures to reach complete failure when only beam failure is considered. The curves of Figures 9.11 and 9.14 are similar, since both show fracture when connection failures are dominant.

To give a numerical example and an illustration to (8.12), which states that the fracture energy w^n of a network is larger than the sum of the fracture energies of the failed components, w^{fc}, the network with only connection failures is considered. For this network w^n is $7.2 \cdot 10^{-8}$ Nm, while the sum of the fracture energies of the failed connections is only $0.6 \cdot 10^{-8}$ Nm. The difference between the fracture energy of a material and the sum of the fracture energies of the failing micro-components of the

material, even when there is no plastic dissipation, is in principle quite important and can also be of significant magnitude. In the present example less than 10% of the total energy corresponds to fracture energy of the failing components. The other part, more than 90%, can be referred to heterogeneity of the material. This major part of the fracture energy can be regarded as a result of instabilities within the micro-structure of the material.

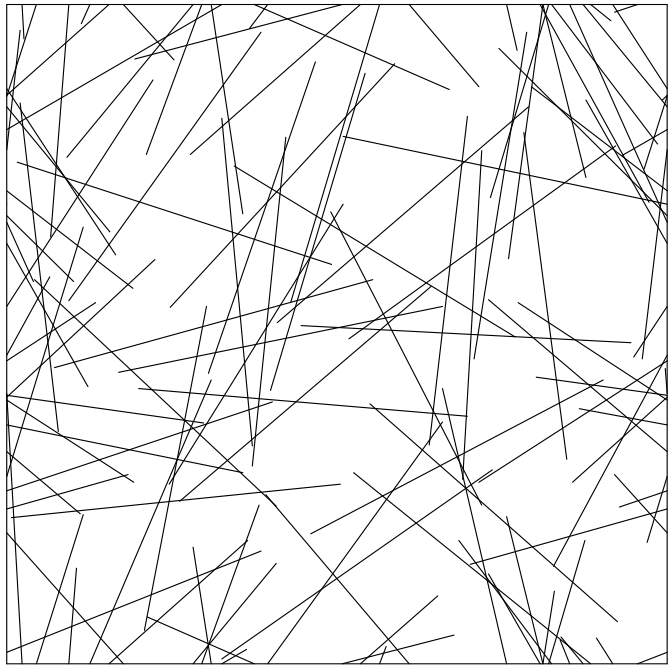

Figure 9.9: *Basic fracture example network.*

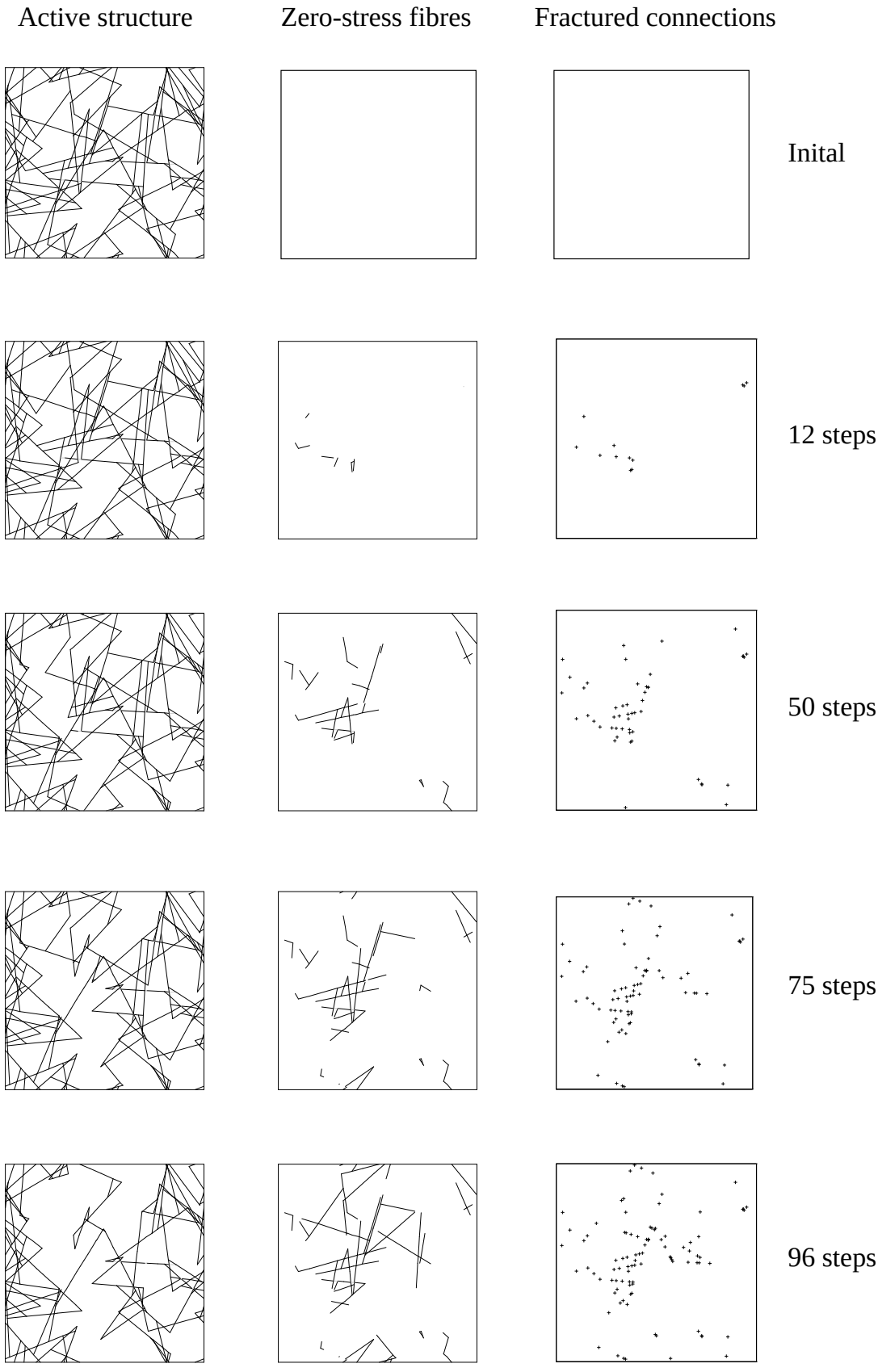

Figure 9.10: *Fracture process of example network, only fracture of connections considered, i.e. fracture of fibres prevented.*

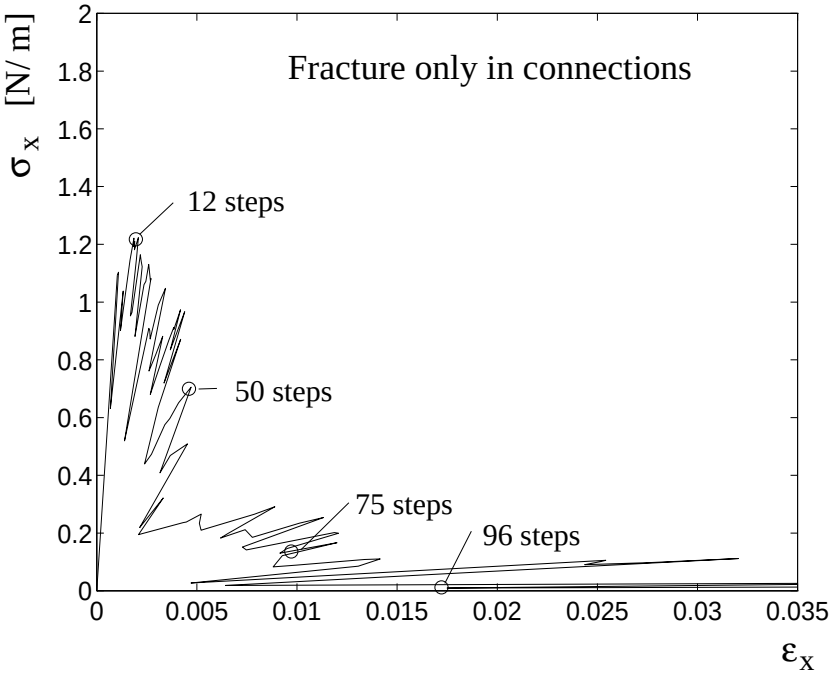

Figure 9.11: *Stress-strain relationship of example network, only fracture of connections considered, i.e. fracture of fibres prevented.*

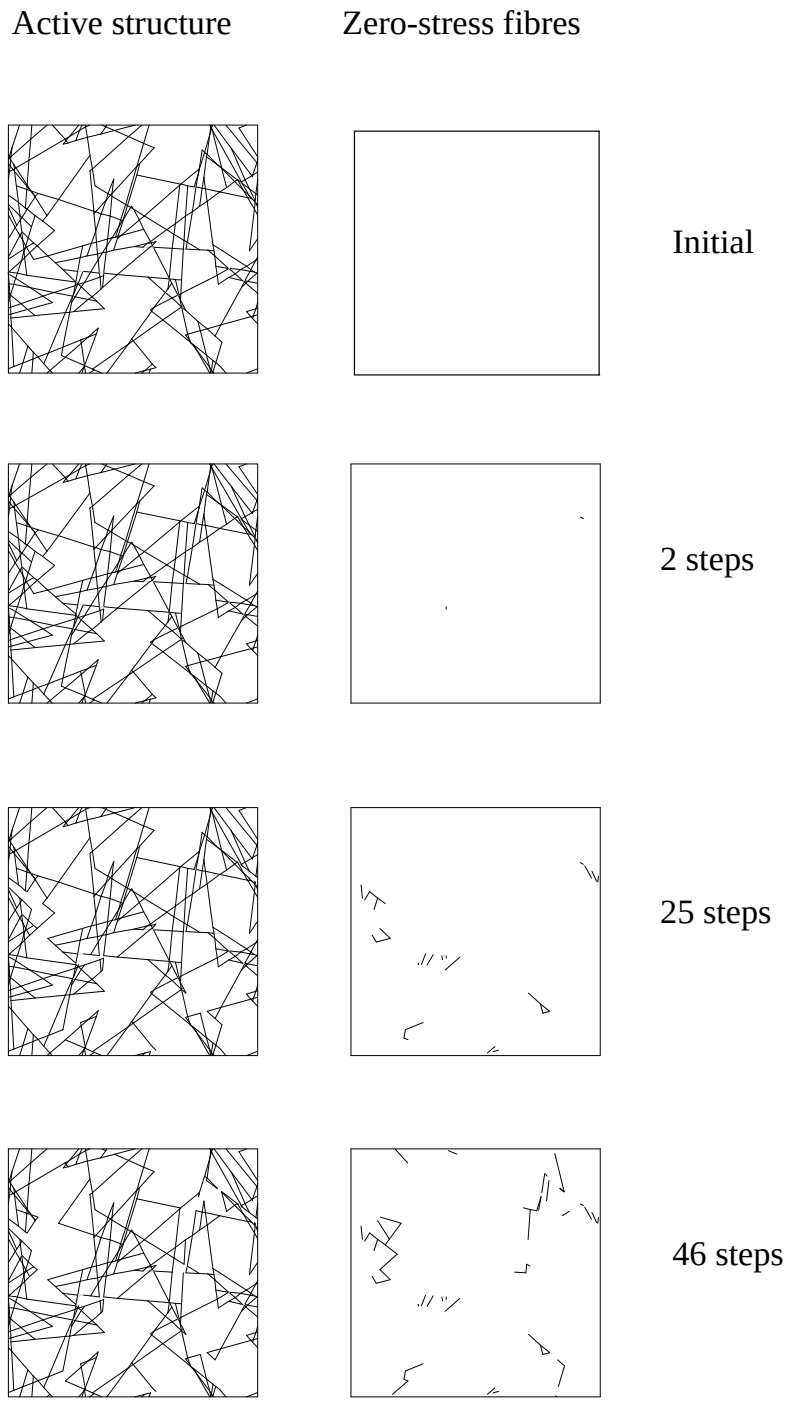

Figure 9.12: *Fracture process of example network, only fracture of fibres considered, i.e. fracture of connections prevented.*

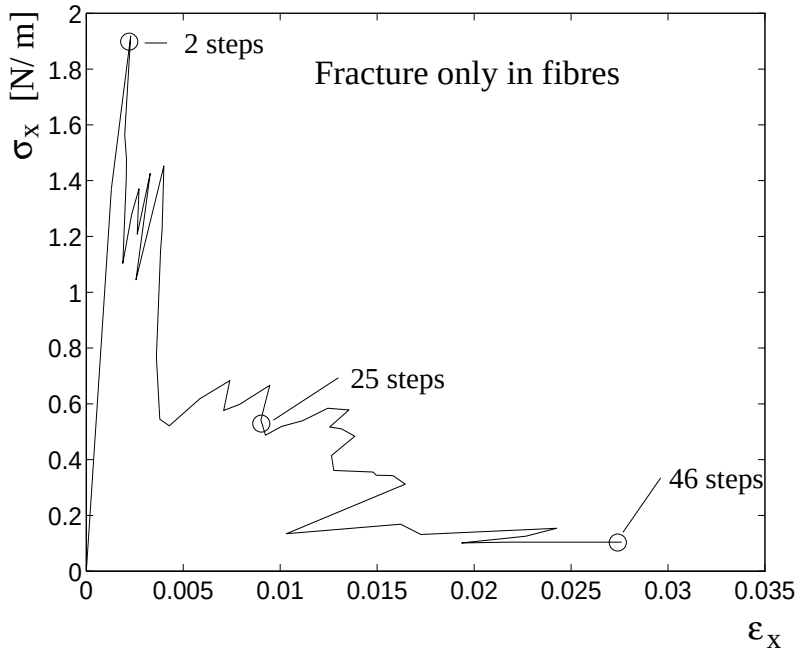

Figure 9.13: *Stress-strain relationship of example network, only fracture of fibres considered, i.e. fracture of connections prevented.*

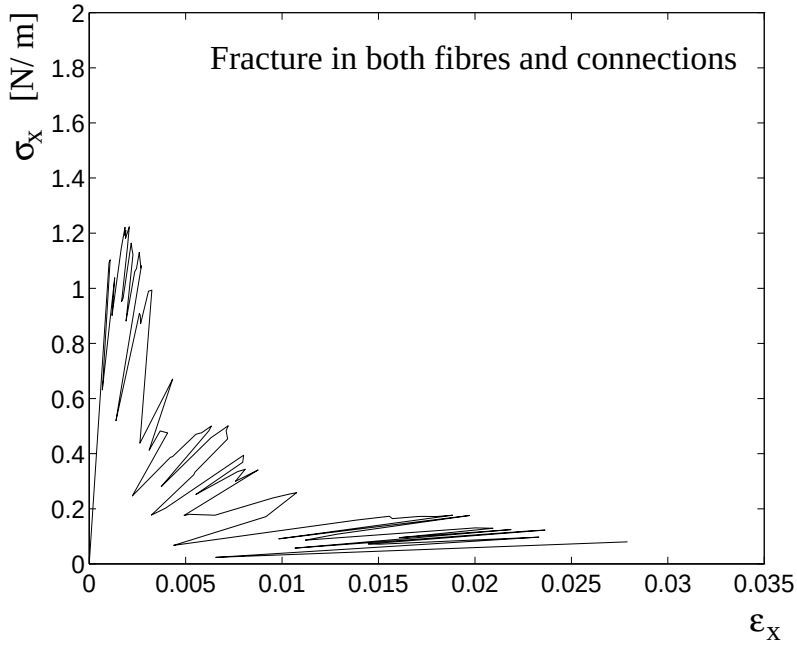

Figure 9.14: *Stress-strain relationship of example network, both fracture of connections and of fibres considered.*

9.3. Influence of properties of connections

In this section it is assumed that only connections fail, that is, the fibres are assumed to be strong enough to avoid fibre failure. Under these circumstances the influence of the properties of the connections on the fracture behaviour is studied. The connection properties taken into consideration are stiffness, strength and degree of ductility, the last property being quantified by n_s, number of slips before complete failure, and by β_1 and β_2, see Figure 3.4.

Starting out by considering one single linear elastic spring, the effect of changing spring properties can be seen from Figure 9.15. In *a)* two springs of equal stiffness but different strength are compared, and in *b)* the springs are equal in strength but differ in stiffness. From the $F - \Delta u$-relationships it can be seen that if the spring strength F is doubled and the stiffness k is kept constant, both the ultimate force and ultimate extension Δu are doubled, while the fracture energy, w, increases four times. If instead the spring stiffness is doubled and the strength is kept constant, as in *b*), the ultimate force does not change but both ultimate extension and fracture energy reach only half their original values.

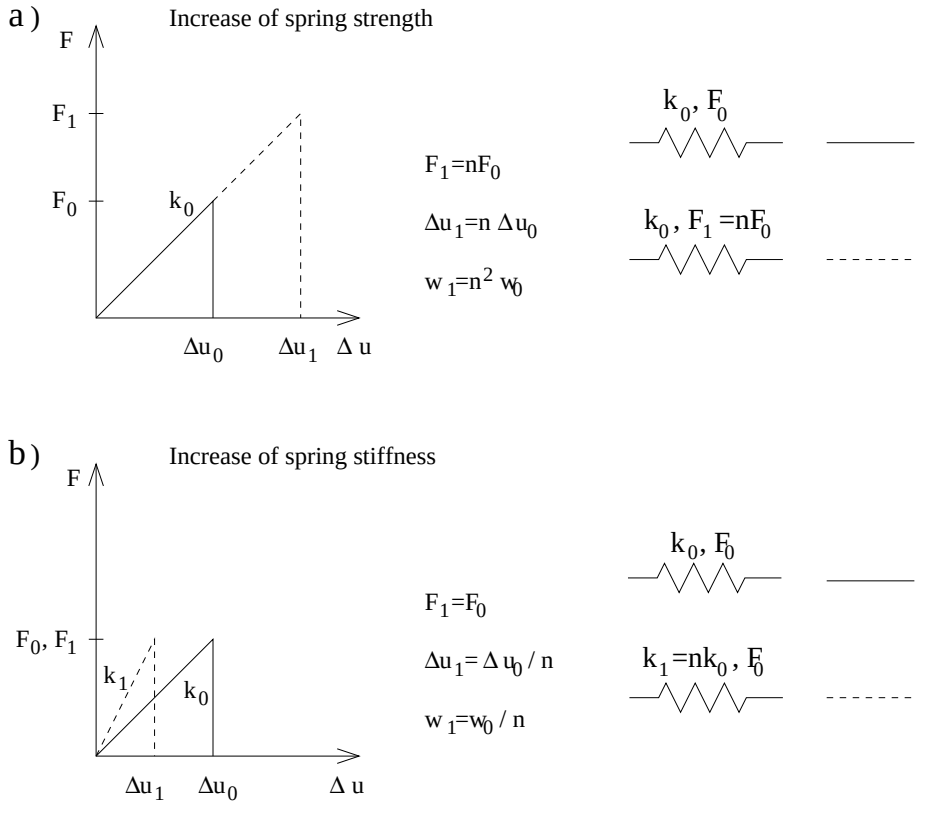

Figure 9.15: *a) Effect of modified spring strength. b) Effect of modified spring stiffness.*

When a network is considered instead of a single spring, the conclusions from

the spring case are directly applicable to the case of change of strength, provided that only connections fail. This is illustrated by Figure 9.16, where the stress-strain relationship of the example network of the previous section is given, together with the corresponding curve for the same network when the strength of the connections has been doubled, dashed in the diagram. Doubling the strength of the connections here means doubling of both ultimate force and ultimate moment. As is expected from the spring case, the ultimate stress as well as the ultimate strain are twice the value of the example network, and the fracture energy is hence increased by a factor of four. When only fracture of connections is considered, and the strength of

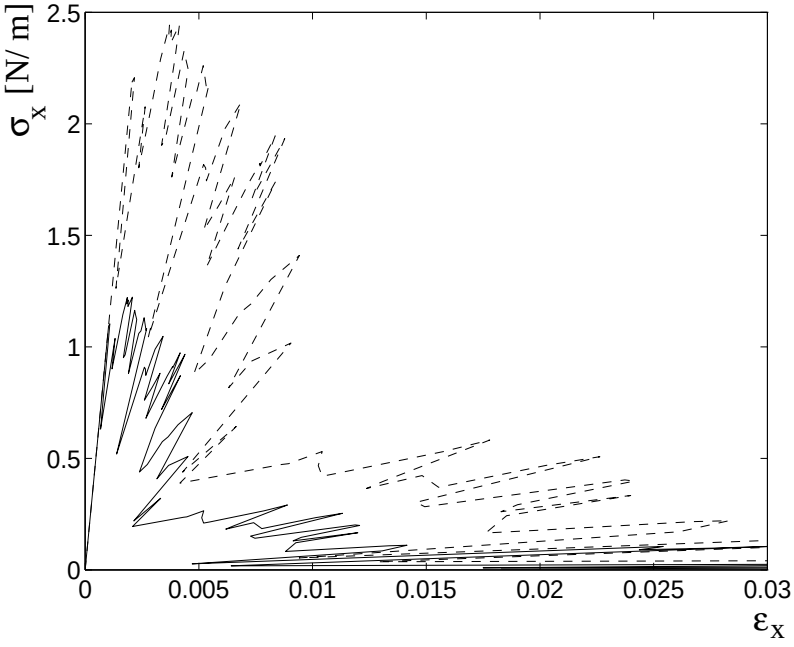

Figure 9.16: *Change of stress-strain relationship for fracture example network when connection strength is doubled.*

the connections is modified, the fracture behaviour of the new network can thus be obtained from the simple relations of Figure 9.15a. From these relations it is also found that the intrinsic or characteristic length parameter of the material, l_{ch}, see (8.15), is not affected by the connection strength.

If on the other hand we choose to modify the spring stiffness, the situation is more complicated. This is because the relation between connection and beam stiffnesses influences the fracture behaviour. To get an implication of what effects to expect, simple spring systems are studied once again, see Figure 9.17, which shows couplings of springs, spring 1 symbolizing connections and spring 2 symbolizing beams. The ultimate force of spring 1 is $k\Delta u$, where k and Δu are constants. The effect of decreasing the stiffness of spring 1 while keeping its ultimate force constant at $k\Delta u$ is studied. Serial and parallel couplings are compared. The following equations

are obtained for resultant stiffness k_{tot}, ultimate force, F_{tot} and ultimate extension Δu_{tot}, by analysing the situation when spring 1 reaches its ultimate force:

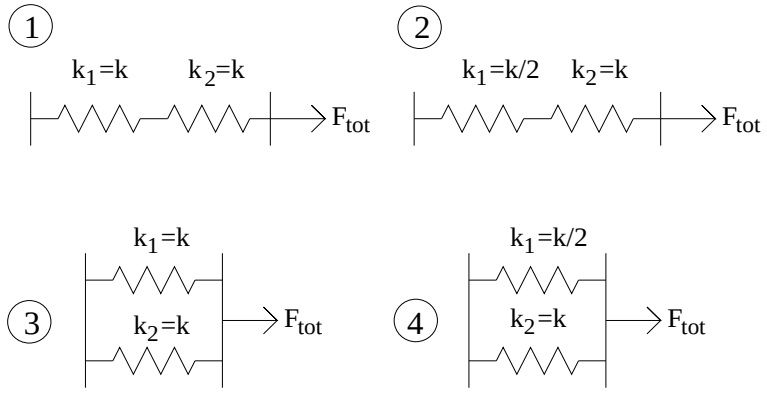

Figure 9.17: *Spring couplings showing effect of decrease in stiffness in one of the springs.*

Spring coupling 1:

$$k_{tot} = \frac{1}{\frac{1}{k} + \frac{1}{k}} = \frac{k}{2}$$

$$F_{tot} = F_1 = k\Delta u$$

$$\Delta u_{tot} = \frac{F_{tot}}{k_{tot}} = \frac{k\Delta u}{k/2} = 2\Delta u$$

Spring coupling 2:

$$k_{tot} = \frac{1}{\frac{2}{k} + \frac{1}{k}} = \frac{k}{3}$$

$$F_{tot} = F_1 = k\Delta u$$

$$\Delta u_{tot} = \frac{F_{tot}}{k_{tot}} = \frac{k\Delta u}{k/3} = 3\Delta u$$

Spring coupling 3:

$$k_{tot} = k + k = 2k$$

$$\Delta u_{tot} = \Delta u_1 = \frac{F_1}{k_1} = \frac{k\Delta u}{k} = \Delta u$$

$$F_{tot} = F_1 + F_2 = k\Delta u + k\Delta u = 2k\Delta u$$

Spring coupling 4:

$$k_{tot} = \frac{k}{2} + k = \frac{3k}{2}$$

$$\Delta u_{tot} = \Delta u_1 = \frac{F_1}{k_1} = \frac{k\Delta u}{k/2} = 2\Delta u$$

$$F_{tot} = F_1 + F_2 = k\Delta u + 2k\Delta u = 3k\Delta u$$

A weaker spring 1, as expected, implies a lower value of k_{tot} for both serial and parallel couplings. In a serial coupling a weaker spring 1 implies the same ultimate load and increased ultimate extension, and in a parallel coupling it implies an increase in both ultimate load and extension. If we think of a network as an intermediate between connections and beams coupled in series and parallel, we thus expect a reduction of the connection stiffness to give a decrease in initial stiffness and increase in ultimate stress, ultimate strain and fracture energy. This is also what simulations show.

Simulations have been made on the basic fracture example network geometry of Section 8.1, with spring stiffnesses multiplied by 0.01, 0.1, 1, 10 and 100. All other parameters, including the spring strength parameters, are kept at constant values according to Table 8.1. The studied variation in spring stiffness is about the same as that which gives strong influence on the initial stiffness of the network according to Figure 7.7. Spring stiffness k here includes all three stiffness values k_x, k_y and k_ϕ, which are all multiplied by the same constant. Due to big differences in magnitudes it is not possible to show all the five curves in the same diagram. Figure 9.18 shows the stress-strain relationship of the example network, and the two networks with reduced spring stiffnesses. It is clear that the initial stiffness decreases and ultimate stress and strain increases as the spring stiffness decreases. Figure 9.19 shows the corresponding relationships for the example network and the two networks with higher stiffness values. The curves for $10k$ and $100k$ are partly interfering and difficult to distinguish. Figures 9.20 and 9.21 show the maximum stress and fracture energies against k/k^0, k denoting stiffness of connections in the network studied and k^0 being connection stiffness of the fracture example network.

In Table 9.2 the results are given numerically, also for the initial stiffness, $(\sigma_x/\epsilon_x)_0$, and the characteristic length, l_{ch}. It should be noted that the computational results for the various k/k_0 are obtained from one single network geometry.

Table 9.2: *Material property parameters against stiffness of connections.*

k/k_0	$(\sigma_x/\epsilon_x)_0$ [N/m]	σ_{max} [N/m]	G_f [Nm/m]	l_{ch} [m]
0.01	110	6.56	$210 \cdot 10^{-5}$	$5.4 \cdot 10^{-3}$
0.1	430	3.28	$30 \cdot 10^{-5}$	$12 \cdot 10^{-3}$
1	1100	1.22	$1.8 \cdot 10^{-5}$	$13 \cdot 10^{-3}$
10	1600	0.61	$0.36 \cdot 10^{-5}$	$16 \cdot 10^{-3}$
100	1800	0.42	$0.30 \cdot 10^{-5}$	$31 \cdot 10^{-3}$

Even though the effect of changing the spring stiffness seems very big from the diagrams it is not as strong as the effect of changing the strength. In the stiffness case we get a factor of increase in ultimate stress of approximately 16 when stiffness is decreased with a factor 10000; in the case of change of strength there is direct proportionality between the increase in spring strength and network ultimate stress.

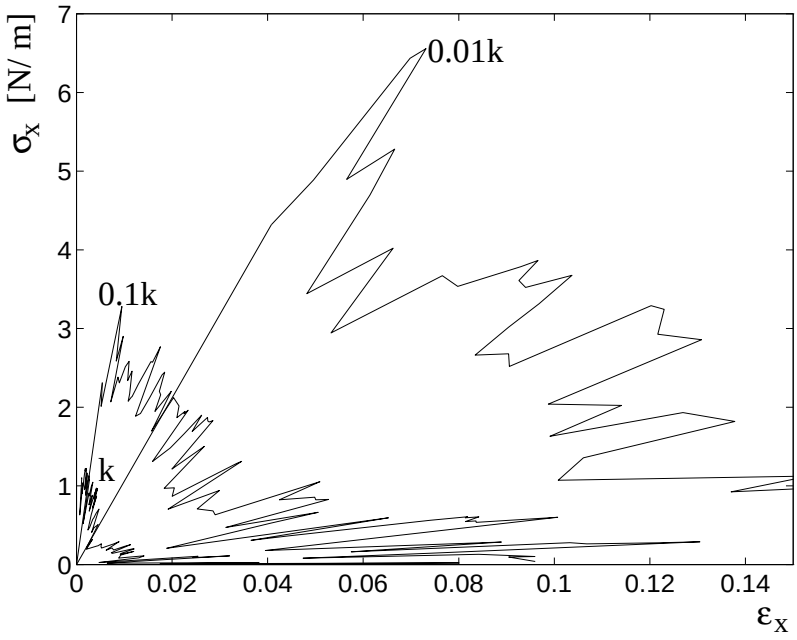

Figure 9.18: *Stress-strain relationship of example network when connection stiffness is decreased.*

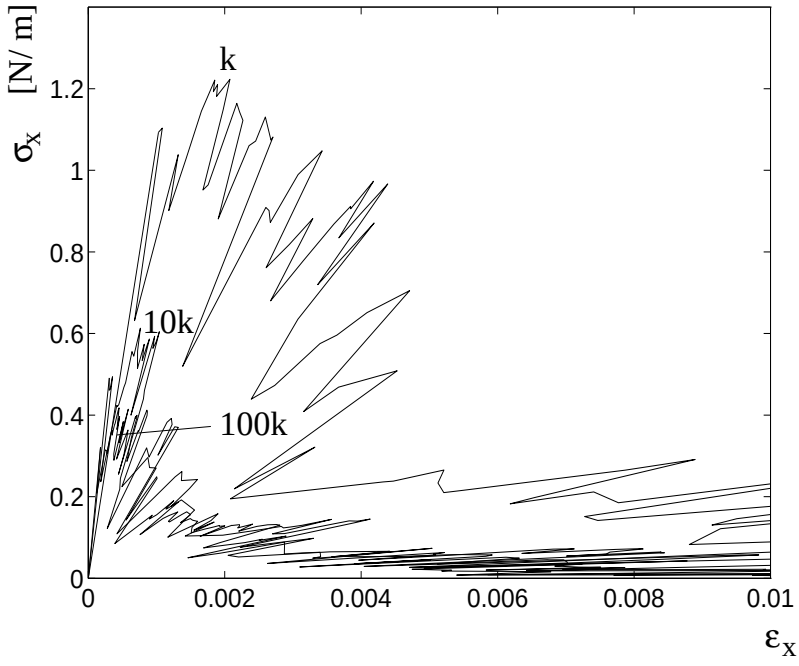

Figure 9.19: *Stress-strain relationship of example network when connection stiffness is increased.*

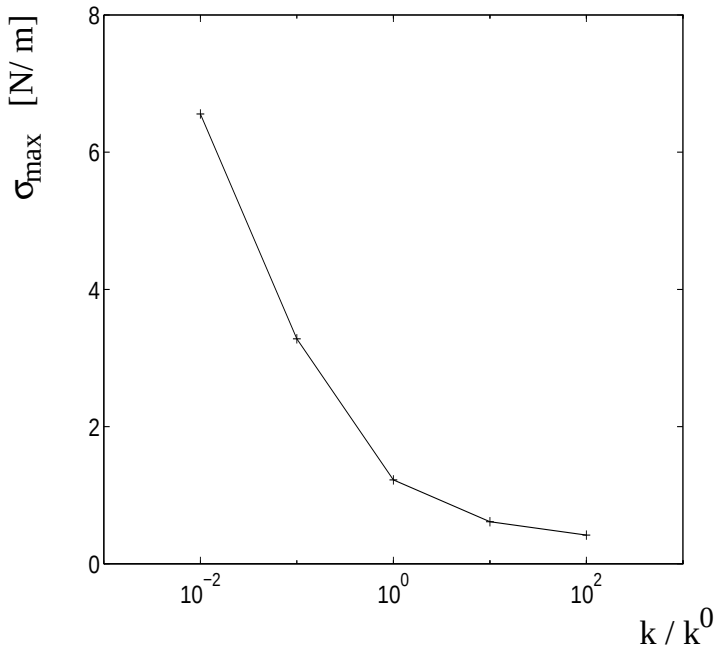

Figure 9.20: *Maximum stress against* k/k^0.

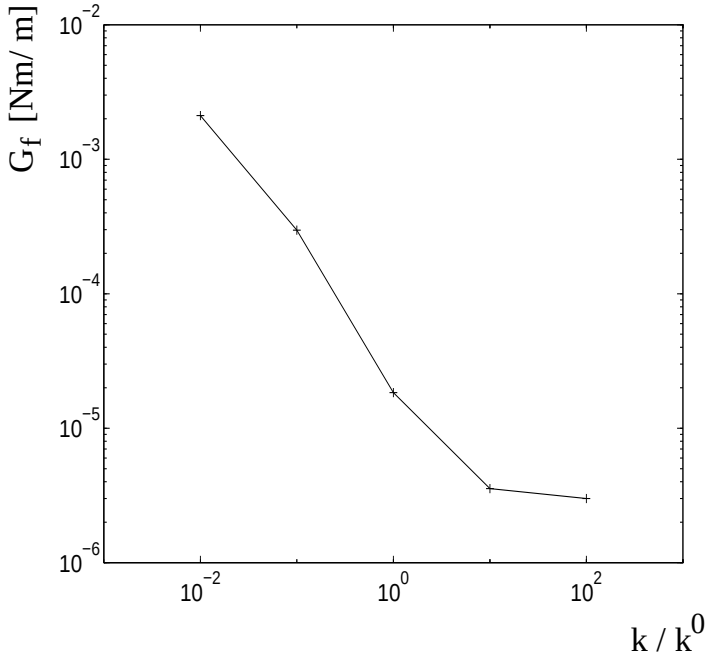

Figure 9.21: *Fracture energy against* k/k^0.

Simulations have also been made in order to investigate the influence of ductility of connections on global fracture behaviour. The stick-slip behaviour of the connections is defined in Figure 3.4. The parameters used were reduction in stiffness between two slips $\beta_1 = 0.5$, and reduction in strength between two slips $\beta_2 = 1.0$. The number of slips before complete failure, n_s, investigated were 1, 2 and 5. The network density is 20 mm^{-1} and the rest of the input parameters are according to Table 8.1. As many as five slips before final failure of a connection may seem a lot, but the relative displacement of two fibres in a connection is here still at the microscopic level. The effect of fibres slipping and forming new connections in a new geometric configuration remains to be accounted for.

Two simulations were made for each value of n_s. In order to speed up the calculations, more than one connection was modified in each step for the cases of $n_s = 2$ and 5. Figure 9.22 illustrates the effect of this approximation, the first diagram showing the result for $n_s = 2$ when only one connection is modified in every step, and the second the result when five connections are modified in each step. The details of the curve are changed, but the overall impression is much the same. For $n_s = 5$, ten connections were modified in each step.

If the results from all the simulations are plotted in the same diagram the curves interfere and make interpretation of the results difficult. In order to avoid this problem the average of the two curves in the different simulations was substituted by a hand-drawn simplified approximation. Figure 9.23 shows the two original curves as well as the approximated one in the same diagram, for the case of $n_s = 5$.

The result of the simulations is shown in Figure 9.24. It is clear that an increase in connection ductility has a remarkable effect on the global strength and fracture energy. This is because the greater ductility allows the degree of utlisation to become more evenly distributed over the network. The stiffness of a connection that is severely stressed is reduced, allowing other less stressed connections to take over part of the loading. Ideally, one could imagine a situation where every connection in the network reaches final failure at the same time, although this would cause a very abrupt failure. The ultimate stress and fracture energy against n_s are shown in Figures 9.25 and 9.26. In Table 9.3 also the results for initial stiffness and characteristic length are indicated.

Table 9.3: *Material property parameters against ductility of connections.*

n_s	$(\sigma_x/\epsilon_x)_0$ [N/m]	σ_{max} [N/m]	G_f [Nm/m]	l_{ch} [m]
1	25000	22	$6.8 \cdot 10^{-5}$	$3.5 \cdot 10^{-3}$
2	25000	30	$14 \cdot 10^{-5}$	$3.9 \cdot 10^{-3}$
5	25000	56	$120 \cdot 10^{-5}$	$9.6 \cdot 10^{-3}$

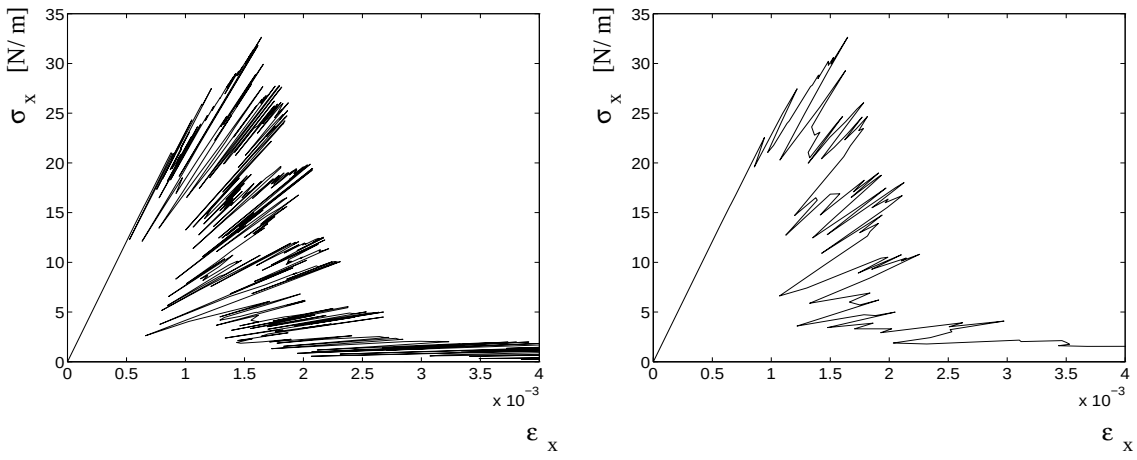

Figure 9.22: *Stress-strain relationship for the same network when 1 and 5 connections respectively have been removed in each step.*

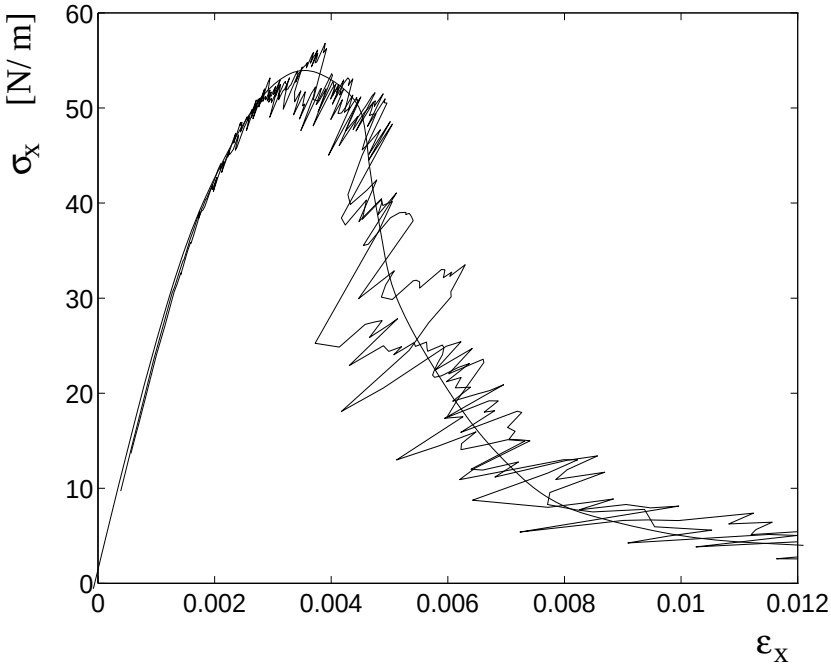

Figure 9.23: *Two stress-strain curves obtained from simulations together with the corresponding hand-drawn approximation.*

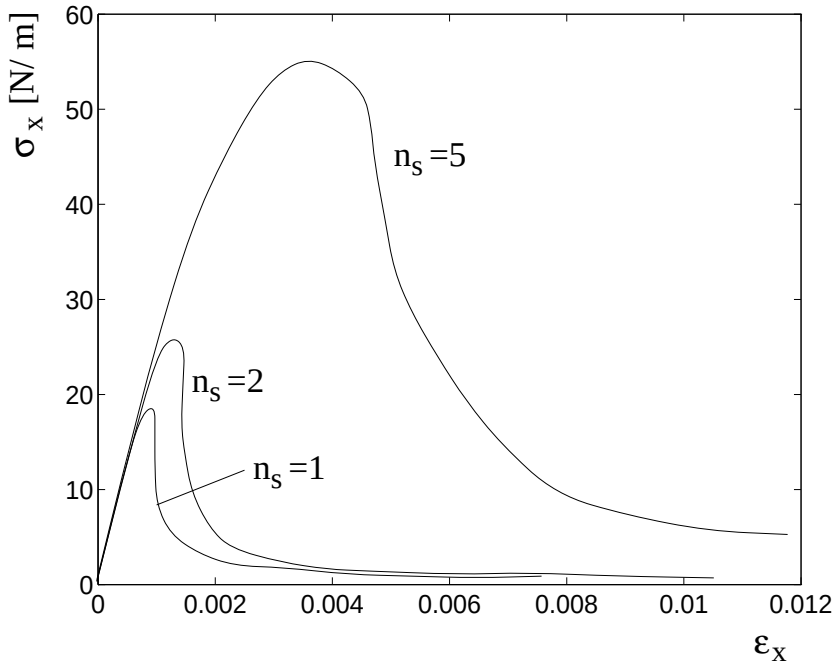

Figure 9.24: *Stress-strain relationships for $n_s = 1$,2 and 5.*

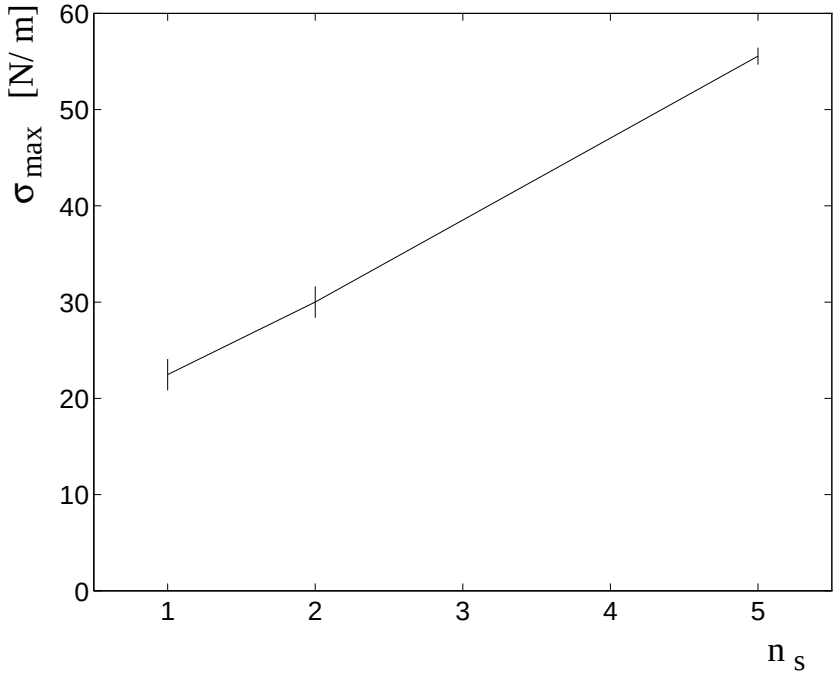

Figure 9.25: *Maximum stress against n_s.*

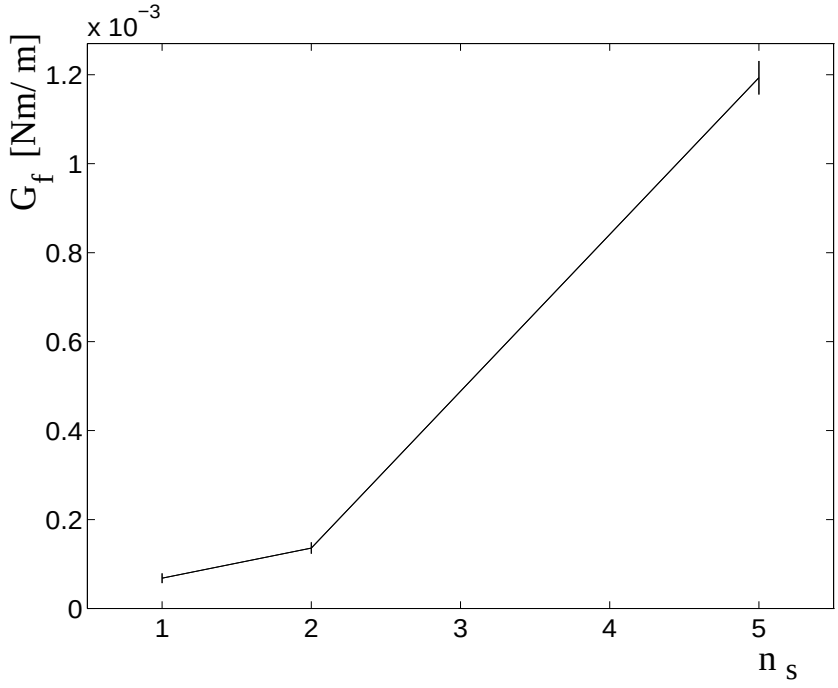

Figure 9.26: *Fracture energy against n_s.*

9.4. Influence of network density

The influence of network density on the fracture behaviour of a network has been examined by simulating a series of networks of density ρ= 8.7, 15 and 20 mm^{-1}. Connection failure is assumed, and the rest of the properties of the networks correspond to those of the fracture example network. Five simulations were made for each value of network density, and the average of the results is given in the following figures. The stress-strain relationships for the different densities are all given in Figure 9.27, despite big differences in both maximum stress and strain. To facilitate interpretation of the figure, hand-drawn approximations have been made, according to the principle given in the preceding section. As ρ increases, the networks become remarkably stronger, and also more brittle. The maximum stress and fracture energy, average and standard deviation, against ρ are given in Figures 9.28 and 9.29.

In [1], where the connections were assumed to be rigid, it was concluded that the strength of a network is proportional to Young's modulus of the network times the ultimate shear strain in a connection. From Figure 9.30 it is clear that the results of the present simulations agree with [1] in that the maximum stress of a network divided by the initial stiffness is almost exactly constant. If the connections are linear elastic, the ratio between fibre and connection stiffness is kept constant and failure is allowed to occur only in the connections, it is obvious that the strength will

be proportional also to the ultimate strain of the connections, see Figure 9.16. If the ultimate strain of the connections is increased by increasing n_s from 1 to 2 and 5 respectively, an increase in network strength is found again, though not proportional to the ultimate strain, see Figure 9.20.

In Table 9.4 the computational results for initial stiffness, strength, fracture energy and characteristic length are indicated numerically. It is interesting to note that the fairly moderate increase in density from 15 mm^{-1} to 20 mm^{-1} gives more than a two-fold increase in both stiffness, strength and fracture energy. In the region from 8.7 mm^{-1} to 15 mm^{-1} the effect on stiffness and strength is even stronger. The theoretical percolation density of the network is 5.7/2.0=2.9 mm^{-1}. Since the strength is low already at $\rho = 8.7$ mm^{-1}, the sensitivity in strength to density is probably very small in the region from the percolation point up to about 8 mm^{-1}.

From Table 9.4 it is also interesting to note that the coefficient of variation for the various properties is greater at low density. This is in agreement with the more heterogeneous character of the geometry of networks with low density. Also, the variation of the intrinsic material length parameter, l_{ch}, with density is consistent. The lowest value, 2.9 mm, at the highest density, $\rho = 20$ mm^{-1}, may correspond to the more brittle character of more homogeneous materials. The variation of l_{ch} with density seems to reflect also the general absolute size of the micro-structure of the material. Although the fibre length is the same for the different networks, the free fibre segment length as well as the size of the open areas, the 'pores', is much smaller at density $\rho = 20$ mm^{-1} than at $\rho = 8.7$ mm^{-1}.

Table 9.4: *Average and coefficient of variation, (c.o.v.), of material properties at different densities.*

ρ	$(\sigma_x/\epsilon_x)_0$ [N/m]		σ_{max} [N/m]		G_f [Nm/m]		l_{ch}
[mm^{-1}]	average	c.o.v.	average	c.o.v.	average	c.o.v.	[m]
8.7	1271	0.45	1.2	0.41	$1.35 \cdot 10^{-5}$	0.35	$11.9 \cdot 10^{-3}$
15	9126	0.19	8.4	0.19	$2.61 \cdot 10^{-5}$	0.18	$3.4 \cdot 10^{-3}$
20	23018	0.09	21.7	0.15	$6.01 \cdot 10^{-5}$	0.27	$2.9 \cdot 10^{-3}$

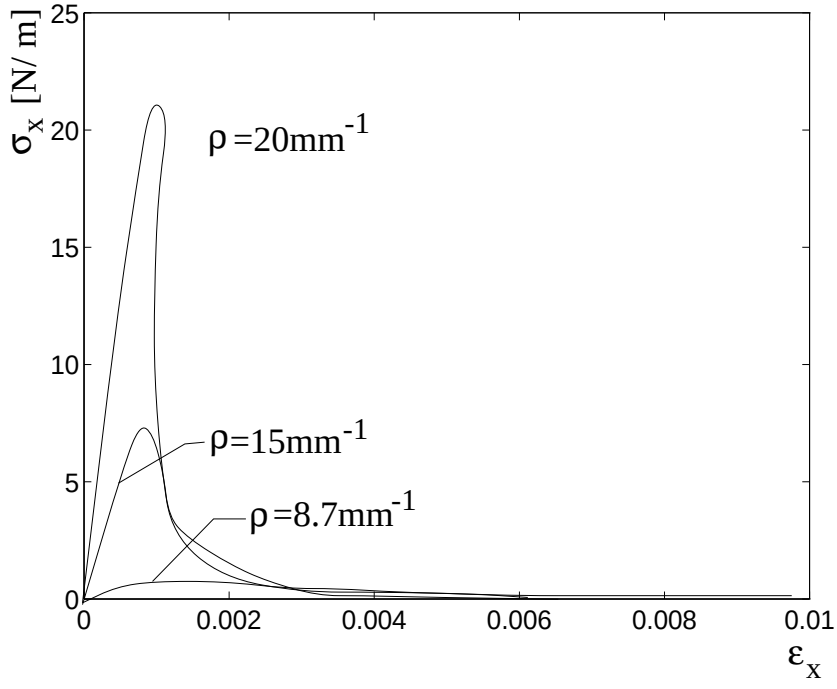

Figure 9.27: *Stress-strain relationships for different network densities.*

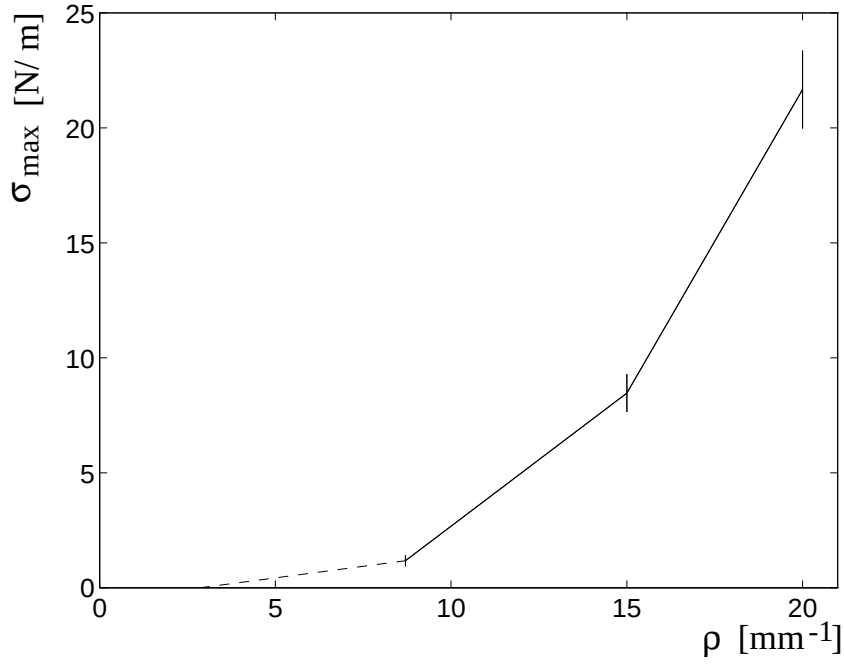

Figure 9.28: *Maximum stress against ρ.*

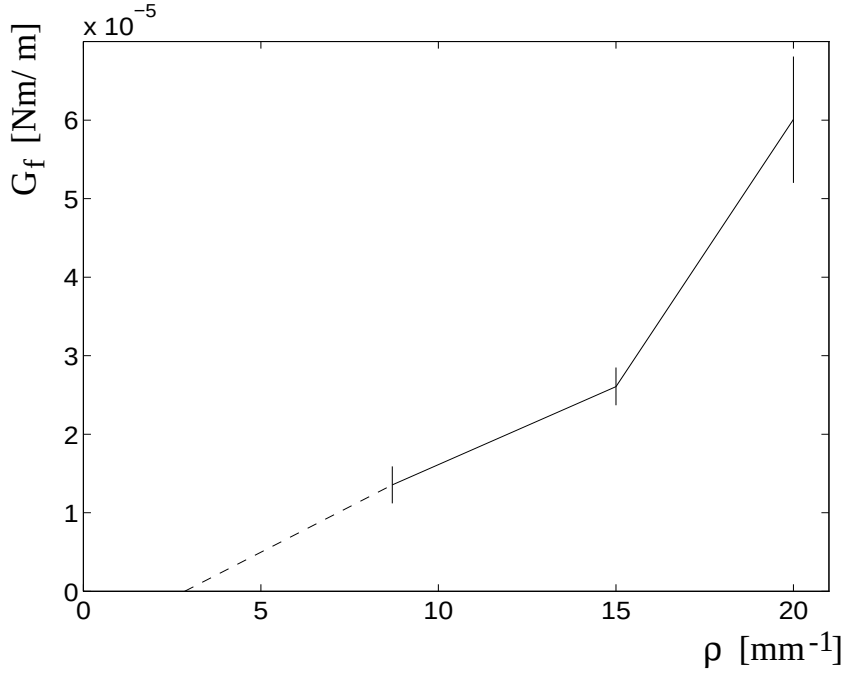

Figure 9.29: *Fracture energy against ρ.*

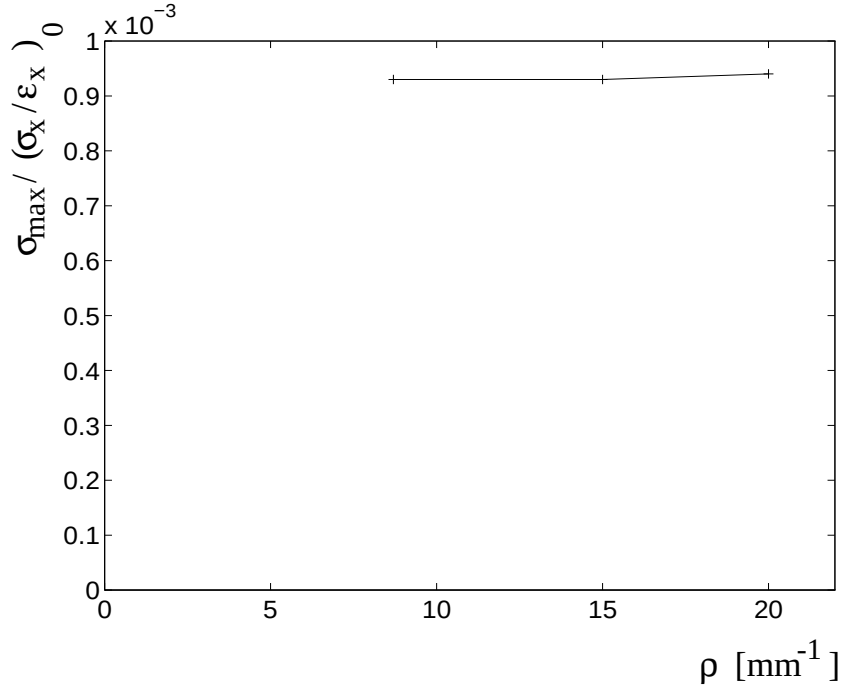

Figure 9.30: *Maximum stress divided by initial stiffness against ρ.*

9.5. Simulation of complex example network

This section shows an example of a simulation of a network of curled fibres of varying length. The length distribution of the fibres is the same as in Figure 7.26 in Section 7.6, approximately representing the length distribution of a CTMP pulp. The radius of curvature of the fibres is 1.4 mm. At a fibre crossing the probability of a connection is 0.4, and each connection shows a stick-slip peformance. The number of slips before complete failure is five, and at each slip the stiffness is reduced by a factor of 0.5, while the strength is unaffected. The orientation distribution is uniform. The network density is 22.1 mm^{-1}, giving an average free fibre segment length of 0.18 mm. This corresponds to a three-dimensional fibre fluff of density 80 kg/m^3, if it is assumed that the fibres are randomly distributed in space, see Appendix E. Only failure of connections is considered and ten connections are modified in each step.

The input parameters of the network are summarized in Table 9.5.

Table 9.5: *Input parameters of complex example network.*

Parameter	Value and unit
l_f	see Figure 7.26
κ	714 mm^{-1}
A_f	$2.5 \cdot 10^{-10}$ m^2
I_f	$0.2 \cdot 10^{-20}$ m^4
E_f	$35 \cdot 10^9$ Pa
σ_{ult}	100 MPa
τ_{ult}	50 MPa
$k_{x1} = k_{y1}$	8750 N/m
$k_{\phi 1}$	$2.8 \cdot 10^{-7}$ Nm/rad
F_{ult1}	$3.5 \cdot 10^{-3}$ N
M_{ult1}	$5.6 \cdot 10^{-9}$ Nm
n_s	5
β_1	0.5
β_2	1.0
L	4.2 mm
ρ	22.1 mm^{-1}
N_α	$\frac{1}{\pi}, \quad 0 < \alpha < \pi$
s	0.4
$d(x, y)$	1.0

Figure 9.31 shows an image of the network, which consists of 1800 active beam elements and 1005 connections, and the approximate active part is 70%. The number of degrees of freedom in the finite element model is 6366.

Figure 9.32 shows the stress-strain relationship of the network. There are 39

steps before maximum stress is reached, and after 95 steps the network has failed completely. $(\sigma_x/\epsilon_x)_0 = 1.29 \cdot 10^3$ N/m, $\sigma_{max} = 5.81$ N/m, $G_f = 20 \cdot 10^{-5}$ Nm/m and $l_{ch} = 7.6 \cdot 10^{-3}$ m.

Figure 9.33 shows the locations of the failed connections after 16, 39 70 and 95 steps. The first column indicates connections that have slipped at least once, the second indicates at least three slips and the third indicates five slips, which correspond to completely failed connections. It can be seen that connections slip all over the network, but the completely failed connections tend to be concentrated along a localized fracture zone. Maximum load is reached after 39 steps. At this point 210 connections have been modified and one has reached final failure. This first final failure corresponds to maximum load, and reveals that the stress-strain relationship begins to show a 'saw-tooth' behaviour. After 95 steps, 380 connections have been modified, and 53 have failed entirely.

Figure 9.34 shows in the first row the connections that fail during the part of the fracture where the stress is increasing, and in the second row the connections that fail while the stress decreases. Even though the side-length of the square, 4.2 mm, is only 1.5 times the distance between the end-points of the longest fibres, 2.8 mm, there is a weak tendency of localization.

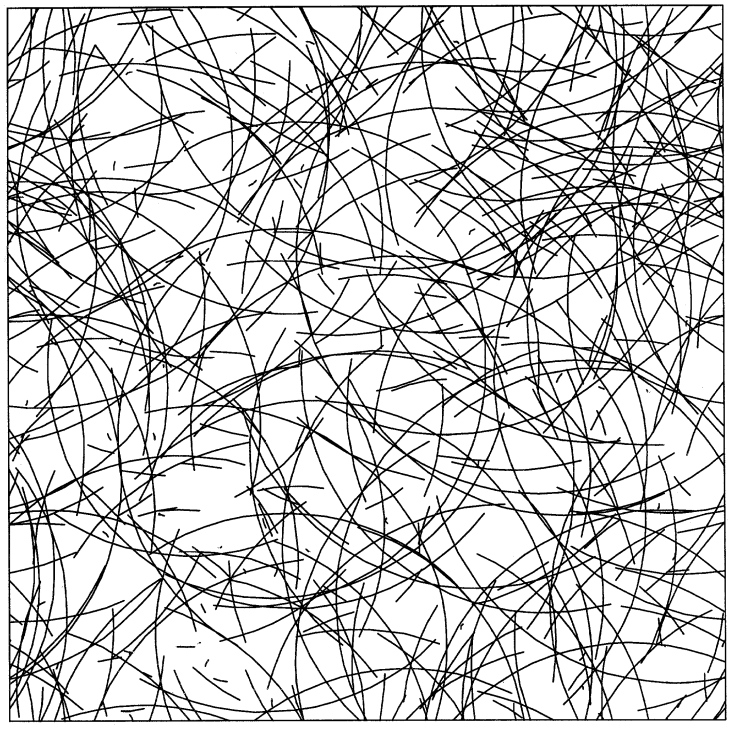

Figure 9.31: *Complex example network geometry.*

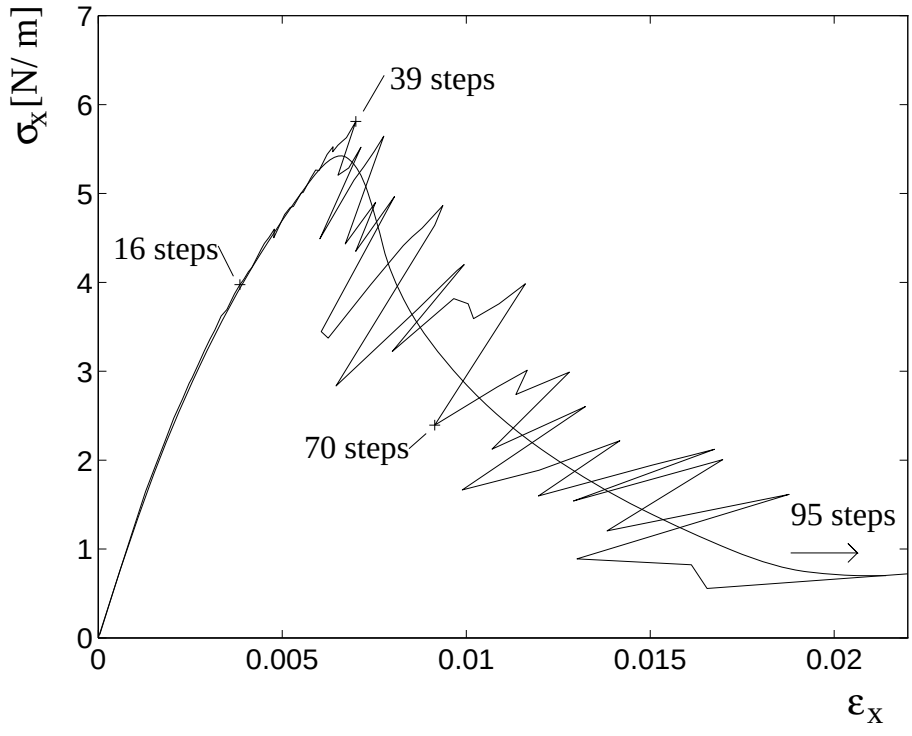

Figure 9.32: *Stress-strain relationship of complex example network.*

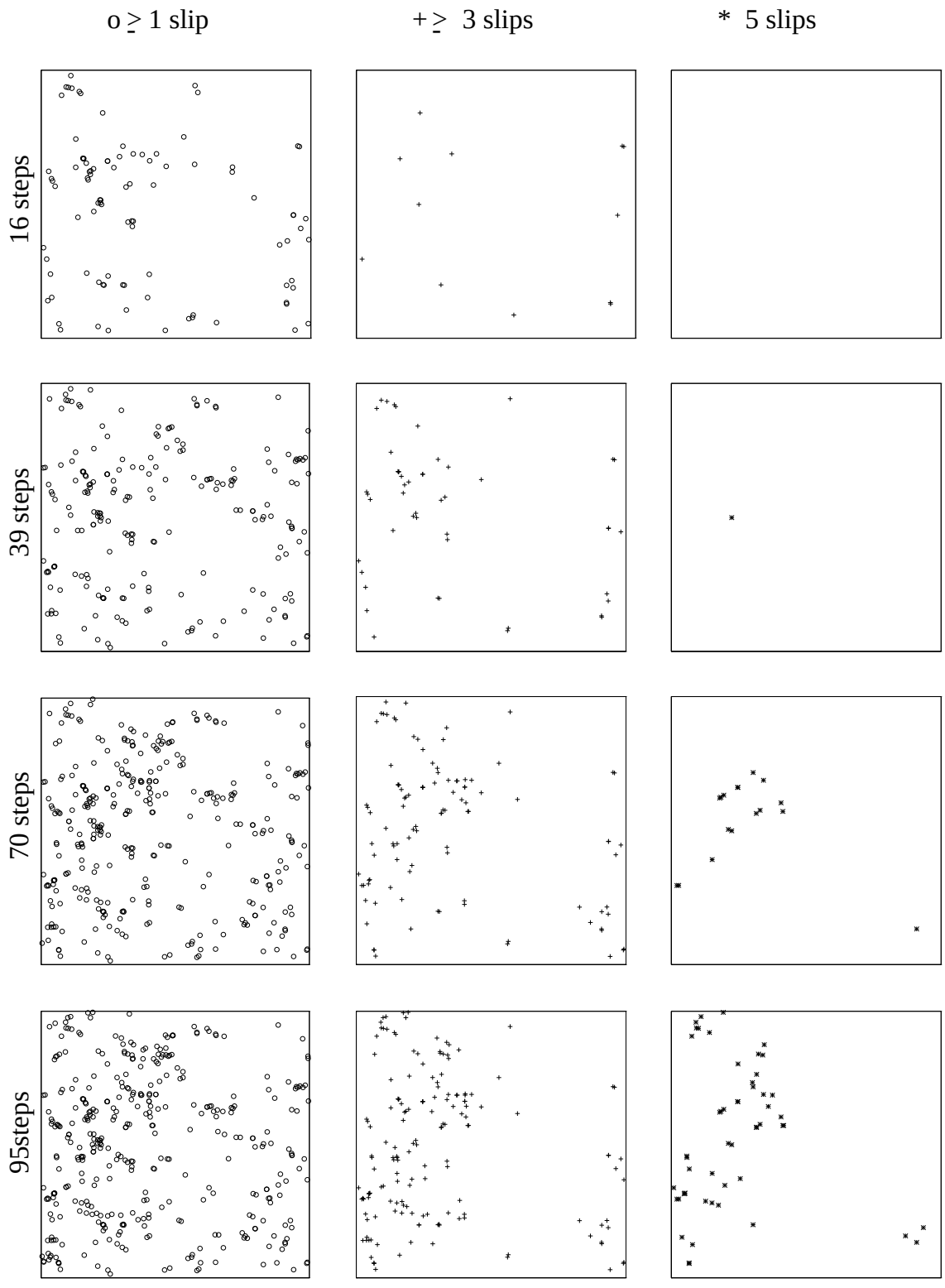

Figure 9.33: *Location of failed connections after 16, 39, 70 and 95 steps.*

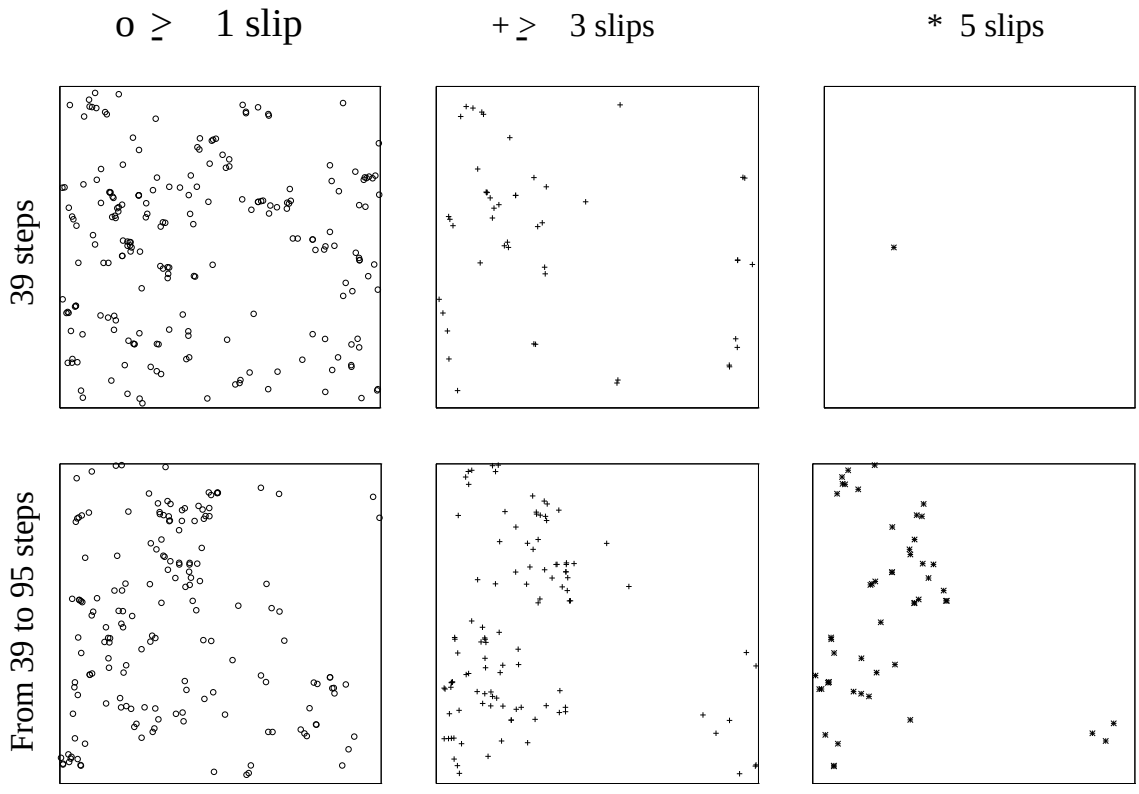

Figure 9.34: *Location of failed connections on the rising and descending part of the stress-strain curve.*

10. Numerical considerations

Some numerical problems have arisen and been dealt with during the study. Basically these problems are all estimated to originate in round-off errors in combination with coefficients of extremely varying magnitude in the global stiffness matrix. This kind of error can be detected by lack of equilibrium, and seems to arise in particular when the solution of the global system of equations is numerically extensive.

When the difference in magnitude of the coefficients is caused by differences between normal and bending stiffness of the beam elements, and between beam and connection stiffness, it has proved to be effective to rescale the matrix as discussed in Section 10.1.

If there happens to be an extremely short beam element in the structure, this causes extremely big coefficients in the stiffness matrix. This is due to the fibre length occurring to the power of three in the denominator of the beam stiffness matrix. This is taken care of by slightly modifying the element, see Section 10.2.

Even with the above measures, in some cases there have been difficulties in achieving accurate global moment equilibrium in the solution when analysing large networks with curled fibres. In those cases moment equilibrium has been explicitely required by constraints in order to stabilize the solution process. This is discussed in Section 10.3.

10.1. Scaling of the stiffness matrix

The character of a dry-shaped cellulose fibre material is such that the fibre-to-fibre connections are much weaker than the fibres, and the fibres themselves are weaker in bending than in axial deformation. The differences in stiffness are, however, not so great that we want to disregard the deformation of the stiffer components by, for example, considering the fibres to be rigid, or possibly rigid in the axial direction. This means that we have a system of equations in which the coefficients are of varying order of magnitude, which implies numerical problems in the solution procedure. This problem is further emphasized by the fact that we want to perform parameter studies over wide ranges of variation of the different material properties. To suppress the effect of these phenomena the coefficients of the stiffness matrix are rescaled. By rescaling the dimension of length, a better conditioned system matrix can often be achieved. Table 10.1 provides some input and output parameters with the corresponding units and scale factors if the length dimension is multiplied by n (equivalent of using another unit for the dimension length).

If we look at the upper left part of the stiffness matrix for a straight beam

Table 10.1:

Parameter	Unit	Scaled parameter
l_f	[m]	nl_f
A_f	[m^2]	n^2A_f
I_f	[m^4]	n^4I_f
E_f	$[\frac{\text{kgm}}{\text{s}^2\text{m}^2}]$	$n^{-1}E_f$
κ	[m^{-1}]	$n^{-1}\kappa$
k_x	$[\frac{\text{kgm}}{\text{s}^2\text{m}}]$	k_x
k_ϕ	$[\frac{\text{kgm}^2}{\text{s}^2}]$	n^2k_ϕ
L	[m]	nL
ρ	[m^{-1}]	$n^{-1}\rho$
u_x	[m]	nu_x
θ	[ ]	θ
F_x	$[\frac{\text{kgm}}{\text{s}^2}]$	nF_x
M	$[\frac{\text{kgm}^2}{\text{s}^2}]$	n^2M

element, (6.3), this means that

$$\begin{bmatrix} \frac{EA}{L} & 0 & 0 \\ 0 & \frac{12EI}{L^3} & \frac{6EI}{L^2} \\ 0 & \frac{6EI}{L^2} & \frac{4EI}{L} \end{bmatrix} \longrightarrow \begin{bmatrix} \frac{EA}{L} & 0 & 0 \\ 0 & \frac{12EI}{L^3} & n\frac{6EI}{L^2} \\ 0 & n\frac{6EI}{L^2} & n^2\frac{4EI}{L} \end{bmatrix}, \tag{10.1}$$

the rotation spring stiffness is multiplied by n^2 and the transversal springs are not affected at all. As an example of the effects of scaling, we study the stiffness matrix of a beam element of 0.5 mm length with properties of the basic example network, Table 5.1. From (6.3) this is

$$\boldsymbol{K}_e = \begin{bmatrix} 1.75\cdot10^4 & 0 & 0 & -1.75\cdot10^4 & 0 & 0 \\ 0 & 6.72 & 1.68\cdot10^{-3} & 0 & -6.72 & 1.68\cdot10^{-3} \\ 0 & 1.68\cdot10^{-3} & 5.6\cdot10^{-7} & 0 & -1.68\cdot10^{-3} & 5.6\cdot10^{-7} \\ -1.75\cdot10^4 & 0 & 0 & 1.75\cdot10^4 & 0 & 0 \\ 0 & -6.72 & -1.68\cdot10^{-3} & 0 & 6.72 & -1.68\cdot10^{-3} \\ 0 & 1.68\cdot10^{-3} & 5.6\cdot10^{-7} & 0 & -1.68\cdot10^{-3} & 5.6\cdot10^{-7} \end{bmatrix}.$$

If we use a scaling factor $n = 10^5$ the stiffness matrix becomes

$$\boldsymbol{K}_e = \begin{bmatrix} 1.75 \cdot 10^4 & 0 & 0 & -1.75 \cdot 10^4 & 0 & 0 \\ 0 & 6.72 & 1.68 \cdot 10^2 & 0 & -6.72 & 1.68 \cdot 10^2 \\ 0 & 1.68 \cdot 10^2 & 5.6 \cdot 10^3 & 0 & -1.68 \cdot 10^2 & 5.6 \cdot 10^3 \\ -1.75 \cdot 10^4 & 0 & 0 & 1.75 \cdot 10^4 & 0 & 0 \\ 0 & -6.72 & -1.68 \cdot 10^2 & 0 & 6.72 & -1.68 \cdot 10^2 \\ 0 & 1.68 \cdot 10^2 & 5.6 \cdot 10^3 & 0 & -1.68 \cdot 10^2 & 5.6 \cdot 10^3 \end{bmatrix}.$$

In order to obtain the condition number (the ratio of the largest singular value of $\boldsymbol{K}_e$ to the smallest) for those single element matrices, three degrees of freedom must be prescribed in order to avoid rigid body motion. This is equivalent to removing three degrees of freedom (rows and columns) from the system. The condition number of the upper left 3×3 matrix without scaling is $1.25 \cdot 10^{11}$, and with scaling it is $1.04 \cdot 10^4$. This example does not precisely tell how the global stiffness matrix is affected by scaling, but practical experience shows that scaling is very efficient and it is used in most of the simulations.

10.2. Modification of extremely short fibres

Since the fibres are independently positioned when the network is generated, there is the possibility that the distance between two crossings on a fibre becomes arbitrarily short. This means that the beam element between the crossings becomes very short. Since beam length occurs to the power of three in the denominator of the beam stiffness matrix, those coefficients become extremely big. In studies where the fibre-to-fibre connections are assumed to be rigid, c.f. [2], [14], this problem has been overcome by merging the two close connections into one. This method is, however, not straightforward to use when the connection is modelled by springs. Instead the beam is slightly modified by moving one of its nodes a short distance. This is also physically reasonable, since the centres of two fibres cannot be closer to each other than one fibre width. In the present implementation, all beams which are shorter than 1/100 of the mean beam element length are modified by moving one end a distance equal to 1/10 of the mean beam element length. This causes a slight distorsion of this fibre, as well as of the fibre connected in the displaced node. The short fibre segments relatively often occur in pairs or triplets, in the form of triangles, in which case the local distorsion of the network becomes somewhat bigger. This is, however, not believed to have an appreciable effect on the final solution since the distorsion is very local and occurs quite rarely.

10.3. Explicit requirement of moment equilibrium

When boundary conditions C are used, only two degrees of freedom, one in the x-direction and one in the y-direction, are prescribed to prevent rigid body motion. This is because global rotation is in theory automatically prevented by the cyclic

boundary conditions. In some cases though, for curled fibres, this has proved to be troublesome numerically. If there is a slight numerical instability in the system, this does not appear as lack of force equilibrium in the x- and y-directions, since the fact that the reaction forces are equal in magnitude and opposite in direction is closely related to the cyclic boundary conditions. Instead it appears as lack of moment equilibrium, that is, the sum of the resultant shear forces on sides 1 and 2 are unequal to that of sides 3 and 4. This has been taken care of by explicitly requiring global moment equilibrium by applying constraints implying that ΣF_x on side 2 be equal to ΣF_y on side 1. This method is believed to give a globally correct solution since the three independent simulations made to obtain $\boldsymbol{D}$, describing initial stiffness, give a symmetric $\boldsymbol{D}$.

11. Concluding remarks

11.1. Summary and conclusions

A network mechanics model for describing materials made of dry-shaped cellulose fibres has been proposed. A two-dimensional implementation of the model has been carried out, and various parameter studies have been performed. Through a parameter which controls whether or not two crossing fibres are bonded to each other, a three-dimensional network can be symbolically represented in a two-dimensional simulation.

The network is composed of fibres, which are modelled as beams of constant in-plane curvature made of linear elastic material. Length, cross-sectional properties, curvature, Young's modulus and ultimate stress for the fibres constituting a network are given in terms of arbitrary statistical distributions.

Where fibres cross there may be fibre-to-fibre interaction. The fibre-to-fibre bonds are modelled as an assemblage of springs. Stiffness and strength properties of the bonds are given in terms of arbitrary statistical distributions, and the probability of a bond at a fibre crossing is another input parameter. The connection springs can be assigned a linear or non-linear behaviour. The non-linear model corresponds to stick-slip performance in the fibre-to-fibre connection.

The fibres are positioned at random in the studied area, with orientation according to a statistical distribution. Network density is another parameter concerning the geometry of the network. The geometry is periodic, that is, the square under consideration is regarded as one of many identical cells making up a global structure of infinite size. Loading is applied by a set of cyclic boundary conditions such that each point on the boundary of a cell is in equilibrium with the corresponding point of the neighbouring cell. At the same time geometric compatibility is achieved at each boundary point. In addition to this method of loading, the more conventional method where straight boundaries are assumed to remain straight is implemented.

Geometry output parameters considered were number of fibre crossings and mechanically active part of the network. It has been verified that the number of crossings obtained from simulations agrees with the number predicted by a theoretical formula from the literature, except for the case of curled fibres where the formula fails, and a new one has been given for the special case of circle arc shape of the curled fibres. The mechanically active part has, for densities above the percolation point, been found to be well approximated by the part of the network that is not free fibre ends. This quantity is easily calculated by use of well-known equations.

A general concept for subjecting a cell of cyclic geometry to load and thereby

obtaining the homogenized elastic parameters of the material has been provided. The method is independent of what kind of heterogeneous material is inside the cell, as long as it is of periodic structure, and was used for obtaining the isotropic stiffness parameters E and ν, as well as the corresponding orthotropic parameters.

Simulations have been performed in order to obtain the global elastic stiffness properties of a network. A basic example network of representative properties has been used, and the different input parameters have been varied in order to yield their respective influence on global elastic stiffness.

Simulations show that the use of cyclic boundary conditions allows simulating smaller cells than does the use of conventional boundary conditions. For the case of constant fibre length, a side-length of the cell of 1.2 times fibre length seems to be enough to avoid a false, simulation-induced, size dependence of the initial stiffness, except for extremely low densities. The conventional conditions with straight boundaries seem to give too high network stiffness even when the side-length of the cell is several times the length of a fibre.

The influence of the individual stiffness components on the global initial stiffness has been examined, and it was concluded that the transversal springs are of greater importance than are the rotational springs of the connections, and that the axial stiffness of straight fibres is more important than the bending stiffness.

Simulations show that curled fibres give a less stiff network, and that this is, in the first place, due to the fibres not extending along a straight path with the connection points along a straight line, and only secondarily because of the smaller axial stiffness of curled beam segments.

For constant network density, long fibres give a stiffer network than short ones do, and for a statistical distribution in length the weighted mean fibre length seems to be a more relevant parameter than the arithmetic mean fibre length.

The influence of network density, degree of fibre-to-fibre interaction and orientation distribution of the fibres on the homogenized stiffness properties have also been investigated.

Fracture criteria have been introduced and the non-linear fracture process of networks analysed. The fracture process has been quantified in terms of initial stiffness, maximum stress, fracture energy, intrinsic length and localization of fracture.

Several results on sample size dependence of fracture properties are indicated and a comparison is made with Weibull theory. The conclusion is that the result from a fracture simulation is always size-dependent, and that Weibull theory is not applicable due to assumptions concerning heterogeneity and material properties not being fulfilled.

The different characters of fibre and connection failure have been indicated by simulating an example network. The failure of a fibre segment has a greater influence on the fracture process than the failure of a connection, since when connection failures are considered the fibres must be pulled out of the network. For dry-shaped materials with no adhesive added though, connection failure is dominant.

For the case of connection failure, simulations have shown that increased strength, decreased stiffness and increased ductility of the connections result in a stronger and

more ductile network.

As for network density, a higher density gives a stronger but more brittle network.

Finally, an example is given of a fracture simulation of a network of curled fibres of varying length, with connections showing stick-slip behaviour.

11.2. Future developments

Possible future work on network mechanics models for cellulose fibre materials includes both further simulations within the present model and development of new or completed models.

Further simulations within the present model include both the many variations of input data which have not been studied yet, and simulations for verification of the model and comparisons with experimental results. A parameter which has not been given the attention it deserves in the present study is the rate of heterogeneity, and its influence on the mechanical properties of a network. One reason for this is that it is not quite straightforward to quantify heterogeneity. Experimentally, heterogeneity is described by variance of local grammage, given a certain cell size. This could also be a useful concept for simulations. It would also be worthwhile to work somewhat with the visualization of the fracture process by means of computer graphics. Although it would not add anything fundamentally new, it would facilitate interpretation of the results.

As for further development of the model there are several possibilities. The two-dimensional model could be refined by including large-strain theory and time dependent effects. The modelling of the fibre-to-fibre interaction also calls for further refinement, preferably coupled to experimental work on the function of fibre-to-fibre bonds. The modelling of the fibres can be improved by consideration of kinks, which affect the fibre geometry and have low or zero bending stiffness. Network geometry, presently generated theoretically, might be taken directly from experimental observation if available. An as yet unexplored area is the effect of initial stresses in the network, originating from the manufacturing process. Another way to go is to, if necessary, simplify the model and go into three-dimensional modelling. In this context the need for developing efficient computational techniques is pronounced.

A. Detection of crossings of two circle arcs

Circle arc shaped fibres A and B are defined by their center points, $\boldsymbol{C}$, radii of curvature, r, and angles between which the fibres extend counter-clockwise, α_1, α_2, see Figure A.1 a). In order to detect possible crossings between fibres A and B, the following path is pursued.

1) Check if circles cross, if so, calculate coordinates of crossings.
Distance d, see Figure A.1 b) between center points $\boldsymbol{C}_A$ and $\boldsymbol{C}_B$, $(C_{Bx} > C_{Ax})$ is

$$d = \sqrt{(C_{By} - C_{Ay})^2 + (C_{Bx} - C_{Ax})^2}.$$

If $r_A + r_B < d$ then circles do not cross.

If $r_A + r_B > d$ then circles cross twice, and the coordinates of the two crossings $\boldsymbol{k}_1$ and $\boldsymbol{k}_2$ are calculated as follows, with notations according to Figure A.1 c).

From the cosine theorem

$$\alpha = \arccos(\frac{r_A^2 + d^2 - r_B^2}{2 r_A d}) \qquad (0 \leq \alpha \leq \pi),$$

and we have

$$\beta = \arctan(\frac{C_{By} - C_{Ay}}{C_{Bx} - C_{Ax}}) \qquad (-\frac{\pi}{2} \leq \beta \leq \frac{\pi}{2}).$$

This gives

$$\begin{aligned} k_{1x} &= C_{Ax} + r_A \cos(\alpha + \beta) \\ k_{1y} &= C_{Ay} + r_A \sin(\alpha + \beta) \\ k_{2x} &= C_{Ax} + r_A \cos(\alpha - \beta) \\ k_{2y} &= C_{Ay} - r_A \sin(\alpha - \beta). \end{aligned}$$

2) If circles cross, check if crossings are on the arcs.

Point $\boldsymbol{k}_1$ is a circlular arc crossing if it is on both circle arcs. With notations according to Figure A.1 d), and i denoting A or B, we have

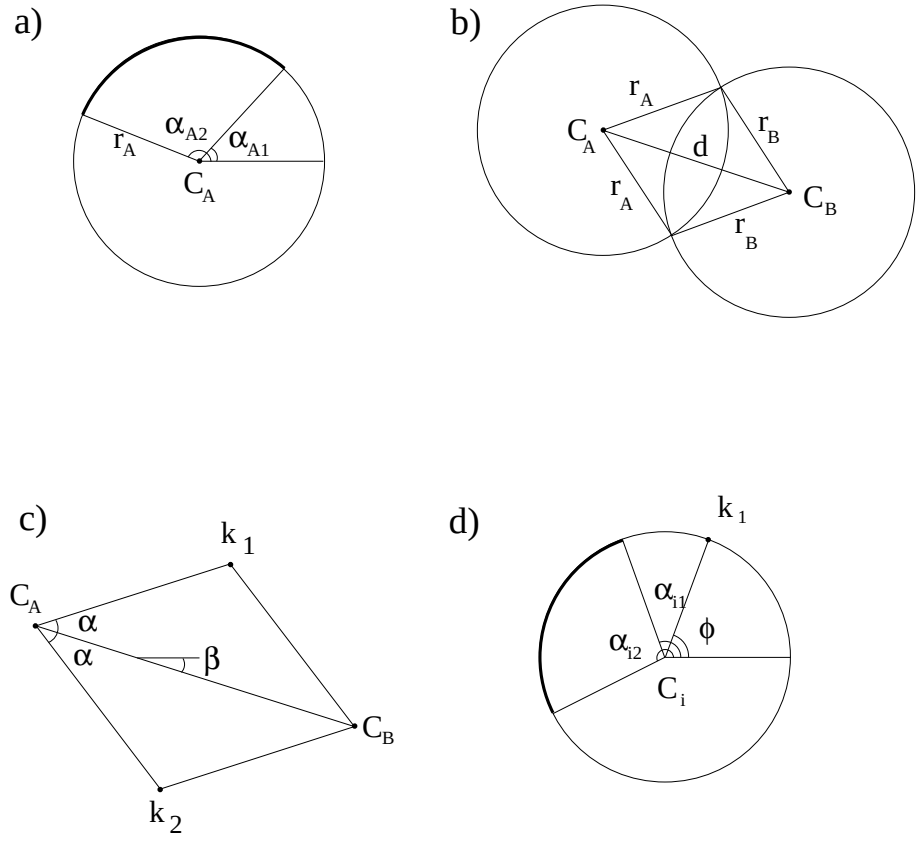

Figure A.1: *Notation used when calculating fibre crossings.*

$$k_{1x} = C_{ix} + r_i \cos\phi$$
$$k_{1y} = C_{iy} + r_i \sin\phi.$$

Introducing

$$\phi_1 = \arccos\frac{k_{ix} - C_{ix}}{r_i} \qquad (0 \le \alpha \le \pi)$$
$$\phi_2 = \arcsin\frac{k_{iy} - C_{iy}}{r_i} \qquad (-\frac{\pi}{2} \le \beta \le \frac{\pi}{2}),$$

we have

$$\phi = \begin{cases} \phi_1; & \phi_2 > 0 \\ 2\pi - \phi_1; & \phi_2 < 0 \end{cases}.$$

Now, obviously, $\boldsymbol{k}_1$ is on arc i if $\alpha_{i1} < \phi < \alpha_{i2}$, or, for the case of $\alpha_{i1} > \alpha_{i2}$, $\boldsymbol{k}_1$ is on arc i if $\alpha_{i2} < \phi$ or $\phi < \alpha_{i1}$. The same procedure is followed for point $\boldsymbol{k}_2$.

B. Analysis of connectedness of network

The first thing that has to be established is what is meant by a connected network. When studying a global network, made up of many cells, it is considered to be a connected network if it is of such geometry that it can sustain load in an arbitrary direction.

For the individual square this implies that there has to be a locally connected structure within the square, which is connected with itself across both the left-right and up-down borders. Figure B.1 shows some schematic examples of connected and non-connected networks.

The criterion given above is a sufficient condition for connectedness of a network, but it is not necessary. This can be seen in Figure B.2, which shows a network that is connected, but still does not satisfy the criterion stated above. The computer program applies the criterion above, and should a network of the type shown in Figure B.2 occur, it is thus falsely classified as not connected.

The following procedure is applied to determine whether a network satisfies the criterion stated above or not.

A network can be viewed as a graph, with beam elements as edges which connect nodes (fibre-to-fibre connections or points on the boundary). A graph can be described by an incidence matrix, in which a 1 in position (i, j) means 'connection between nodes i and j', that is 'a beam element between fibre-to-fibre connections i and j', and a 0 means no connection.

The first thing to do is to sort the graph into connected graphs. (A connected graph is a graph in which there is a path between every pair of nodes.) This is done as follows: Choose an arbitrary node. Incorporate in this node all nodes that it has paths to. Choose a new starting node, which has not previously been classified as a member of a connected graph, and incorporate all nodes that it has paths to. Keep on doing this until every node is part of a connected graph. In the computer code this is done by means of manipulations in the incidence matrix.

Now we have a number of connected graphs. The next step is to go through those and check if any of them satisfies the conditions stated in the beginning. If there is a fibre-to-fibre connection in every fibre crossing there can only be one connected graph that satisfies the conditions, but if there are not connections in every crossing there is a theoretical possibility that there may be more than one. This possibility is not taken into account in the code.

If we have found a connected graph which is also connected with itself across the borders, we must complete it with possible parts that it is connected with across

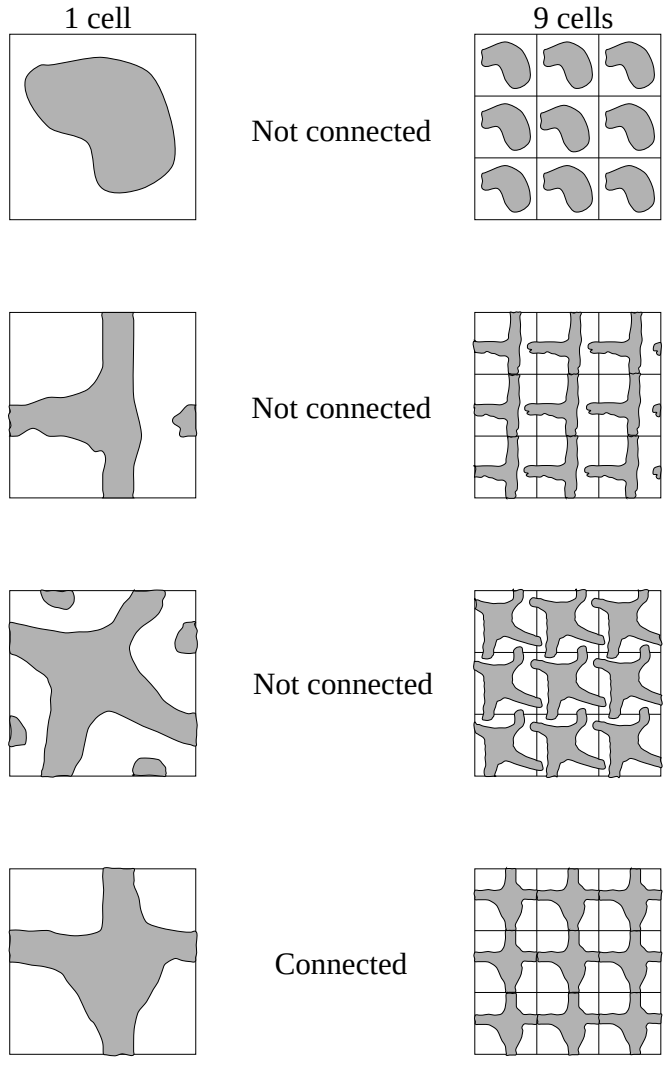

Figure B.1: *Examples of connected and not connected networks.*

borders, but not inside the square.

The rest of the connected graphs, if any, are 'islands', clusters of fibres with no contact with the rest of the global network. Those are removed and can be disregarded in the following.

Clusters of fibres that are attached to the rest of the network by only one fibre are detected as follows. For every beam element: Take away the beam element and go through the procedure above. If there are now two connected graphs, the one that does not satisfy the conditions in the beginning is a 'semi-island', or 'peninsula'.

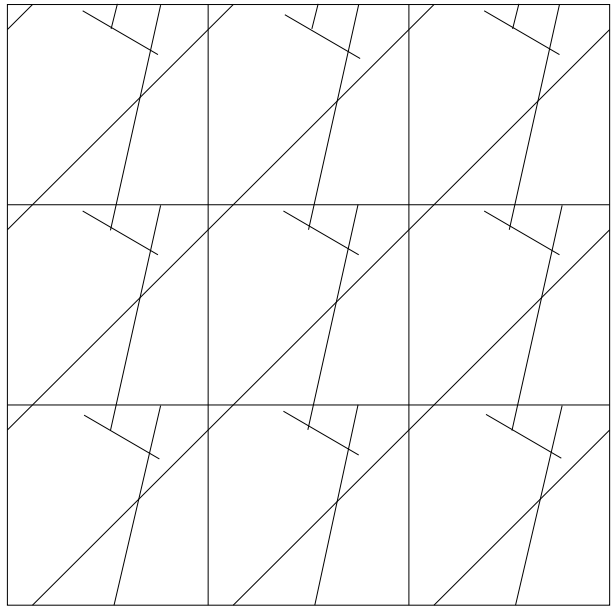

Figure B.2: *A connected network which is difficult to detect.*

C. Angle change of line segment in pure shear

The deformation in pure shear is described by

$$\begin{aligned} x &= X + \gamma Y \\ y &= Y, \end{aligned} \tag{C.1}$$

where capital letters denote coordinates of a point in the undeformed configuration, lower-case letters denote coordinates of a point in the deformed configuration and γ is the angle of shear, see Figure C.1.

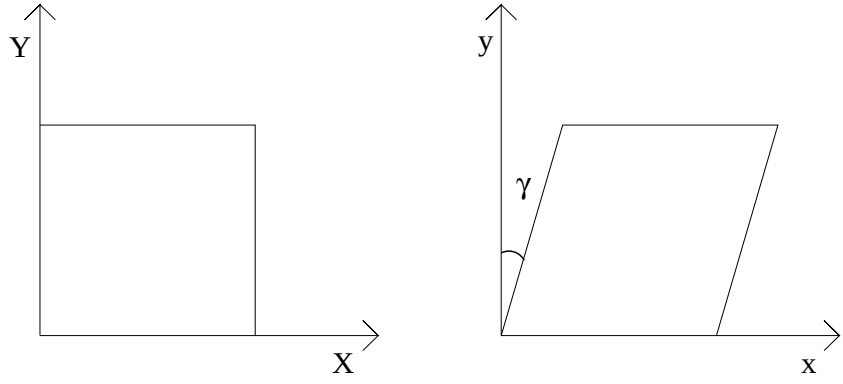

Figure C.1: *Definition of angle of shear, γ, of unit cell.*

The gradient of this deformation is

$$\frac{\partial \boldsymbol{x}}{\partial \boldsymbol{X}} = \begin{bmatrix} 1 & \gamma \\ 0 & 1 \end{bmatrix}. \tag{C.2}$$

A line segment of unit length making an angle α with the x-axis can be described as a vector

$$\begin{bmatrix} X \\ Y \end{bmatrix} = \begin{bmatrix} \cos\alpha \\ \sin\alpha \end{bmatrix}. \tag{C.3}$$

Under pure shear this deforms as

$$\begin{bmatrix} x \\ y \end{bmatrix} = \begin{bmatrix} 1 & \gamma \\ 0 & 1 \end{bmatrix} \begin{bmatrix} \cos\alpha \\ \sin\alpha \end{bmatrix} = \begin{bmatrix} \cos\alpha + \gamma\sin\alpha \\ \sin\alpha \end{bmatrix}. \tag{C.4}$$

The angle α' relative to the x-axis in the deformed configuration is

$$\alpha' = \arctan \frac{\sin \alpha}{\cos \alpha + \gamma \sin \alpha} = \arctan \frac{Y}{X + \gamma Y}. \tag{C.5}$$

To simplify the expression we make a first order approximation in γ by taking the Taylor expansion

$$f(x) = f(0) + \frac{f'(0)}{1!}x + r(x). \tag{C.6}$$

Since

$$\frac{\mathrm{d}}{\mathrm{d}\gamma} \arctan(\frac{Y}{X + \gamma Y})|_{\gamma=0} = \frac{1}{1 + (\frac{Y}{X + \gamma Y})^2}(\frac{-Y^2}{(X + \gamma Y)^2})|_{\gamma=0} = \frac{-Y^2}{X^2 + Y^2} = -\sin^2 \alpha, \tag{C.7}$$

we have

$$\alpha'(\gamma) \approx \alpha - (\sin^2 \alpha)\gamma. \tag{C.8}$$

That is, the angle change of a line segment with initial angle α relative to x-axis is $(\sin^2 \alpha)\gamma$, with sign according to the sign convention used.

D. Effective bending stiffness of spiral beam

We have a spiral beam with moments of inertia $I_{x'}$ and $I_{y'}$ around its principal axes, which completes one revolution in a distance l. We want to know the moments of inertia of the non-spiral beam which yields the same angle change $\Delta\phi_x = u'(l) - u'(0)$ when subjected to moment m_x as in Figure D.1.
The bending stiffness of a spiral beam varies along the z-axis. Therefore we start by computing change in ϕ_x per unit length as a function of z for a spiral beam segment of length l subjected to moment m_x. We begin by considering the angle change per

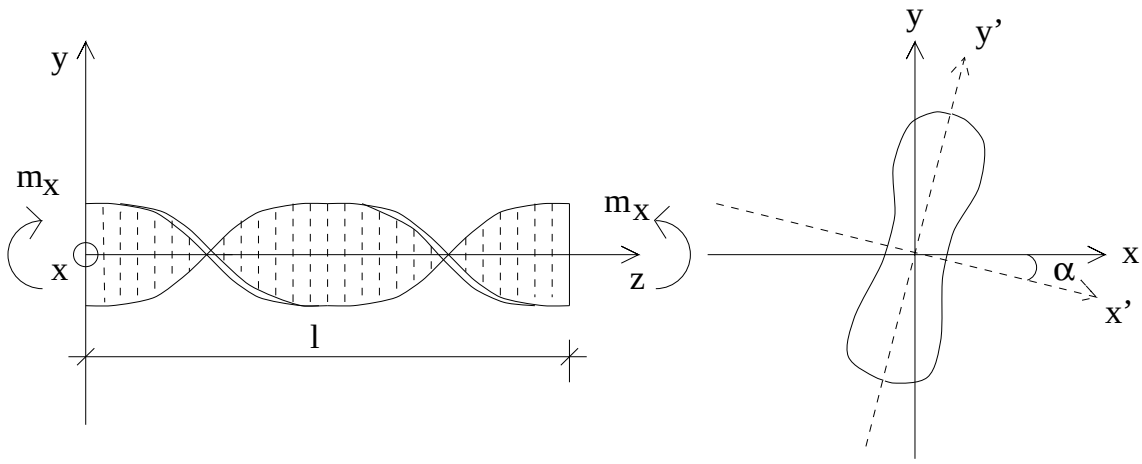

Figure D.1: *Spiral beam segment and cross section.*

unit length around the principal axes of the beam cross-section, x', y', which are rotated an angle α relative to the nominal x- and y-axes.

$$\frac{\mathrm{d}\phi_{x'}}{\mathrm{d}z} = \frac{m_x \cos\alpha}{EI_{x'}}, \qquad \frac{\mathrm{d}\phi_{y'}}{\mathrm{d}z} = \frac{m_x \sin\alpha}{EI_{y'}}. \tag{D.1}$$

From this we can calculate the angle change per unit length around the x-axis.

$$\frac{\mathrm{d}\phi_x}{\mathrm{d}z} = \frac{m_x}{E}\left(\frac{\cos^2\alpha}{I_{x'}} + \frac{\sin^2\alpha}{I_{y'}}\right). \tag{D.2}$$

To obtain the total angle change we integrate over the revolution length, l.

$$\Delta\phi_x = \int_0^l \frac{\mathrm{d}\phi_x}{\mathrm{d}z}\mathrm{d}z = \frac{m_x}{E}\int_0^l (\frac{\cos^2\alpha}{I_{x'}} + \frac{\sin^2\alpha}{I_{y'}})\mathrm{d}z \tag{D.3}$$

Since

$$\alpha = \frac{z}{l}2\pi \tag{D.4}$$

and

$$\mathrm{d}z = \frac{l}{2\pi}\mathrm{d}\alpha, \tag{D.5}$$

D.3 gives

$$\Delta\phi_x = \frac{m_x l}{2\pi E}\int_0^{2\pi} (\frac{\cos^2\alpha}{I_{x'}} + \frac{\sin^2\alpha}{I_{y'}})\mathrm{d}\alpha = \frac{m_x l}{2\pi E}(\frac{\pi}{I_{x'}} + \frac{\pi}{I_{y'}}) = \frac{m_x l}{2E}(\frac{1}{I_{x'}} + \frac{1}{I_{y'}}). \tag{D.6}$$

For a non-spiral cross section with moment of inertia I_e around the x-axis, the angle change on length l when subjected to moment m_x is

$$\Delta\phi_x = \frac{m_x l}{E I_e}. \tag{D.7}$$

On setting $\Delta\phi_x$ for spiral and non-spiral beam equal and solving for I_e we obtain

$$I_e = \frac{m_x l}{E\frac{m_x l}{2E}(\frac{1}{I_{x'}} + \frac{1}{I_{y'}})} = \frac{2I_{x'}I_{y'}}{I_{x'} + I_{y'}}. \tag{D.8}$$

For a rectangular cross section of width b and depth h this yields

$$I_e = \frac{2\frac{bh^3}{12}\frac{b^3h}{12}}{\frac{bh^3}{12} + \frac{b^3h}{12}} = \frac{b^3h^3}{6(b^2+h^2)}. \tag{D.9}$$

E. Relation between network densities in 2 and 3 dimensions

When a three-dimensional network structure is analysed by a two-dimensional model, an interesting issue is the relation between the mass density in 3D, ρ_{3D} [kg/m^3], and the network density in 2D, ρ_{2D} [m^{-1}]. One possible approach is to compare the mean free fibre segment length, $\bar{l}_s$, in the two cases.

If it is assumed that $\bar{l}_s$ is the same in the three-dimensional real material and the two-dimensional model network, a relation between the two densities can be obtained. In this calculation the equations for $\bar{l}_s$ from [17] are used. In those equations it is assumed that the fibres are uniformly distributed in position and orientation. The fibres are assumed to be straight, and in the case of 3D, they are assumed to be of circular cross section.

$\bar{l}_s$ in three dimensions is

$$\bar{l}_s = \frac{2V}{\pi D n_f \bar{l}_f}, \tag{E.1}$$

where D denotes diameter of fibres and V is the volume studied. Since

$$\rho_{3D} = \frac{n_f \bar{l}_f A_f \rho_{fibre}}{V}, \tag{E.2}$$

where ρ_{fibre} denotes the density of a cellulose fibre, we have

$$\bar{l}_s = \frac{D\rho_{fibre}}{2\rho_{3D}}. \tag{E.3}$$

The corresponding equation in two dimensions is, from (2.1) and (2.2),

$$\bar{l}_s = \frac{n_f \bar{l}_f}{2\bar{n}_c} = \frac{\pi}{2\rho_{2D}}. \tag{E.4}$$

Combining (E.3) and (E.4) gives

$$\rho_{2D} = \frac{\pi \rho_{3D}}{D\rho_{fibre}} \tag{E.5}$$

On assuming ρ_{fibre} to be 1600 kg/m^3, and D to correspond to the cross-sectional area of a fibre used in this study, $2.5 \cdot 10^{-10}$ m^2, that is,

$$D = \sqrt{\frac{4A_f}{\pi}} = 1.78 \cdot 10^{-5}\text{m}, \tag{E.6}$$

we have

$$\rho_{2D} \approx 110\rho_{3D}. \tag{E.7}$$

If the probability of a connection in a fibre crossing is s, the equation is modified to

$$\rho_{2D}s \approx 110\rho_{3D}. \tag{E.8}$$

References

[1] Åström, J.A. and Niskanen, K.J. *Simulation of network fracture.* Proceedings of the 1991 International Paper Physics Conference, TAPPI 1991.

[2] Åström, J.A. and Niskanen, K.J. *Symmetry-Breaking Fracture in Random Fibre Networks.* Europhys. Lett., 21 (5), pp. 557-562 (1993).

[3] Berg, A. and Svensson, U. *Computer simulations and analysis of fracture performance in a heterogeneous material structure.* M.Sc. diploma work, Report TVSM-5050, Lund University, Division of Structural Mechanics, Lund, Sweden 1991. (In Swedish).

[4] Blom, G. *Statistikteori med tillämpningar.* Studentlitteratur, Lund, 1984. (In Swedish).

[5] *CALFEM - A finite element toolbox to MATLAB, Version 3.2.* Lund University, Division of Structural Mechanics and Department of Solid Mechanics, Lund, Sweden 1995.

[6] Cox, H.L. *The elasticity and strength of paper and other fibrous materials.* British Journal of Applied Physics, vol 3, pp. 72-79 (1952).

[7] Deng, M. and Dodson, C.T.J. *Paper: An engineered stochastic structure.* Tappi Press, Atlanta, USA 1994.

[8] *Formelsamling i hållfasthetslära.* Royal Inst. of Technology, Department of Solid Mechanics, Stockholm, Sweden 1986. (In Swedish).

[9] Gustafsson, P.J. *Fracture Mechanics Studies of Non-Yielding Materials such as Concrete.* Report TVBM-1007, Ph.D. thesis, Lund University, Division of Building Materials, Lund, Sweden 1985.

[10] Gustafsson, R. *Dynamic analysis of networks: Estimation of stiffness of paper from wave propagation velocity.* M.Sc diploma work, Report TVSM-5064, Lund University, Division of Sructural Mechanics, Lund, Sweden 1996. (In Swedish).

[11] Hahn, H.T. *A Derivation of Invariants of Fourth Rank Tensors.* J. Composite Materials, vol 8, pp 2-14 (1974).

[12] Hamlen, R.C. *Paper structure, mechanics, and permeability: Computer-aided modeling.* Ph.D. thesis, University of Minnesota, USA 1991.

[13] Heyden, S. and Gustafsson, P-J. *A network model for application to dry-shaped cellulose fibre materials.* Report TVSM-7095, Lund University, Division of Structural Mechanics, Lund, Sweden 1996.

[14] Jangmalm, A. and Östlund, S. *Modelling of curled fibres in two-dimensional networks.* STFI, Stockholm, Sweden 1995.

[15] Kallmes, O. and Corte, H. *The structure of paper, I. The Statistical Geometry of an Ideal Two Dimensional Fiber Network.* Tappi, vol 43, pp 737-752 (1960).

[16] Kollmann, F.F.P. and Cote W.A. *Principles of Wood Science and Technology, I, Solid Wood.* Springer-Verlag, Berlin 1968.

[17] Komori, T and Makishima, K. *Numbers of Fiber-to-Fiber Contacts in General Fiber Assemblies.* Textile Research Journal, vol 47, pp. 13-17 (1977).

[18] Krenk, S. *A General Format for Curved and Non-Homogeneous Beam Elements.* Computers & Structures, vol 50, No. 4, pp. 449-454 (1994).

[19] Malvern, L.E. *Introduction to the mechanics of a continuous medium.* Prentice-Hall, Englewood Cliffs, New Jersey 1969.

[20] *MATLAB - High-Performance Numerical Computation and Visualization Software.* The Math Works Inc, Natick, Ma, USA 1992.

[21] Niskanen, K.J. *Strength and fracture of paper.* KCL Paper Science Centre, Finland 1993.

[22] Ottosen N.S. and Petersson H. *Introduction to the finite element method.* Prentice-Hall, U.K. 1992.

[23] Persson, K. *Material model for paper, experimental and theoretical aspects.* M.Sc. diploma work, Lund University, Division of Solid Mechanics, Lund, Sweden 1991.

[24] Popov, E.P. *Mechanics of materials.* Prentice-Hall, Englewood Cliffs, New Jersey 1978.

[25] Rigdahl, M., Westerlind, B. and Hollmark, H. *Analysis of cellulose networks by the finite element method.* Journal of Materials Science, vol 19, pp 3945-3952 (1984).

[26] Salomonsson, A. *A model for dry-shaped cellulose fibre materials.* M.Sc. diploma work, Report TVSM-5051, Lund University, Division of Structural Mechanics, Lund, Sweden 1992. (In Swedish).

[27] SCA Research, Sundsvall, Sweden.

[28] Tryding, J. *In-Plane Fracture in Paper.* Report TVSM-1008, Ph.D. thesis, Lund University, Division of Structural Mechanics, Lund, Sweden 1996.

[29] Yang, C-F. *Plane modeling and analysis of fiber system.* Ph.D. thesis, University of Washington, USA 1975.

[30] Zienkiewicz, O.C. and Taylor, R.L. *The finite element method, fourth edition, vol.1.* McGraw-Hill, London 1989.